Computational Modeling of Flow Separation in an Overexpanded Nozzle for a High-Speed Flow

a project presented to
The Faculty of the Department of Aerospace Engineering
San José State University

in partial fulfillment of the requirements for the degree
Master of Science in Aerospace Engineering

by

Igor Eramov

December 2025

approved by

Dr. Yawo Ezunkpe
Faculty Advisor



© 2025
Igor Eramov
ALL RIGHTS RESERVED

Abstract

Computational Modeling of Flow Separation in an Overexpanded Nozzle for a High-Speed Flow

Igor Eramov

Flow separation in overexpanded rocket nozzles remains a significant problem for engines with high expansion ratios that operate at low altitudes. Depending on operating conditions and nozzle geometry, the separation may occur as free or restricted shock separation. Both types cause unsteady side loads, additional thermal stresses, and performance losses. Despite decades of research, there is still no universally accepted model that can reliably predict the onset and structure of flow separation in real nozzle geometries. This project aims to fill this gap by developing a validated computational fluid dynamics (CFD) model to simulate flow separation in overexpanded nozzles. The model is also used to evaluate an improved conventional high-expansion-ratio nozzle design.

The work is organized into three main stages: theoretical investigation of the problem, development of a CFD model, and modification of the nozzle geometry, followed by performance evaluation.

In the first stage, an approach was developed to generate ideal parabolic contours using the Method of Characteristics – the method, which is widely used to construct truncated ideal contour (TIC) nozzles. Governing equations of classical quasi-one-dimensional and isentropic flow relations were analyzed to identify suitable geometric parameters for the nozzle. The second stage involved creating an efficient and realistic CFD model. The simulation was carried out in Ansys Fluent using a two-dimensional, axisymmetric representation of a second, widely used nozzle type based on the thrust-optimized parabola (TOP) methodology. The workflow for constructing, verifying, and validating the model is documented thoroughly. In the final stage, the validated model was employed to perform a quantitative comparison between the baseline nozzle and a newly developed modified design. The proposed configuration, called TICTOP, combines features from both major nozzle contour families.

The project offers a comprehensive and detailed study of the development of a reliable model for simulating supersonic flow in overexpanded nozzles. Additionally, it covers techniques for geometric modifications to mitigate flow separation. The results demonstrate that hybrid shapes of TIC and TOP geometries can improve nozzle performance and reduce side loads caused by flow separation.

Table of Contents

Abstract . . . . . **iii**

List of Tables . . . . . **vi**

List of Figures . . . . . **vii**

Nomenclature . . . . . **ix**

Acronyms . . . . . **x**

1 Introduction **1**
1.1 Motivation 1
1.2 Literature Review 2
1.2.1 Rocket Nozzle Overview 3
1.2.2 Flow Separation in Overexpanded Nozzles Overview 8
1.2.3 Flow Separation Theoretical Prediction Criteria 11
1.2.4 Computational Fluid Dynamics (CFD) Approaches 12
1.2.5 Modern Advances in Nozzle Design and Flow Control 13
1.3 Project Proposal 14
1.4 Methodology 14

2 Nozzle Design **17**
2.1 Quasi-One-Dimensional Flow 18
2.1.1 Continuity Equation 19
2.1.2 Momentum Equation 20
2.1.3 Energy Equation 21
2.2 Isentropic Compressible Flow Relations 22
2.3 Area–Mach Number Relation 23
2.4 Velocity Potential Equation 27
2.5 Method of Characteristics for Two-Dimensional Supersonic Flow 28
2.5.1 Compatibility Equations 31
2.5.2 Unit Processes 32

3 Preliminary CFD Modeling **37**
3.1 Initial 2D Nozzle CAD Design 37
3.1.1 Geometry 37
3.2 CFD Modeling 40
3.2.1 Mesh 40
3.2.2 Problem Setup 40
3.2.3 Results 43

4 Mesh Generation and Validation Model Development . . . 45
4.1 Sub-scale Nozzle Testing . . . 45
4.2 Computational Model Development . . . 45
4.2.1 Nozzle Geometry: VOLVO S1 . . . 46
4.2.2 Mesh Generation and Quality Criteria . . . 48

5 CFD Setup, Verification, and Validation . . . 56
5.1 Overview of CFD Verification and Validation . . . 56
5.1.1 CFD Verification . . . 56
5.1.2 CFD Validation . . . 59
5.2 Experimental Benchmark for Validation . . . 59
5.2.1 VOLVO S1 CFD Simulation . . . 60

6 Nozzle Performance Evaluation and Design Modification . . . 67
6.1 Performance Evaluation Methodology . . . 67
6.2 Design Modification and TICTOP Concept . . . 72
6.2.1 Geometry of TIC and TICTOP Nozzles . . . 72
6.2.2 Mesh Generation for TIC and TICTOP Nozzles . . . 74
6.3 Results and Discussion . . . 75
6.3.1 Pressure Ratio 8.0 Results . . . 75
6.3.2 Pressure Ratio 14.2 Results . . . 76
6.3.3 Pressure Ratio 16.2 Results . . . 77
6.3.4 Pressure Ratio 22.0 Results . . . 78
6.3.5 Final Performance Comparison . . . 80
6.4 Conclusion . . . 81

References . . . 83

List of Tables

1.1 Separation criteria 12

2.1 Example of MOC calculation for three characteristic lines. 35

3.1 Dimension parameters of conical nozzle design. 39
3.2 Separation pressure and its ratio to the ambient pressure. 44

4.1 VOLVO S1 divergent section dimensions. 47
4.2 Mesh division and bias parameters for each segment. 54

5.1 Grid level parameters. 58
5.2 Boundary conditions for the VOLVO S1 CFD simulation. 62
5.3 Summary of Fluent setup: methods and controls. 62

6.1 VOLVO S1 performance parameters. 72
6.2 Comparison of key performance metrics of TOP, TICTOP, and TIC nozzles. . . 80

List of Figures

1.1 Comparison of different nozzle designs. 3
1.2 Thrust coefficient C_F as a function of pressure ratio, nozzle area ratio, and specific heat ratio for optimum expansion conditions 6
1.3 Thrust coefficient C_F as a function of pressure ratio for the specific heat ratio of 1.2 6
1.4 Ideal contours with different design Mach numbers 7
1.5 Comparison of truncated ideal contour and thrust optimized contour type nozzles 8
1.6 Visualization of FSS 9
1.7 Visualization of RSS 10
1.8 Schematic of asymmetric shock structure in diverging section of over expanded supersonic nozzle 10
1.9 Project geometry example 15

2.1 One-dimensional (left) and quasi-one-dimensional (right) 19
2.2 Finite control volume for quasi-one-dimensional flow 19
2.3 Geometry for the derivation of the area–Mach number relation 25
2.4 Movement of point A along the streamline 29
2.5 Left- and right-running characteristic lines through point A 31
2.6 Intersecting left-running and right-running characteristics at point 3 32
2.7 Characteristic line intersecting with a point 5 on a solid wall. 33
2.8 Three characteristics and corresponding nodes 34
2.9 Minimum-length nozzle design for Mach number 2.5 and $\gamma = 1.4$ 35
2.10 Minimum-length nozzle wall contour for Mach number 2.5 and $\gamma = 1.4$ 36

3.1 Conical nozzle contour 38
3.2 Conical nozzle with computational domain 39
3.3 Computational mesh 40
3.4 Meshed nozzle section 40
3.5 Mach number and static pressure contours for different PR values 43
3.6 Axis Mach number (left) and nozzle wall pressure for different PR values . . . 44

4.1 Geometry of the VOLVO S1 TOP nozzle section 47
4.2 Computational domain with boundaries 48
4.3 Example of a block structure for a complex geometry with the corresponding structured mesh 51
4.4 Block-structured computational domain 52
4.5 Block-structured nozzle section and surrounding regions 52
4.6 Mesh control strategy for the nozzle section 53
4.7 Computational mesh for the VOLVO S1 nozzle design 55

5.1 Three grid levels . . . 58
5.2 Wall pressure distribution for different mesh resolutions . . . 59
5.3 Mach number contours for different PRs . . . 63
5.4 Wall pressure distribution at PR = 8 . . . 64
5.5 Wall pressure distribution at PR = 14.2 compared with experiment . . . 64
5.6 Wall pressure distribution at PR = 16.2 compared with experiment . . . 65
5.7 Wall pressure distribution at PR = 22.0 compared with experiment . . . 65

6.1 Axial Mach number distribution at various PR along the exit cross-section . . . 68
6.2 Mach number streamlines for different PRs . . . 69
6.3 Density distribution at nozzle exit (left) and density contours (right) for different PRs. . . . 70
6.4 Pressure distribution at nozzle exit (left) and Pressure contours (right) for different PRs. . . . 70
6.5 Comparison of TIC contours with the baseline TOP nozzle geometry . . . 73
6.6 Comparison of TIC, TOP, and TICTOP contours . . . 74
6.7 Block-structured sections of TIC and TICTOP nozzles . . . 74
6.8 Nozzle section meshes of the TIC and TICTOP types . . . 75
6.9 Mach number contours for TOP, TICTOP, and TIC nozzles at PR = 8 . . . 75
6.10 Wall-pressure distributions for TOP, TICTOP, and TIC nozzles at PR = 8 . . . 76
6.11 Mach number contours for TOP, TICTOP, and TIC nozzles at PR = 14.2 . . . 76
6.12 Wall-pressure distributions for TOP, TICTOP, and TIC nozzles at PR = 14.2 . . . 77
6.13 Mach number contours for TOP, TICTOP, and TIC nozzles at PR = 16.2 . . . 78
6.14 Wall-pressure distributions for TOP, TICTOP, and TIC nozzles at PR = 16.2 . . . 78
6.15 Mach number contours for TOP, TICTOP, and TIC nozzles at PR = 22.0 . . . 79
6.16 Wall-pressure distributions for TOP, TICTOP, and TIC nozzles at PR = 22.0 . . . 79

Nomenclature

A_c	Combustion chamber area
A_e	Exit area
A_t, A^*	Throat area
a	Local speed of sound
C_F	Thrust coefficient
C_p	Specific heat
C_{fric}	Skin friction coefficient
e	Internal energy
F_T	Rocket thrust
g	Gravitational acceleration
$\mathrm{I_{TIC}}$	Axial position of the transition
h	Enthalpy
k	Kinetic energy
k_A	Velocity ratio
k_{th}	Thermal conductivity
L_c	Chamber length
L_n	Length diverging section
L^*	Characteristic length
M	Mach number
M_{des}	Design Mach number
Ma_{sep}	Separation Mach number
M_W	Molecular weight
$\dot{m}$	Mass flow rate
R_c	Chamber radius
R_{con}	Contour radius
R_d	divergent throat curvature
R_e	Exit radius
R_t, R^*	Throat radius
p_a	Ambient pressure
p_c	Chamber pressure
p_e	Exit pressure
p_{op}	Operating pressure
p_p	Plateau pressure
p_{sep}	Separation pressure
p_w	Wall pressure
R	Specific gas constant
R_A	Universal gas constant
S	Control surface
t	Time
T_c	Chamber temperature
u, v, w	Velocity components
U_∞	Freestream velocity
u_τ	Friction velocity
$\mathscr{V}$	Volume
V_c	Chamber volume
v_e	Exit velocity
$V_{e,\mathrm{eff}}$	Effective exit velocity
x, y, z	Cartesian coordinates
y^+	y-plus
α_c	Divergent cone half-angle
δ	boundary layer thickness
ε	Expantion ratio
ε_c	Contraction ratio
γ, κ	Specific heat ratio
$\Gamma(\gamma)$	Vandenkerckhove function
μ_M	Mach angle
ν	Kinematic viscosity
$\nu(M)$	Prandtl-Meyer function
ρ	Density
τ_w	Wall shear stress
θ	Flow angle
θ_c	Conical nozzle angle
θ_e	Exit wall angle
θ_N	Initial wall angle
θ_w	Wall angle
ω	Specific dissipation rate

Acronyms

CAD	Computer aided design
CD	Convergent–divergent
CFD	Computational fluid dynamic
CFL	Courant-Friedrichs-Lewy condition
FSS	Free shock separation
LES	Large Eddy Simulation
MOC	Method of characteristics
ODE	Ordinary differential equation
OML	Outer mold line
PDE	Partial differential equation
PR	Pressure ratio
RANS	Reynolds-averaged Navier Stokes
RSS	Restricted shock separation
SA	Spalart-Allmaras
SST	Shear stress transport
TIC	Truncated ideal contour
TOC	Thrust-optimized contour
V&V	Verification and validation
2D	Two dimensional
3D	Three dimensional

Chapter 1 - Introduction

1.1 Motivation

In recent years, there has been a significant increase in space missions, leading to a rise in the demand for higher-performing space systems. Modern advancements in this area emphasize trends such as reusable space launch vehicles and improvements in rocket engine performance across a broader range of operating conditions. To achieve these objectives, we need a detailed study of rocket engine components, such as rocket nozzles, which significantly influences the entire engine performance and reliability.

The rocket engine nozzle is a major component for generating thrust and constitutes a large portion of the engine structure. Due to its shape, the flow within the nozzle first converges to a minimum area, or throat, and then expands through the divergent section to the exit. This process accelerates the hot, high-pressure exhaust gases to supersonic speeds, forming a high-momentum jet that produces thrust.

Rocket thrust is one of the crucial characteristics of the engine that propels the vehicle. Higher thrust is desirable as it provides higher vehicle acceleration to overcome gravity more quickly, the ability to carry heavier payload, and other performance gains. To achieve greater thrust, the exhaust gases must have higher kinetic energy, which can be reached through a larger expansion ratio [1]. However, the increase in pressure ratio is limited by ambient pressure effects, which determine the nozzle's operating regime.

Optimum thrust and nozzle performance occurs when the exhaust gases are fully expanded to the surrounding pressure, creating a parallel uniform flow. However, to reduce weight and complexity, nozzles are designed with a fixed expansion ratio that keeps the exit pressure at a constant value while the ambient pressure decreases with altitude [2]. This results in three operating regimes: underexpanded (exit pressure is higher than ambient), fully expanded (pressures are equal), and overexpanded (exit pressure is lower than ambient).

Modern rocket engines are calculated and designed to operate at a specific altitude, typically above sea level, where most of their work is performed and ambient pressure is lower. As a result, rocket nozzles operate in an overexpanded regime during low-altitude flights, engine starts, or shutdowns. Nozzles face several performance and efficiency issues such as flow separation at the overexpanded condition.

Flow separation is a complex physical phenomenon where the boundary layer of the flow detaches from the nozzle walls due to the prevailing ambient pressure. In high-speed flows, this detachment leads to pressure stabilization through shock waves. There are two types of flow

separation: 1) Free Shock Separation, where the overexpanded flow completely detaches from the wall, forming recirculation zones and an oblique shock wave near the wall, and 2) Restricted Shock Separation, where the flow reflects and reattaches downstream.

Flow separation causes excessive side loads on the nozzle wall and increases its temperature, compromising the nozzle structural integrity. In rocket design, flow separation is undesirable because an asymmetry in the flow can yield dangerous lateral forces, which may damage the nozzle [3]. The test failures of projects such as the Space Shuttle, Saturn V J-2, and Japanese LE-7A are clear examples of how these side loads can impact the nozzle operation [4]. Additionally, flow separation negatively affects the engine performance, increases vibrations, and leads to other operational issues.

To date, there is no definitive physical interpretation of the cause and behavior of supersonic flow separation in overexpanded nozzles, as noted in Hadjadj's work on the study of flow separation structures [3]. Therefore, extensive studies on flow separation in overexpanded rocket nozzles are essential to prevent separation and develop methods for flow control. This can improve nozzle efficiency, extend service life, and enhance reliability of rocket engines.

Flow control is a manipulation of the characteristics and properties of a fluid flow by introducing external influences to meet specific requirements and objectives. It can serve as an alternative approach to mitigating or eliminating flow separation when its occurrence is unavoidable. Several flow control methods are categorized into active and passive, based on their energy source. Passive flow control involves modifications to the nozzle geometry or surface, such as dual-bell nozzles, surface roughness adjustments, optimized nozzle contours, and more.

Active methods usually require an external energy source. Microjet injection involves secondary gas injection microjets near the separation line, delaying flow separation and improving the efficiency of nozzle flow [5]. Another active control method is removing low-momentum boundary-layer fluid by suction, where a portion of the flow is removed from the boundary layer through small openings in the nozzle wall [6]. These techniques help to maintain a more stable flow structure and reduce the flow separation formation.

1.2 Literature Review

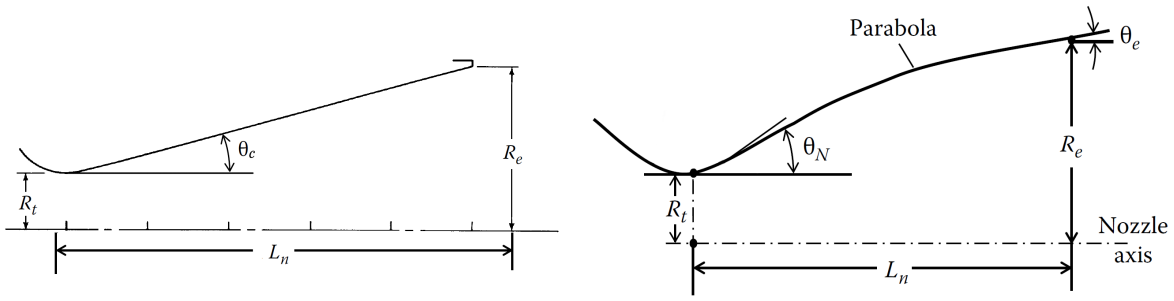
This section reviews the main aspects of flow separation in overexpanded rocket engine nozzles. The literature review begins with an overview of nozzle designs used in rocket engineering, focusing on the geometric and performance characteristics, as nozzle shape plays a significant role in the formation of flow separation. The main types of nozzles are examined, along with the governing ideal flow equations. The performance characteristics dependency is illustrated with respect to the nozzle design.

Next, flow separation at supersonic speeds in overexpanded nozzles is observed as a physical phenomenon. The primary types of flow separation are identified, and the key factors of occurrence are analyzed. Additionally, the section provides existing theoretical criteria for predicting flow separation. Recent advancements in computational fluid dynamics (CFD) related to this field are also discussed.

In conclusion, the section explores current options for modifications of rocket nozzles and flow control methods for preventing and mitigating flow separation negative consequences.

1.2.1 Rocket Nozzle Overview

Before analyzing flow separation phenomena, it is necessary to consider the conventional rocket nozzle designs, as their geometry has a significant influence on the formation of flow. Convergent–divergent (CD) nozzles are primarily used for producing thrust in rocket engines [1], [7], and [8]. The conventional nozzle geometries are called a conical nozzle and a bell-shaped nozzle, as shown in Figs. 1.1a and 1.1b. Bell-type nozzles are the most widely used in modern rocket engineering today.



(a) Schematic of a conical CD nozzle [9].

(b) Schematic of a bell-shaped CD nozzle [1].

Figure 1.1: Comparison of different nozzle designs.

The main dimensions shown in Fig.1.1 include the length of the diverging section L_n, throat radius R_t, nozzle exit radius R_e, conical nozzle angle θ_c, initial wall angle of the parabola θ_N, and nozzle-exit wall angle θ_e.

The nozzle is a body of revolution around its axis. It features a converging inlet section from the combustion chamber, a throat, and a diverging section to the nozzle exit. A conical nozzle design requires only one angle θ_c, whereas a bell nozzle involves selecting both angles θ_N and θ_e. The conical type has historically been the most common contour for rocket nozzles due to its design simplicity. However, the bell type nozzle is the most commonly used shape in rocket engines today [10]. This category of nozzle provides significant benefits in terms of performance and size over the conical type nozzle.

The preliminary flow analysis in CD nozzle and geometry calculations begins consideration of ideal flow [1]. Gas-flow calculations for rocket thrust-chamber design usually assume the following conditions [8]:

- Homogeneous gas composition.
- Perfect gas.
- No heat transfer through the motor walls in either direction (i.e., adiabatic processes).
- No friction.
- Steady flow rate.
- One-dimensional flow (all gas molecules move on parallel lines).
- Velocity uniformity across any section normal to chamber axis.
- Chemical equilibrium established within the combustion chamber and remaining constant in the nozzle.

This project involves developing a nozzle geometry for subsequent computer aided design (CAD) modeling and computational fluid dynamic (CFD) analysis. Consequently, there is a need to consider the process of calculating the main dimensions. Preliminary calculation of nozzle parameters usually includes the following governing equations [8].

Exit velocity:

$$v_e = \sqrt{\frac{2\gamma}{\gamma - 1}\frac{R_A}{M_W}T_c}\left[1 - \left(\frac{p_e}{p_c}\right)^{\frac{\gamma-1}{\gamma}}\right] \tag{1.1}$$

Where γ is the specific heat ratio, R_A is the universal gas constant, M_W is the molecular weight of the gas, T_c is the temperature in the combustion chamber, p_e is the exit pressure of the nozzle, and p_c is the pressure of the combustion chamber.

Theoretical mass flow rate:

$$\dot{m} = \frac{p_c A_t}{\sqrt{\frac{R_A}{M_W}T_c}}\Gamma(\gamma) \tag{1.2}$$

Where A_t is the throat area, and $\Gamma(\gamma)$ is Vandenkerckhove function.

$$\Gamma(\gamma) = \sqrt{\gamma\left(\frac{1+\gamma}{2}\right)^{1-\gamma}} \tag{1.3}$$

Theoretical nozzle expansion ratio:

$$\varepsilon = \frac{A_e}{A_t} = \frac{\left(\frac{2}{\gamma+1}\right)^{\frac{1}{\gamma-1}} \left(\frac{p_c}{p_e}\right)^{\frac{1}{\gamma}}}{\sqrt{\frac{\gamma+1}{\gamma-1}\left[1-\left(\frac{p_e}{p_c}\right)^{\frac{\gamma-1}{\gamma}}\right]}} \tag{1.4}$$

Where A_e is the nozzle exit area.

The pressure ratio:

$$\frac{p_e}{p_c} = \left(\frac{2}{\gamma+1}\right)^{\frac{\gamma}{\gamma-1}} \tag{1.5}$$

Rocket thrust equation:

$$F_T = \dot{m} v_e + (p_e - p_a) A_e \tag{1.6}$$

Where p_a is ambient pressure.

Also, for a comparative assessment of engine efficiency and, accordingly, the nozzle, the parameters of specific impulse Eq.1.7 and thrust coefficient Eq.1.8 are widely used.

$$I_{sp} = \frac{F_T}{\dot{m} g} \tag{1.7}$$

Where g is the gravitational acceleration constant.

$$C_F = \frac{F_T}{p_c A_t} = \sqrt{\frac{2\gamma^2}{\gamma-1}\left(\frac{2}{\gamma+1}\right)^{\frac{\gamma+1}{\gamma-1}}\left[1-\left(\frac{p_e}{p_c}\right)^{\frac{\gamma-1}{\gamma}}\right]} + \varepsilon\frac{p_e - p_a}{p_c} \tag{1.8}$$

From the equation of the thrust coefficient, it follows that maximum thrust is achieved when $p_e = p_a$, which corresponds to the full expansion of exhaust gases in the engine nozzle.

Figures 1.2 and 1.3 clearly illustrate the dependence of the thrust coefficient on different pressure ratios, nozzle area ratios, and specific heat ratios. The area expansion ratio is denoted as ε, k represents the specific heat ratio γ, p_1 denotes the chamber pressure p_c, p_2 represents the exit pressure p_e, p_3 is the ambient pressure p_a, and A_2 represents the exit nozzle area A_e. Therefore, the Fig.1.3 shows the variations in the thrust coefficient for γ = 1.2 as a function of pressure ratio p_c/p_a and area ratio ε.

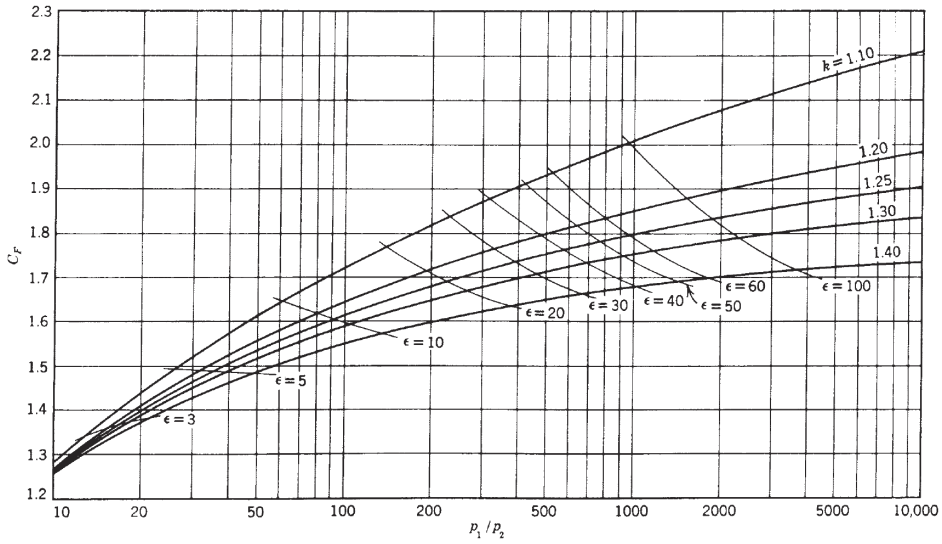


Figure 1.2: Thrust coefficient C_F as a function of pressure ratio, nozzle area ratio, and specific heat ratio for optimum expansion conditions [11].

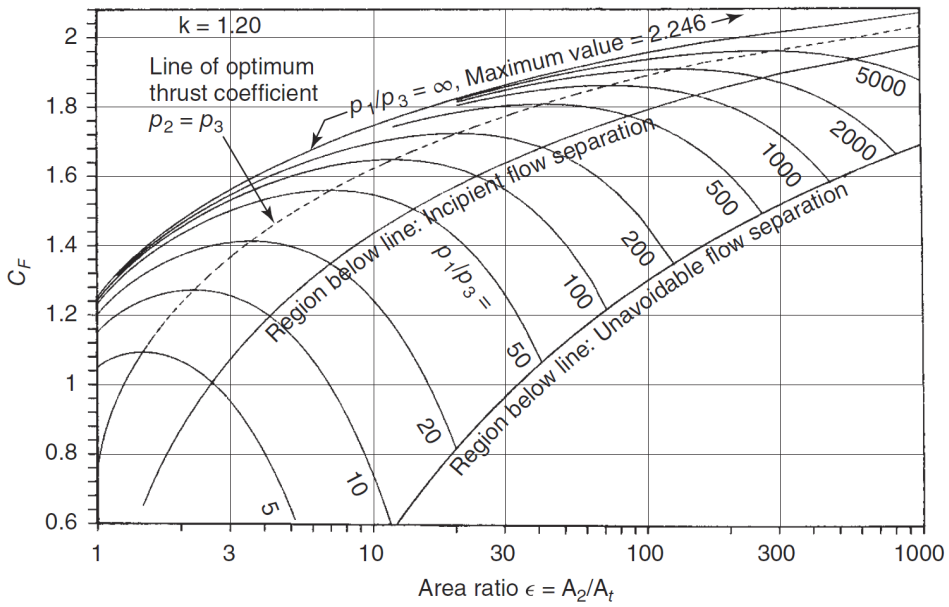


Figure 1.3: Thrust coefficient C_F as a function of pressure ratio for the specific heat ratio of 1.2 [11].

Currently, mainly two contouring methods are used for the design of rocket engine nozzles, namely the truncated ideal contour (TIC) and the thrust-optimized parabola (TOP). Both types feature a rounded and parabolic geometry in the expansion section of the nozzle.

This shape provides a smooth surface transition without sharp corners, which prevents high-speed flow separation while also providing with an increased the expansion ratio due to a larger cross-sectional area. Only the nozzle exit plane has a sharp edge, because a rounded one would permit over-expansion and lead to flow separation. Regardless of the nozzle type, the design solution is based on basic principles [8], [12]:

- Uniform, parallel, axial gas flow at the nozzle exit.
- Minimum separation and turbulence losses within the nozzle.
- Shortest possible nozzle length for minimum space envelope, weight, wall friction losses, and cooling requirements.

Truncated Ideal Contour (TIC) Nozzle

In inviscid flow, it is possible to design so-called ideal contour nozzles that have a uniform exit flow profile, meaning constant pressure, temperature and velocity over the whole exit plane. Already before the middle of the last century, computational methods to design such contours were available [12]. For the fixed chamber and throat geometries, the only free design parameter is the Mach number M_{des}. The higher the design Mach number, the higher is the maximum divergence angle and the larger is the nozzle as shown in Fig.1.4.

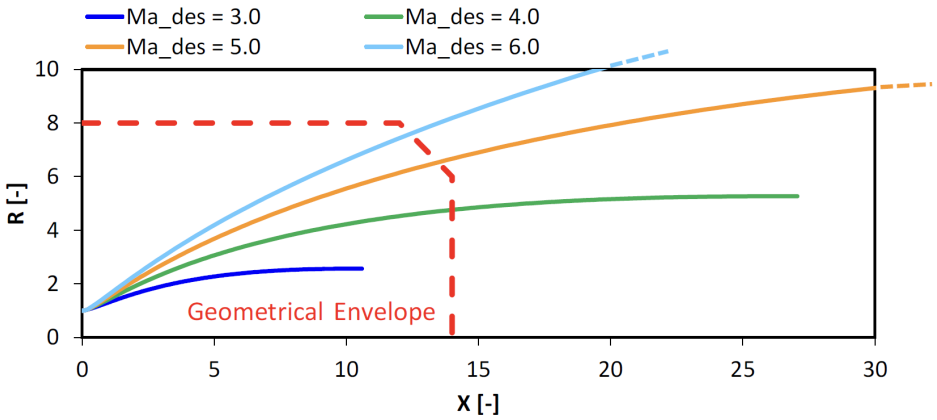


Figure 1.4: Ideal contours with different design Mach numbers [12].

For space applications with their restrictive mass requirements, ideal contours are too long and thus too heavy. Therefore, ideal contours are truncated for space applications, resulting in so-called truncated ideal contours.

Thrust-Optimized Parabola (TOP) Nozzle

The thrust optimization is carried out by varying two angles, θ_N and θ_e, and selecting the nozzle with the highest thrust. In most cases, the optimum is flat, meaning that a moderate variation of, for example, 1° on either angle hardly influences the resulting thrust. Taking into account also the optimization process, there is only one TOP for a given exit point, i.e. there are no free design parameters [12].

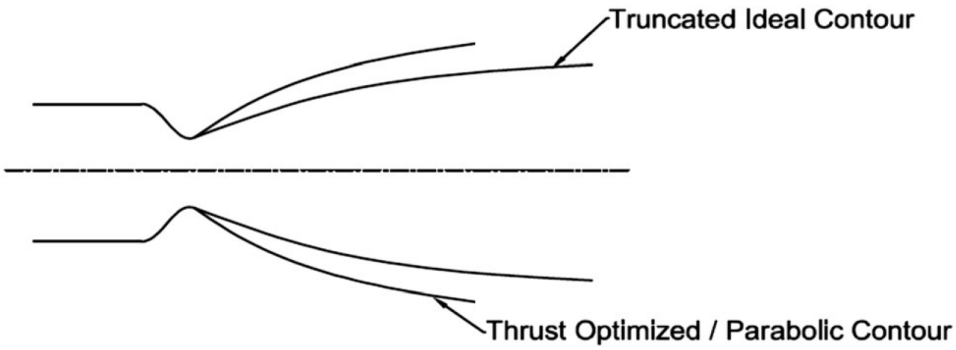


Figure 1.5: Comparison of truncated ideal contour and thrust optimized contour type nozzles [10].

Real Rocket Nozzles and Losses

In real rocket nozzles, several losses occur during operation, affecting overall efficiency. The three main types of losses are:

- Chemical Losses - Incomplete combustion or dissociation of exhaust gases can reduce available energy.
- Viscous Losses – Friction and turbulence within the nozzle cause energy dissipation, reducing thrust.
- Geometric Losses – Imperfect nozzle design, such as non-ideal expansion ratios or flow separation, can lead to inefficiencies.

1.2.2 Flow Separation in Overexpanded Nozzles Overview

The flow separation in rocket nozzles occurs when the ratio of wall pressure to ambient pressure p_w/p_a is less than approximately 30 % [12]. This holds true for TIC and TOP nozzles. The exhaust flow, reaching a certain pressure value at the wall, detaches from the nozzle inner surface due to the superior ambient pressure. This leads to the formation of a shock wave and a recirculation flow (Fig.1.6).

In 1973, Nave and Coffey [13] discovered and proposed two types of flow separation, which remain the main ones today. They observed that after separating from the wall, the jet flow continues toward the nozzle exit, forming a large recirculation zone Fig.1.6. This regime

is called Free Shock Separation (FSS). In cases of asymmetric boundary layer separation, an inclined separation surface forms, increasing lateral loads on the wall [14].

FSS is typical for TIP nozzles and is the initial phase of development of the second type of flow, which is called Restricted Shock Separation (RSS), shown in Fig.1.7. As the FSS flow moves toward the nozzle exit, the recirculation zone expands, generating a vortex flow structure. When the vortex reaches the nozzle center, it obstructs the main exhaust jet and deflects the flow back toward the wall. As a consequence, a radial flow component is generated that tends to reattach the separated region to the wall [14].

The resulting "trapped vortex," illustrated in Fig.1.7, forms a curved shock wave known as the cap-shock pattern. A closed recirculation region emerges between the separation and reattachment points, resulting in a sharp pressure jump at the point of reattachment to the nozzle wall [15]. This type of flow behavior is characteristic of TOP-type nozzles. However, both modes significantly impact engine performance reducing thrust. Moreover, FSS and RSS cause significant lateral loads, also known as side loads, which can exceed 20% of engine's axial thrust [4].

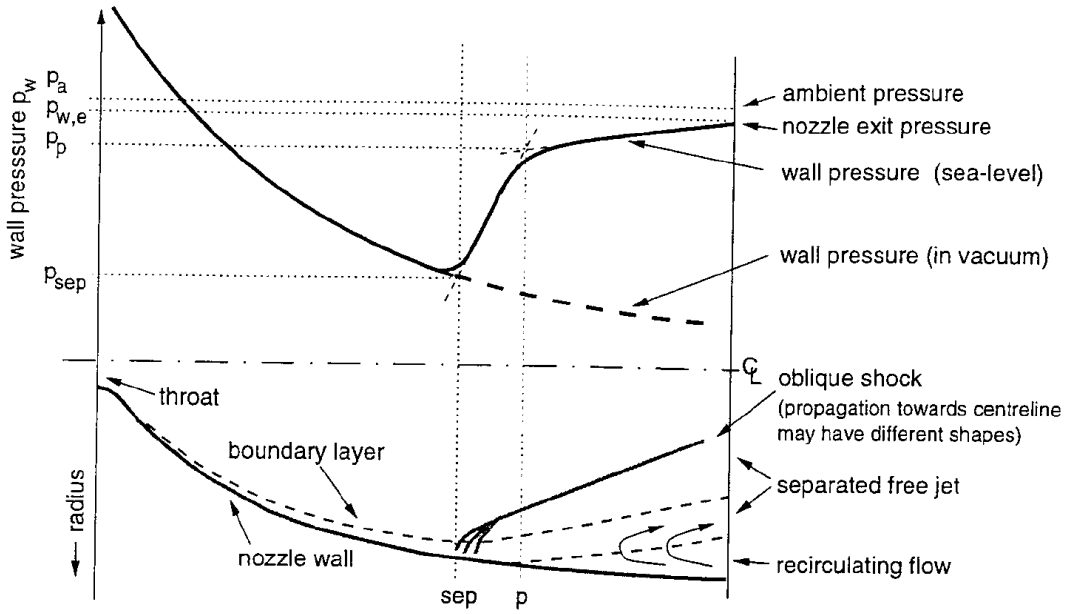


Figure 1.6: Visualization of FSS [15].

In both cases, asymmetric flow separation can occur, deflecting the jet stream from the nozzle centerline and making flow separation a three-dimensional asymmetric phenomenon. The transition process from FSS to RSS makes the flow unsteady, which increases the difficulty to analyze this phenomenon properly. The transient flow separation process is difficult to avoid due to the ambient pressure changing with altitude. Moreover, during this transition process, the highest pressure peaks on the wall are generated.

The mechanism behind flow separation formation is complex. According to [14], this phenomenon is governed by an inviscid mechanism. The driving factor is the non-uniformity of the flow incident on the separation shock. As a result, the shock force changes along its surface, resulting in a curved shock profile.

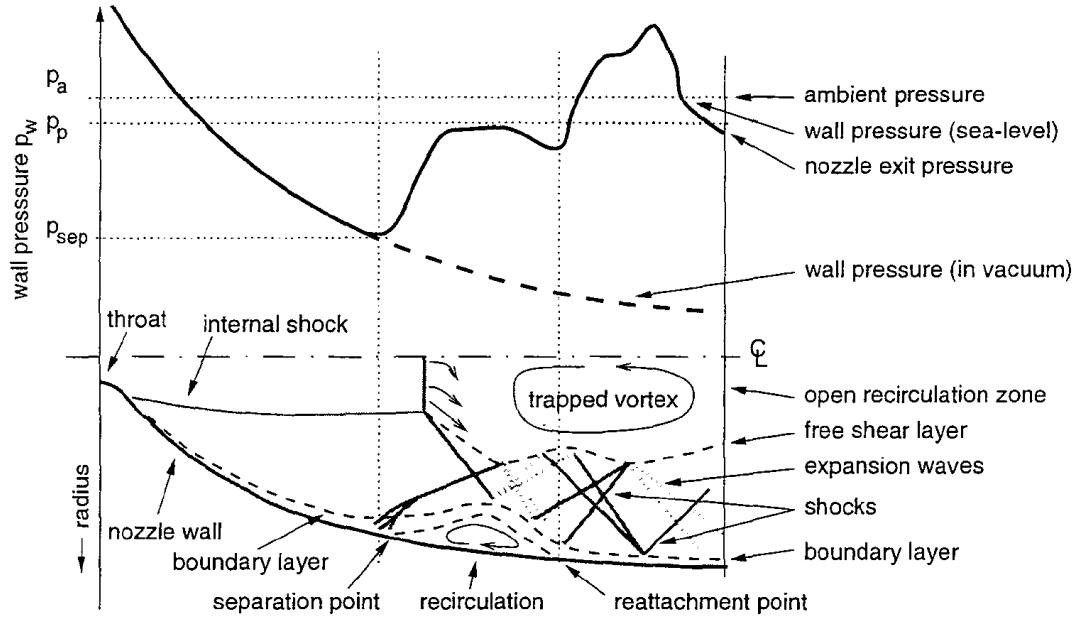


Figure 1.7: Visualization of RSS [15].

The asymmetry of flow separation also has a serious negative effects in terms of side loads and analytical complexity. Under overexpanded flow conditions, there is a range of nozzle pressure ratios (PR) in supersonic nozzles for which the separated flow becomes asymmetric. In such a case, the flow deviates from the nozzle centerline as shown in Fig.1.8. The result of such deviation may be FSS and RSS region along the top and bottom walls of the diverging section. Such asymmetric separated flow results in a thrust vector, which is offset at certain angle from its symmetrical axis, leading to a significant change in thrust and potential structural damage [16].

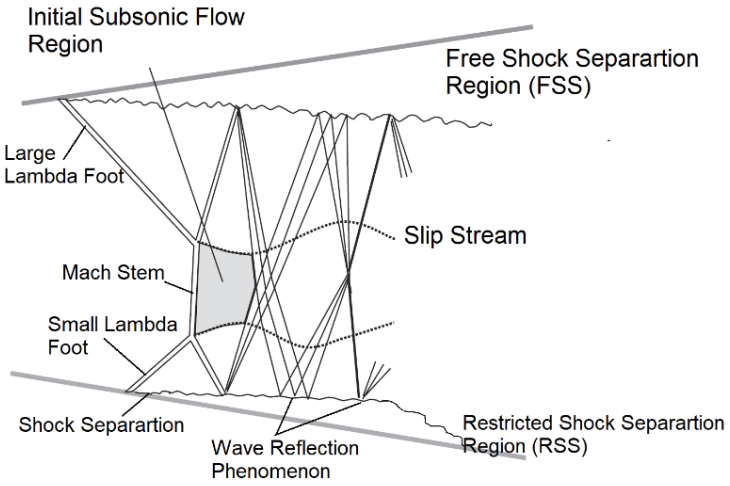


Figure 1.8: Schematic of asymmetric shock structure in diverging section of over expanded supersonic nozzle [16].

The shock structure near the wall is called "lambda foot." In the case of asymmetric separation, one lambda foot becomes larger than the other, creating the FSS region. In contrast, the RSS region develops along the opposite wall. Both shock waves merge in a formation called

the Mach Stem. This shock structure of overexpanded nozzles is indicated to be unstable, and its location oscillates with low frequency [16].

The experimental study [17] on flow separation during startup and shutdown also reveals asymmetric flow transitions from FSS to RSS and vice versa. The investigation confirms peak side loads during this process and conducts a thorough analysis of the displacement of the separation point along the nozzle wall with the exit pressure changes. Beyond the side loads, asymmetric shock separation creates a thrust vector shift, which leads to significant thrust variations that can negatively impact the rocket's trajectory characteristics [16].

1.2.3 Flow Separation Theoretical Prediction Criteria

As the rocket industry has developed, the speed characteristics and performance of rocket nozzles have improved, increasing the need for a theoretical method capable of predicting the location and conditions of flow separation. However, a universal formula for this prediction does not currently exist. This is due to different behavior of flow separation, which depends on multiple factors such as nozzle shape and geometry, environmental conditions, working gas, initial conditions, and etc. Over the past century, various criteria have been created, allowing to approximately determine the location and condition of flow separation. However, each of them is based on experimental data from specific case studies.

Stark [18] provides a comprehensive review of the literature on highly overexpanded flows in rocket nozzles, highlighting the main existing criteria for predicting flow separation. The author identifies five key periods in the historical development of this phenomenon study, conducts a comparative analysis of the existing models, and notes that the technical progress have improved the accuracy of experimental results. The main separation criteria in his work are presented in Table 1.1.

Table 1.1: Separation criteria [18].

	Separation criterion
Arens & Spiegler	$\frac{p_{sep}}{p_p} = \frac{\left[1+\frac{\kappa-1}{2}Ma_{sep}^2\left(1-k_A^2\right)\right]\left\{0.5Ma_{sep}^2\left[(\kappa+1)k_A^2-\frac{(\kappa-1)^2}{\kappa+1}\right]-\frac{\kappa-1}{\kappa+1}\right\}^{\frac{1}{\kappa-1}}}{\left[\frac{\kappa+1}{2}Ma_{sep}^2\cdot k_A^2\right]^{\frac{\kappa}{\kappa-1}}}$ $k_A = \frac{u}{U_\infty} \sim 0.6$
Frey	$\frac{p_{sep}}{p_p} = \left(1+\frac{2\kappa}{\kappa+1}\left[Ma_{sep}^2\cdot\sin^2(44.5^\circ - 4.7^\circ\cdot Ma_{sep}) - 1\right]\right)^{-1}$
Kalt & Badal	$\frac{p_{sep}}{p_a} = \frac{2}{3}\left(\frac{p_c}{p_a}\right)^{-\frac{1}{5}}$
Schilling	$\frac{p_{sep}}{p_a} = 0.583\left(\frac{p_c}{p_a}\right)^{-0.195}$; suggested for short bell type nozzles
Schmucker	$\frac{p_{sep}}{p_a} = \left(1.88Ma_{sep} - 1\right)^{-0.64}$
Summerfield & McKenney	$\frac{p_{sep}}{p_a} = 0.34\ldots0.4$; $\gamma = 1.25$; for $Ma_{sep} = 2.84 - 3.36$ $\frac{p_{sep}}{p_a} = 0.38\ldots0.41$; $\gamma = 1.4$; for $Ma_{sep} = 2.92 - 3.32$
Zukoski	$\frac{p_{sep}}{p_p} = \frac{2}{Ma_{sep}+2}$; Forward-Facing Step
Stark	$\frac{p_{sep}}{p_a} = \frac{1}{Ma_{sep}}$; for turbulent flows

The authors of the criteria used different notations for physical parameters, some of which were standardized later. The variable κ represents the specific heat ratio γ, Ma_{sep} denotes the separation Mach number, and k_A is the velocity ratio between the current velocity u and the freestream velocity U_∞ in the work of Arens & Spiegler and Frey. Additionally, p_{sep} represents the separation pressure and p_p is the plateau pressure.

1.2.4 Computational Fluid Dynamics (CFD) Approaches

Computational fluid dynamics (CFD) is the science of using computers to predict liquid and gas flows based on the governing equations of conservation of mass, momentum, and energy [19]. CFD methods offer a number of advantages in solving complex technical and physical problems. One of the main benefits is cost and time savings compared to traditional experimental approaches. The concept of CFD is to mathematically predict fluid flow behavior by solving the governing equations, namely the continuity equation, the conservation of momentum, and the conservation of energy. However, the CFD modeling is a complex process and demands an expertise in fluid and gas dynamics. Additionally, any CFD model must be validated with theoretical and, preferably, experimental data.

Although there are many existing approaches to solving fluid flow on a computer, the fundamental principles of CFD modeling include the following steps [19]:

1. Defining and creating the geometry of the fluid flow domain.
2. Discretizing the domain into a mesh of a specific size.
3. Assigning physical models and boundary conditions to different regions, followed by numerical computation.

Modern studies of flow separation in overexpanded nozzles using CFD programs [16], [20], [21], and [22] mostly use models based on the Reynolds-averaged Navier Stokes (RANS) equations. In the RANS approach, the starting point is the Reynolds decomposition of the flow variables into mean and fluctuating parts. Substituting the decomposed variables into the Navier-Stokes equations and averaging of the equations themselves, gives rise to the Reynolds-stress tensor - an unknown term that has to be modeled in order for the RANS equations to be solved. Special models have been developed, such as the shear stress transport (SST) model, k-ε, k-ω, and etc., for the flows where a turbulence presences. These models are designed to take into account the eddy viscosity parameter. The concept involves solving equations for the renormalized velocity field (large scales) that account for the influence of the removed small scales through eddy viscosity. Eliminating only the smallest scales leads to subgrid-scale closures in Large Eddy Simulation (LES), while removing larger scales results in Reynolds-stress models [23]. For a more accurate analysis of highly turbulent flows, nonlinear Reynolds-stress tensor models can be employed to consider nonlinear eddy viscosity.

1.2.5 Modern Advances in Nozzle Design and Flow Control

To date, a lot different approaches have been proposed to enhance nozzle efficiency by mitigating and delaying flow separation in overexpanded nozzles. These methods are categorized into two types: active and passive. The most common passive methods involve modifying the nozzle by building up an additional expanding contour at the nozzle exit section or incorporating a specially shaped internal structure inside the nozzle to streamline the jet flow. Among the advanced nozzle concepts, the following stand out [24]:

- Dual-bell nozzle: A combination of a TIC nozzle for operation at sea level and low altitudes, and a TOP contour for higher altitudes.
- Aerospike nozzle: A nozzle with a central spike inside that compresses exhaust gases by interacting with ambient pressure during flight.
- Expansion-deflection nozzle: Similar to the aerospike nozzle, with an internal structure that expands exhaust gases around a central pintle. This theoretically reduces the base-drag and the pressure losses due to flight velocity.

Active methods require additional energy, which can be either directly supplied from the working fluid itself or from an external source. For example, Alvi [25] investigated the effect of second microjet injection on supersonic flow behavior that disrupts the shear layer and reduces instability within supersonic jet flows.

Zaheer [16] considers a control method of asymmetric flow separation in overexpanded supersonic nozzles using the Coanda effect. The study proposes a change to the nozzle throat geometry to tilt the sonic plane, causing the Coanda effect and changing the flow behavior.

Schneider [26] examines active flow control using film cooling and adjustments of mixture ratio. The author's findings indicate that a cooling film with a specific mass flow rate reduces the pressure ratio in the secondary nozzle section. This alteration accelerates the transition to high-altitude flight conditions.

Despite the extensive number of scientific papers on flow control and flow separation mitigation methods, none of these approaches have been widely implemented in real spacecraft designs. This further emphasizes the need for continued research in this area.

1.3 Project Proposal

The main objective of this project is to develop, model, and study the pressure distribution along the contour of an overexpanded nozzle. The research focuses on examining the effects of heat transfer and flow conditions both inside and outside the boundary layer. Additionally, this research aims to evaluate the flow separation affects on engine performance and structural integrity. The findings will contribute to the improvement of nozzle designs to increase efficiency and reliability.

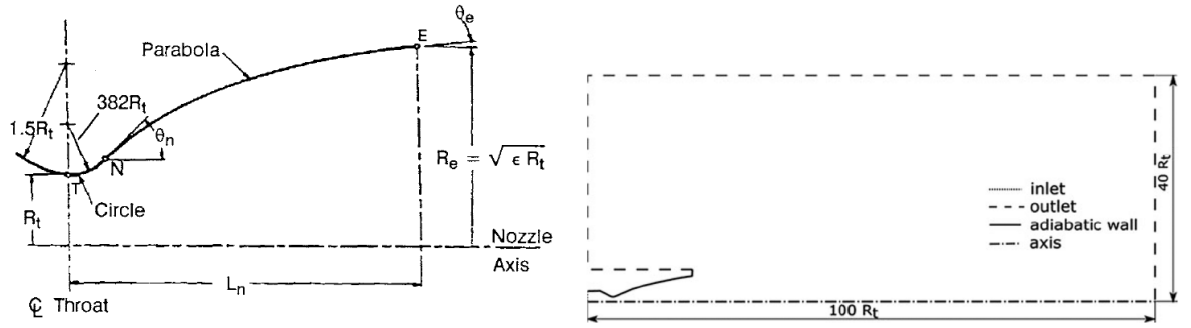
1.4 Methodology

The initial stage requires preparation for CFD analysis. Following the fundamental principles of CFD modeling, the first step involves the development of the fluid flow domain. Geometry creation is performed using CAD programs to accurately model the nozzle geometry and the controlled volume.

To create the preliminary two-dimensional (2D) geometry, Eqs.1.1-1.8 for an ideal flow are used. A 2D geometry significantly simplifies the computational process and the mesh creation. A full 2D section of the nozzle represents a planar simulation that does not take into account certain three-dimensional (3D) spatial properties. However, a 2D half-section cut along the nozzle's centerline enables an axisymmetric analysis, which includes the three-dimensional nature of the object.

For the nozzle's geometric dimensions, the method of characteristic dimensions is used. A calculation example of the method is presented in [8], and the resulting geometry is shown in Fig.1.9a. The contour curvature is calculated using MATLAB software based on ideal flow calculations within the nozzle. The design must be taken with consideration of parameters such as design Mach number, throat section size, combustion chamber dimensions, exit radius, divergent section length, and parabolic-contour wall angles. These parameters can also be calculated using Eqs.1.1-1.8 and from Table 1.1.

The initial geometries will include five different nozzles with five different area ratios ranging from 12 to 20 in increments of 2. An example of the nozzle's geometry with the controlled volume is shown in Fig.1.9b.



(a) Parabolic approximation of bell nozzle contour [8].

(b) Full geometry model example [22].

Figure 1.9: Project geometry example.

Once the geometry is prepared, the next step is to generate the mesh. For this, the built-in mesh designer in ANSYS Fluent is used. The quality of the mesh impacts the computational results and must be defined properly for the specific problem. Turbulent flows are significantly affected by walls, where the viscosity-affected regions have large gradients in the solution variables. An accurate presentation of the near-wall region is essential for successfully predicting wall-bounded turbulent flows. It is recommended to use the computed wall y^+ when working with such flows [27]. The dimensionless quantity y^+ refers to the distance from a wall to the center of the first computational cell. The parameter y^+ is determined by the following three formulas.

$$y^+ = \frac{u_\tau y}{\nu} \tag{1.9}$$

Where ν is the kinematic viscosity of the fluid, y represents the absolute distance from the wall, and u_τ is the friction velocity, defined by Eq.1.10.

$$u_\tau = \sqrt{\frac{\tau_w}{\rho}} \tag{1.10}$$

Where ρ represents the fluid density, and τ_w is the wall shear stress, calculated using the following equation:

$$\tau_w = \frac{1}{2} C_{fric} \rho U_\infty^2 \tag{1.11}$$

Where C_{fric} is the skin friction coefficient, and U_∞ is the freestream velocity. The recommended wall y^+ value is in the range between 30 and 60 to determine sufficient accuracy in predicting flow behavior [27].

The numerical study will be performed in ANSYS Fluent using RANS-based turbulence models. A literature review shows that the SST k-ω model is suitable for capturing shock waves in this type of problem. Pressure values are assigned to the inlet and outlet boundaries of the fluid domain. The outlet pressure of the surrounding volume will remain constant, while the inlet pressure will change. Therefore, multiple simulations will be compiled for different PR values ranging from 4 to 22.

For a more detailed study of the flow separation phenomenon, transient simulations will be conducted taking into account the flow development. Using a sufficiently small time step, it is possible to capture details of the shock wave formation near the wall.

The simulation results must be compared and validated with additional data. Ideally, the simulation would be based on existing experimental data. However, for preliminary validation, a comparative analysis of CFD results with a theoretical model developed using a criterion is sufficient.

Chapter 2 - Nozzle Design

Rocket nozzle design is a crucial part of engine development. It affects flow behavior, thrust performance, engine weight, and overall mission success. The design process requires balancing fluid dynamics with manufacturing technologies. Engineers determine the nozzle geometry using mathematical calculations. Among them, the most common approaches are the method of characteristics (MOC) and Rao's method.

The method of characteristics, founded in the early 19th century, is based on solving partial differential equations (PDEs). This technique transforms PDEs into systems of ordinary differential equations (ODEs) along characteristic curves or surfaces, commonly termed as characteristics. Once the ODEs are determined, they can be solved along the characteristic lines. The solution can then be converted back to the original PDE. Today, MOC is widely used in fluid dynamics to solve hyperbolic PDEs, helping to understand flow propagation and shock waves.

In rocket nozzle design, the method of characteristics is used to solve the fundamental Navier–Stokes equations in various interpretations. Today, the method is widely utilized to calculate steady, two-dimensional, planar, and axisymmetric irrotational supersonic flow. The analysis of such flow requires the following assumptions:

- Steady flow. Flow parameters such as velocity, pressure, and density at a specific point remain constant over time.
- Two-dimensional flow. Flow parameters vary only in two spatial dimensions (e.g., x and y).
- Planar and axisymmetric flow. Planar flow assumes the motion occurs in a two-dimensional plane, while axisymmetric flow assumes a fluid motion is symmetric around a central axis, reducing a three-dimensional problem to a two-dimensional one.
- Irrotational flow. Fluid elements are not subject to rotation, meaning their motion is purely translational.
- Supersonic flow. The flow velocity exceeds the local speed of sound a, meaning the Mach number M is greater than one.

Additional assumptions for this type of flow include:

- Isentropic flow. The isentropic process includes both adiabatic (no heat added or removed from the system) and reversible (no dissipative phenomena).
- Compressible flow. The density of the flow is a variable quantity.
- Inviscid flow. Viscous effects are neglected.

However, the method of characteristics can be modified for other flow types, such as unsteady one-dimensional flow, steady three-dimensional isentropic flow, and unsteady two-dimensional isentropic flow, and others. The governing equations of these flows are hyperbolic, meaning they form a well-posed problem of partial differential equations with known initial conditions. For hyperbolic equations, the flow properties at each point in the flow field depend on those properties in a finite region of the upstream flow field, but are independent of the downstream conditions [28], [29].

From a physical point of view, the characteristic line represents the path along which a physical disturbance propagates. In supersonic flow, such disturbances travel along Mach lines at the local speed of sound. Since the local Mach number M, and flow direction angle vary throughout the nozzle, characteristic lines are typically curved. In other words, in a supersonic flow, the characteristic lines correspond directly to the Mach lines.

For the design of supersonic nozzles, the MOC determines the nozzle wall profile from a shock-free isentropic expansion design. This is a sequential numerical procedure that begins at the nozzle throat, where the flow has sonic initial conditions ($M = 1$). It then proceeds downstream of the throat by calculating the Mach numbers M, the Mach angle μ_M, the expansion angle through the Prandtl-Meyer expansion wave $\nu(M)$, and the flow angle θ. This chapter presents the necessary equations for steady, two-dimensional, axisymmetric, irrotational flow.

2.1 Quasi-One-Dimensional Flow

Before applying the method of characteristics, it is important to establish a set of governing equations and necessary functions. At the initial stage, the flow through the nozzle is described by the theory of quasi-one-dimensional flow. One-dimensional flow is characterized by a change in the main flow parameters of pressure, density, temperature, and velocity along a single direction, denoted as x, while the cross-sectional area remains constant. In contrast, quasi-one-dimensional flow accounts for variations in the cross-sectional area as a function of x, as shown in Fig.2.1.

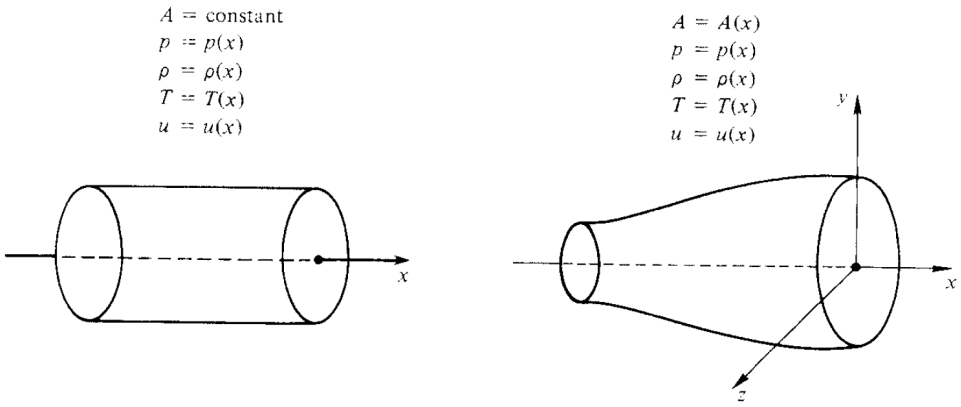


Figure 2.1: One-dimensional (left) and quasi-one-dimensional (right) [30].

Although quasi-one-dimensional flow is an approximation of real flow in a channel with a varying cross-sectional area, the fundamental conservation equations of mass, momentum, and energy can be applied. These equations form a base for deriving the governing equations of steady quasi-one-dimensional flow through the control volume $\mathscr{V}$, illustrated in Fig.2.2.

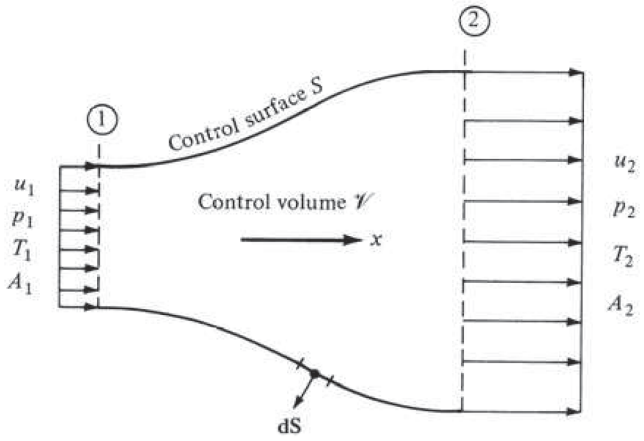


Figure 2.2: Finite control volume for quasi-one-dimensional flow [30].

Figure 2.2 illustrates the flow parameters of velocity, pressure, and temperature at the inlet section 1 and the outlet section 2. An infinite set of elementary segments dS is directed normally to the surface control surface S.

2.1.1 Continuity Equation

According to the principle of conservation of mass, mass can be neither created nor destroyed. This implies that the mass flow rate at the nozzle inlet section 1 must be equal to the mass flow rate at the outlet 2. The principle provides the first governing Navier-Stokes equation, which can be mathematically expressed in integral form as:

$$\frac{\partial}{\partial t}\iiint_{\mathscr{V}} \rho d\mathscr{V} + \oiint_{S} \rho \mathbf{V} \cdot \mathbf{dS} = 0 \tag{2.1}$$

For a steady state condition, Eq.2.1 can be reduced to its time-independent form.

$$\oiint_S \rho \mathbf{V} \cdot \mathbf{dS} = 0 \tag{2.2}$$

Applying Eq.2.2 to the control surface yields the general differential form of the continuity equation for quasi-one-dimensional flow.

$$d(\rho u A) = 0 \tag{2.3}$$

Equation 2.3 states that there is no change in mass withing the control surface. The mass flow rate, expressed as Eq.2.4, remains constant at both inlet and outlet sections, as given by Eq.2.5.

$$\dot{m} = \rho u A \tag{2.4}$$

$$\rho_1 u_1 A_1 = \rho_2 u_2 A_2 \tag{2.5}$$

2.1.2 Momentum Equation

The law of conservation of momentum states that in a closed system, the total momentum of all interacting bodies remains constant. This physical principle of Newton's second law can be interpreted as force equaling the rate of change of momentum over time. Based on the terms presented in Fig.2.2, the force originates from the pressure acting on the control surface S. The elementary surface force caused by pressure acting on an element $\mathbf{dS}$ is $-p\mathbf{dS}$. The negative sign indicates that the force acts opposite to $\mathbf{dS}$. The total pressure force is the summation of these elemental forces over the entire control surface.

Additionally, the flow has a mass momentum at both the inlet and outlet. The difference between these quantities is called the net flow of momentum out of control volume across surface S. Since the mass flow rate across the elemental area $\mathbf{dS}$ is $(\rho \mathbf{V} \cdot \mathbf{dS})$, the flow of momentum per second across $\mathbf{dS}$ is $(\rho \mathbf{V} \cdot \mathbf{dS})\mathbf{V}$. Thus, the integral form of the momentum equation for a steady flow can be written as:

$$\oiint_S (\rho \mathbf{V} \cdot \mathbf{dS})\mathbf{V} = -\oiint_S p\mathbf{dS} \tag{2.6}$$

The terms $\mathbf{V}$ and $\mathbf{dS}$ are vector quantities. Since the parameters of a quasi-one-dimensional flow change only in the x direction, Eq.2.6 can be simplified to a single x component.

$$\oiint_S (\rho \mathbf{V} \cdot \mathbf{dS})u = -\oiint_S (p\ dS)_x \tag{2.7}$$

The derivation of the differential form of the momentum equation requires considering an incremental control volume where flow properties such as pressure, velocity, and density vary along the x direction. By applying the integral momentum equation to this incremental volume and expanding the right and left terms of Eq.2.7, the conservation of momentum equation for steady, inviscid, quasi-one-dimensional flow results in Eq.2.8.

$$dp = -\rho u \, du \tag{2.8}$$

2.1.3 Energy Equation

The integral form of the energy equation for an inviscid, adiabatic, steady flow without body forces includes the total of the fluid's internal energy e and its kinetic energy. When there are no changes over time, it can be expressed as:

$$\oiint_S \rho \left(e + \frac{V^2}{2} \right) \mathbf{V} \cdot \mathbf{dS} = - \oiint_S p \mathbf{V} \cdot \mathbf{dS} \tag{2.9}$$

Applying Eq.2.9 to the control volume in Fig.2.2 and mathematically rearranging it yields the energy conservation equation for steady, adiabatic, inviscid quasi-one-dimensional flow within the control volume, given by Eq.2.10.

$$h_1 + \frac{u_1^2}{2} = h_2 + \frac{u_2^2}{2} \tag{2.10}$$

Equation 2.10 states that the total enthalpy is constant throughout the flow, since the total enthalpy is:

$$h_0 = h + \frac{u^2}{2} \tag{2.11}$$

Thus,

$$h_0 = \text{const} \tag{2.12}$$

The differential form of the energy conservation equation for a steady, inviscid, adiabatic, quasi-one-dimensional flow can be obtained by combining Eqs.2.11 and 2.12.

$$dh + u \, du = 0 \tag{2.13}$$

2.2 Isentropic Compressible Flow Relations

To understand and predict flow behavior in rocket nozzles, it is essential to outline the fundamental principles and relationships governing high-speed flow. This type of flow is characterized by two key aspects: 1) High-speed flow possesses significant energy due to its velocity, which corresponds to high kinetic energy, and 2) In high-speed flow, density is a variable quantity, classifying the flow as compressible.

In such flows, the transient conversion between kinetic and internal energy makes temperature a crucial factor. Consequently, thermodynamic laws dominate, particularly isentropic relations given by Eqs.2.16-2.19.

An isentropic flow is commonly described by the Mach number term, Eq.2.14, which is defined as the ratio of the flow speed to the local speed of sound.

$$M = \frac{u}{a} \tag{2.14}$$

Additionally, the local speed of sound depends on the local density, pressure, temperature, and the specific heat ratio of the fluid.

$$a = \sqrt{\gamma \frac{p}{\rho}} = \sqrt{\gamma R T} \tag{2.15}$$

Where R represents the specific gas constant.

By applying the equation of state for an ideal gas, the following isentropic relations can be obtained.

$$\frac{p_2}{p_1} = \left(\frac{\rho_2}{\rho_1}\right)^{\gamma} = \left(\frac{T_2}{T_1}\right)^{\frac{\gamma}{\gamma-1}} \tag{2.16}$$

Using the conservation equations of mass, momentum, and energy (Eqs.2.3, 2.8, and 2.13) with the definition of total enthalpy, Eq.2.11, the ratios of the main flow static parameters to their total quantities can be derived, as shown in Eqs.2.17-2.19.

Pressure ratio.

$$\frac{p}{p_0} = \left(1 + \frac{\gamma - 1}{2} M^2\right)^{-\frac{\gamma}{\gamma-1}} \tag{2.17}$$

Temperature ratio.

$$\frac{T}{T_0} = \left(1 + \frac{\gamma - 1}{2} M^2\right)^{-1} \tag{2.18}$$

Density ratio.

$$\frac{\rho}{\rho_0} = \left(1 + \frac{\gamma - 1}{2} M^2\right)^{-\frac{1}{\gamma - 1}} \tag{2.19}$$

However, the assumption of isentropic flow represents an ideal case and does not apply in reality to the nozzle flow region near the wall, where the boundary layer forms. In the boundary layer, the effects of the dissipative mechanisms of viscosity, thermal conduction, and diffusion cannot be ignored. Nevertheless, for the majority of the flow within the nozzle, these mechanisms have minimal impact, allowing isentropic flow to be a reasonable initial approximation for nozzle design [31].

2.3 Area–Mach Number Relation

Another important relationship in the study of flow dynamics in nozzles is the dependence of cross-sectional areas on the Mach number. This ratio is derived from the conservation equations of mass and momentum. The continuity Eq.2.3 can be transformed by expanding the differential, as shown in Eq.2.20.

$$uA\, d\rho + A\rho\, du + \rho u\, dA = 0 \tag{2.20}$$

Each term can be divided by the constant $\rho A u$, resulting in Eq.2.21 that contains the necessary ratios of area and velocity.

$$\frac{d\rho}{\rho} + \frac{du}{u} + \frac{dA}{A} = 0 \tag{2.21}$$

Equation 2.8, representing momentum conservation, can be rearranged and multiplied by $d\rho$, resulting in Eq.2.22.

$$\frac{d\rho}{\rho} = -\frac{u\, du\, d\rho}{dp} \tag{2.22}$$

The definition of the speed of sound provided by Eq.2.15 is based on the pressure derivative, which can be taken isentropically, meaning at constant entropy.

$$a^2 = \left(\frac{dp}{d\rho}\right)_{\text{Constant entropy}} \tag{2.23}$$

Substituting Eq.2.23 into Eq.2.22 yields:

$$\frac{d\rho}{\rho} = -\frac{u\,du}{a^2}$$

Multiplying the right-hand side by u/u and using the Mach number definition (Eq.2.14):

$$\frac{d\rho}{\rho} = -M^2\frac{du}{u} \tag{2.24}$$

Substituting Eq.2.24 into Eq.2.21 results in the area-velocity relation, shown in Eq.2.25.

$$-M^2\frac{du}{u} + \frac{du}{u} + \frac{dA}{A} = 0$$

$$\frac{du}{u}\left(-M^2 + 1\right) + \frac{dA}{A} = 0$$

$$\frac{dA}{A} = \left(M^2 - 1\right)\frac{du}{u} \tag{2.25}$$

Equation 2.25 describes the change in flow velocity du as a function of the change in cross-sectional area dA. The term in brackets in the equation has three main conditions:

1. Subsonic flow ($0 \leq M < 1$): an increase in velocity du is accompanied by a decrease in area dA.
2. Sonic flow at ($M = 1$): the derivative of the area $dA = 0$, which mathematically indicates a horizontal tangent that corresponds to a local maximum, a local minimum, or an inflection point. Physically, this corresponds to the minimum nozzle area.
3. Supersonic flow at ($M > 1$): the term in brackets is positive, therefore, an increase in velocity du is accompanied by an increase in area dA.

Equation 2.25 demonstrates that when the speed of sound is reached, the nozzle cross-section must increase to further accelerate the gas and achieve a supersonic condition. Therefore, in designing a supersonic rocket nozzle, it is essential to determine the minimum throat area and the nozzle exit cross-section based on the desired Mach number. For this purpose, a parameter

called the area ratio is used. The derivation of this parameter assumes that the sonic speed of a compressible isentropic flow is achieved in the nozzle throat.

To derive the area ratio equation, Fig.2.3 will be used, where the flow parameters at the throat are denoted as M^* and u^*, and the throat area is A^*. Since the flow at the throat is sonic, the Mach number is $M^* = 1$ and $u^* = a^*$. Any cross-section of the nozzle after the throat is designated as A, with the flow parameters M and u. Thus, the continuity Eq.2.3 becomes:

$$\rho u A = \rho^* u^* A^* = \rho^* a^* A^* \tag{2.26}$$

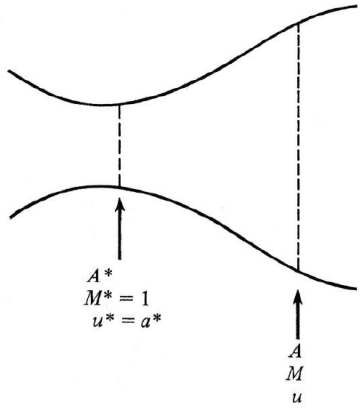


Figure 2.3: Geometry for the derivation of the area–Mach number relation [30].

Rearranging the Eq.2.26 and multiplying it by ρ_0/ρ_0 yields Eq.2.27.

$$\frac{A}{A^*} = \frac{\rho^*}{\rho_0}\frac{\rho_0}{\rho}\frac{a^*}{u} \tag{2.27}$$

Where ρ_0 is the stagnation density that remains constant throughout an isentropic flow.

From the isentropic compressible flow relation for density (Eq.2.19), the density ration at the throat area, assuming sonic conditions ($M^* = 1$), yields Eq.2.28:

$$\frac{\rho^*}{\rho_0} = \left(\frac{2}{\gamma + 1}\right)^{\frac{1}{\gamma - 1}} \tag{2.28}$$

At any other cross-sectional area, Eq.2.19 can be written as the Eq.2.29:

$$\frac{\rho_0}{\rho} = \left(1 + \frac{\gamma - 1}{2} M^2\right)^{\frac{1}{\gamma - 1}} \tag{2.29}$$

The Mach number at the throat (M^*) can be expressed as a function of Mach number M and the specific heat ratio γ:

$$M^* = \sqrt{\frac{\frac{\gamma+1}{2} M^2}{1 + \frac{\gamma-1}{2} M^2}} \tag{2.30}$$

Combining Eq.2.30 with the definition of the Mach number Eq.2.14 yields Eq.2.31:

$$\frac{a^*}{u} = \frac{1 + \frac{\gamma-1}{2} M^2}{\frac{\gamma+1}{2} M^2} \tag{2.31}$$

Squaring Eqs.2.28, 2.29, and 2.31, and substituting them into Eq.2.27 results in Eq.2.32.

$$\left(\frac{A}{A^*}\right)^2 = \left(\frac{2}{\gamma + 1}\right)^{\frac{2}{\gamma-1}} \left(1 + \frac{\gamma - 1}{2} M^2\right)^{\frac{2}{\gamma-1}} \frac{1 + \frac{\gamma-1}{2} M^2}{\frac{\gamma+1}{2} M^2} \tag{2.32}$$

Rearranging Eq.2.32 yields the final area-Mach number relation (Eq.2.33):

$$\frac{A}{A^*} = \sqrt{\frac{1}{M^2} \left[\frac{2}{\gamma + 1} \left(1 + \frac{\gamma - 1}{2} M^2\right)\right]^{\frac{(\gamma+1)}{(\gamma-1)}}} \tag{2.33}$$

Equation 2.33 presents the important dependence of Mach number M on the nozzle area ratio A/A^*. For a given area ratio A/A^*, the equation has two possible Mach numbers: subsonic and supersonic. In the subsonic condition ($M < 1$), an increase in M corresponds to a decrease in A/A^*, i.e., the channel narrows. On the contrary, in the supersonic regime ($M > 1$), an increase in M correlates with an increase in A/A^*, meaning the channel expands.

2.4 Velocity Potential Equation

In designing the diverging section of a supersonic nozzle, the method of characteristics is used to solve the fundamental equations for supersonic, steady, inviscid, and irrotational flow. The concept of irrotational flow means that fluid elements do not rotate, meaning their motion is purely translational. Mathematically, this condition is expressed as the absence of vorticity at any point in the flow.

$$\nabla \times \mathbf{V} = 0 \tag{2.34}$$

Where the vector operator ∇ is the gradient, defined in cartesian coordinates as:

$$\nabla = \frac{\partial}{\partial x}\mathbf{i} + \frac{\partial}{\partial y}\mathbf{j} + \frac{\partial}{\partial z}\mathbf{k} \tag{2.35}$$

The velocity potential, denoted as $\Phi = \Phi(x, y, z)$, is a scalar function that represents the velocity of the fluid as a function of position.

$$\nabla \times (\nabla\Phi) = 0 \tag{2.36}$$

Substituting Eq.2.36 into Eq.2.34 yields Eq.2.37, which states that for an irrotational flow, there exists a scalar function Φ such that the velocity is given by the gradient of Φ.

$$\mathbf{V} = \nabla\Phi \tag{2.37}$$

In cartesian coordinates, the velocity vector $\mathbf{V}$ is expressed as:

$$\mathbf{V} = u\mathbf{i} + v\mathbf{j} + w\mathbf{k} \tag{2.38}$$

Thus, the velocity components can be expressed by the velocity potential:

$$u = \frac{\partial\Phi}{\partial x}, \quad v = \frac{\partial\Phi}{\partial y}, \quad w = \frac{\partial\Phi}{\partial z} \tag{2.39}$$

The continuity equation.

$$\nabla \times (\nabla\Phi) = \nabla^2\Phi = \frac{\partial^2\Phi}{\partial x^2} + \frac{\partial^2\Phi}{\partial y^2} + \frac{\partial^2\Phi}{\partial z^2} = 0 \tag{2.40}$$

Combining Euler's equation 2.8 and continuity Eq. 2.3, the governing equation for steady, irrotational, and inviscid flow is reduced to the velocity potential equation.

$$\left(1-\frac{\Phi_x^2}{a^2}\right)\Phi_{xx}+\left(1-\frac{\Phi_y^2}{a^2}\right)\Phi_{yy}+\left(1-\frac{\Phi_z^2}{a^2}\right)\Phi_{zz} \\ -\frac{2\Phi_x\Phi_y}{a^2}\Phi_{xy}-\frac{2\Phi_x\Phi_z}{a^2}\Phi_{xz}-\frac{2\Phi_y\Phi_z}{a^2}\Phi_{yz}=0 \tag{2.41}$$

The assumption of two-dimensional flow reduces Eq.2.41 to the form:

$$\left(1-\frac{\Phi_x^2}{a^2}\right)\Phi_{xx}+\left(1-\frac{\Phi_y^2}{a^2}\right)\Phi_{yy}-\frac{2\Phi_x\Phi_y}{a^2}\Phi_{xy}=0 \tag{2.42}$$

Considering the relations 2.39, Eq.2.42 can be expressed by velocity components u and v.

$$\left(1-\frac{u^2}{a^2}\right)\frac{\partial u}{\partial x}+\left(1-\frac{v^2}{a^2}\right)\frac{\partial v}{\partial y}-\frac{2uv}{a^2}\frac{\partial u}{\partial y}=0 \tag{2.43}$$

2.5 Method of Characteristics for Two-Dimensional Supersonic Flow

In a supersonic flow, Eq.2.43 is hyperbolic type and can be solved by the method of characteristics. A PDE is classified as hyperbolic if the coefficients of its highest-order derivatives satisfy a certain condition. For the velocity potential equation, this condition is:

$$\frac{\left(\Phi_x^2+\Phi_y^2\right)}{a^2}>1 \quad \text{or equivalently} \quad M^2>1 \tag{2.44}$$

A hyperbolic equation is characterized by the existence of certain directions (or lines) in the $x-y$ plane, called characteristics. For the velocity potential equation, characteristics correspond to Mach lines.

The normal derivatives of the velocity components (i.e., second derivatives of the velocity potential) are indeterminate on a characteristic and may even be discontinuous, whereas the velocity itself (i.e., first derivatives of the velocity potential) is continuous. Along a characteristic, the velocity potential satisfies a certain relation known as the compatibility equation.

In two-dimensional flow, where $\Phi = \Phi(x, y)$, the following relations can be defined.

$$du = d\Phi_x = d\left(\frac{\partial \Phi}{\partial x}\right) = \frac{\partial^2 \Phi}{\partial x^2} dx + \frac{\partial^2 \Phi}{\partial x \partial y} dy \tag{2.45}$$

$$dv = d\Phi_y = d\left(\frac{\partial \Phi}{\partial y}\right) = \frac{\partial^2 \Phi}{\partial y^2} dy + \frac{\partial^2 \Phi}{\partial x \partial y} dx \tag{2.46}$$

Equations 2.43, 2.45, and 2.46 represent three equations with the three second derivatives unknown. These equations can be solved using Cramer's rule.

$$\Phi_{xy} = \frac{\partial^2 \Phi}{\partial x \partial y} = \frac{\begin{vmatrix} 1 - \frac{u^2}{a^2} & 0 & 1 - \frac{v^2}{a^2} \\ dx & du & 0 \\ 0 & dv & dy \end{vmatrix}}{\begin{vmatrix} 1 - \frac{u^2}{a^2} & -\frac{2uv}{a^2} & 1 - \frac{v^2}{a^2} \\ dx & dy & 0 \\ 0 & dx & dy \end{vmatrix}} = \frac{N}{D} \tag{2.47}$$

Where N and D represent the numerator and denominator determinants, respectively.

Figure 2.4 illustrates the geometry of a streamline, with dx and dy directed away from point A, as well as the initial velocity $\mathbf{V}$ at a certain flow angle θ and velocity components du and dv. At a particular location of point A in space, Fig.2.4, Φ_{xy} has a specific value, and general choices of dx and dy point away from this location. Along the line formed by dx and dy, the velocity changes with particular du and dv. Regardless of the choice of this line, the associated values of change in velocity will ensure that Φ_{xy} remains constant.

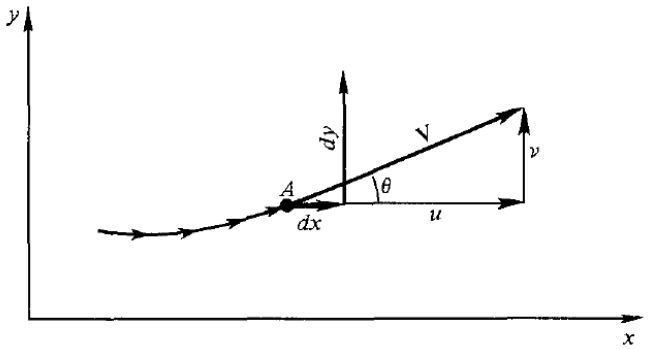


Figure 2.4: Movement of point A along the streamline [30].

However, a particular line in space, given by particular values of dx and dy, leads to $D = 0$. Since it is known that Φ_{xy} cannot physically be infinite at this location, then $N = 0$ to keep Φ_{xy} finite.

$$\Phi_{xy} = \frac{\partial u}{\partial y} = \frac{\partial v}{\partial x} = \frac{N}{D} = \frac{0}{0} \tag{2.48}$$

The velocity derivatives are indeterminate in the directions created by dx and dy. These lines in space are the characteristic lines, where the derivatives of velocity are indeterminate. The equations to create these lines can be obtained by setting $D = 0$.

$$\left(1 - \frac{u^2}{a^2}\right)(dy)^2 + \frac{2uv}{a^2}dxdy + \left(1 - \frac{v^2}{a^2}\right)(dx)^2 = 0$$

$$\left(1 - \frac{u^2}{a^2}\right)\left(\frac{dy}{dx}\right)^2_{\text{char}} + \frac{2uv}{a^2}\left(\frac{dy}{dx}\right)_{\text{char}} + \left(1 - \frac{v^2}{a^2}\right) = 0 \tag{2.49}$$

Where $\left(\frac{dy}{dx}\right)_{\text{char}}$ is the slope of the characteristic line. Equation 2.49 can be solved as a quadratic equation.

$$\left(\frac{dy}{dx}\right)_{\text{char}} = \frac{-\frac{uv}{a^2} \pm \sqrt{\frac{u^2+v^2}{a^2} - 1}}{1 - \frac{u^2}{a^2}} \tag{2.50}$$

Equation 2.50 describes the slope of the characteristic line in space. Knowing from Fig.2.4 that $u = V\cos\theta$ $v = V\sin\theta$ and considering the supersonic condition Eq.2.44, there are two real solutions to this equation.

$$\left(\frac{dy}{dx}\right)_{\text{char}} = \tan\left(\theta \mp \mu_M\right) \tag{2.51}$$

Where μ_M is the local Mach angle and is defined by Eq.2.52.

$$\mu_M = sin^{-1}\left(\frac{1}{M}\right) \tag{2.52}$$

In other words, there are two characteristic lines passing through any point, which are also Mach lines as presented in Fig.2.5. The left-running $\theta + \mu_M$ line is denoted as C_+ characteristic, and the right-running $\theta - \mu_M$ line is C_- characteristic.

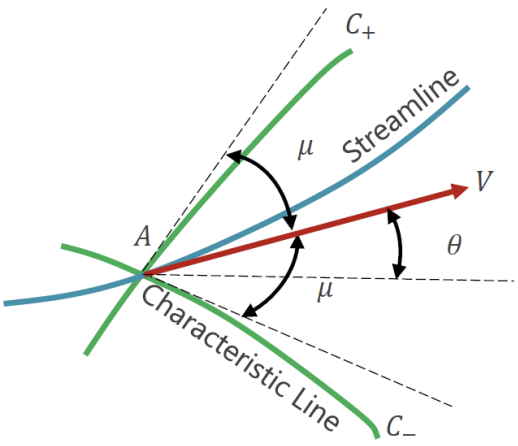


Figure 2.5: Left- and right-running characteristic lines through point A [32].

Characteristic lines are curved in space because the local Mach angle μ_M depends on the local Mach number M, which is a function of both x and y. Moreover, the local streamline direction θ also varies throughout the flow.

2.5.1 Compatibility Equations

Along the characteristic lines, the governing partial differential equation that describes the flow reduces to ordinary differential equations known as compatibility equations. These equations can be found by setting the numerator determinant to zero, $N = 0$.

$$\left(1 - \frac{u^2}{a^2}\right) du dy + \left(1 - \frac{v^2}{a^2}\right) dx dv = 0$$

$$\frac{dv}{du} = \frac{-\left(1 - \frac{u^2}{a^2}\right)}{1 - \frac{v^2}{a^2}} \frac{dy}{dx} \tag{2.53}$$

Recognizing the slope of the characteristic line dy/dx and substituting it into Eq.2.51, the following ODEs can be obtained.

$$d\theta = \mp\sqrt{M^2 - 1}\frac{dV}{V} \tag{2.54}$$

Equation 2.54 is called the compatibility equations and describes how the flow changes along characteristic lines, relating changes in direction θ to the changes in velocity magnitude **V**. Equation 2.54 can be integrated to obtain a result in terms of the Prandtl-Meyer function $\nu(M)$.

$$\theta + \nu(M) = \text{const} = K_- \quad \text{(along } C_- \text{ line)} \tag{2.55}$$

$$\theta - \nu(M) = \text{const} = K_+ \quad (\text{along } C_+ \text{ line}) \tag{2.56}$$

Where K_- and K_+ are different constants along the characteristic lines C_- and C_+.

Prandtl-Meyer function is:

$$\nu(M) = \sqrt{\left(\frac{\gamma+1}{\gamma-1}\right)} \tan^{-1} \sqrt{\left[\frac{\gamma-1}{\gamma+1}\left(M^2-1\right)\right]} - \tan^{-1}\sqrt{\left(M^2-1\right)} \tag{2.57}$$

As the flow exits the nozzle throat, expansion waves are formed as the flow expands to fill the space of the diverging region of the nozzle. The expansion waves accelerate toward the curved geometry of the wall, causing a change in the local gas density. The expansion waves are then compressed to allow the flow to pass through the same angle as the wave reflects off the nozzle wall.

The result of the compression of the expansion waves is the sound waves. They are the result of small disturbances in the flow, i.e., the density, as the mean flow accelerates in the direction of the speed of sound in the divergent part of the nozzle. The wall geometry is the sum of the characteristic points along the upper and lower walls of the wind tunnel that together expand the flow to the desired supersonic conditions with uniformity.

2.5.2 Unit Processes

Internal Point

Once the flow angle θ and Mach angle μ_M at two points are known, the parameters at the third can be determined. Figure 2.6 illustrates the intersection of the left-running C_+ and right-running C_- characteristics, which meet at point 3.

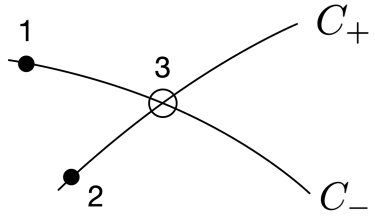


Figure 2.6: Intersecting left-running and right-running characteristics at point 3 [33].

The angles for the third point can be calculated using the known values of K_+ and K_-, as shown in Eqs.2.58 and 2.59.

$$\theta_3 = \frac{1}{2}\left[(K_-)_1 + (K_+)_2\right] \tag{2.58}$$

$$\nu_3(M) = \frac{1}{2}\left[(K_-)_1 - (K_+)_2\right] \tag{2.59}$$

Having determined the Prandl-Meyer angle $\nu_3(M)$, the Mach number at the third point M_3 can be obtained using the inverse Prandl-Meyer function. Knowing the Mach number, the pressure, temperature, and density at the third point can be determined using the isotropic relations of these parameters given in Eqs.2.17-2.19. An important assumption in determining the location of point 3 is that the characteristics are straight lines, whereas in reality, they are curved. However, a greater number of characteristic lines provides higher accuracy. Thus, the slope of the characteristics is approximated by the average value of the parameters from the previous two points, as presented in Eqs.2.60 and 2.61.

$$\text{slope } C_- = \left[\frac{1}{2}(\theta_1 + \theta_3) - \frac{1}{2}(\mu_{M1} + \mu_{M3})\right] \tag{2.60}$$

$$\text{slope } C_+ = \left[\frac{1}{2}(\theta_2 + \theta_3) - \frac{1}{2}(\mu_{M2} + \mu_{M3})\right] \tag{2.61}$$

Wall Point

The nozzle wall contour has an expanding section and a straightening section. As the flow exits the throat section, it expands and forms expansion waves. To design a nozzle without shock waves, the flow must expand to the maximum expansion angle of the design Mach number. Therefore, the maximum wall angle θ_w of the nozzle will be half of the expansion angle. This will be the first known geometric parameter of the nozzle.

$$\theta_{w,max} = \frac{\nu(M_{des})}{2} \tag{2.62}$$

Figure 2.7 illustrates a single right-running characteristic through point 4 that intersects the wall at point 5.

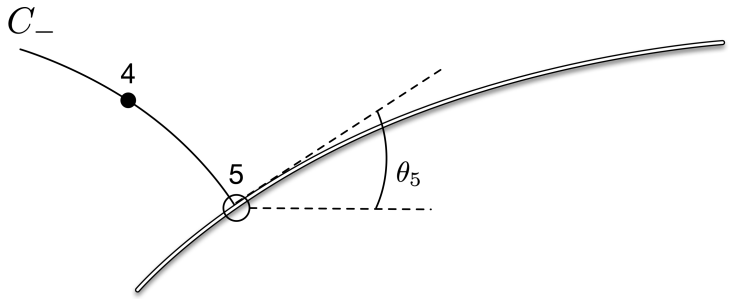


Figure 2.7: Characteristic line intersecting with a point 5 on a solid wall [33].

The parameters of point 4 are known, and accordingly, the values of K_- for C_- at this point are also known. The wall angle is derived from the maximum expansion angle. Thus, the

only unknown parameter is the expansion angle at point 5, which can be calculated using the compatibility equation (Eq.2.63).

$$(K_-)_4 = \theta_4 + \nu_4(M) = (K_-)_5 = \theta_5 + \nu_5(M) \tag{2.63}$$

$$\nu_5(M) = \nu_4(M) + \theta_4 - \theta_5$$

The remaining parameters of point 5 are calculated using a similar method after determining the Mach number at the point from the inverse Prandtl-Meyer function.

Minimum-Length Nozzle Design

This section presents the results of an example design for a minimum-length nozzle with an exit Mach number of 2.5 and air as the working gas, with a constant specific heat ratio of 1.4. The nozzle geometry calculation is performed in the MATLAB environment, and the detailed code is presented in Appendix A. The code is based on the method described by Anderson [30] and on the code written by S. Maurya [34].

The design of the nozzle geometry begins with determining the desired design Mach number M_{des} at the nozzle exit and the specific heat ratio γ. With these two parameters, the maximum wall expansion angle θ_{max} can be calculated. Additional initial data is the number of characteristic lines. A greater number of lines results in a more accurate calculation. This method has shown convergence with theoretical calculations of the throat and exit areas ratio, Eq.2.33, when designing with 50 characteristics.

Figure 2.8 and Table 2.1 show an example and the results of calculating a minimum-length nozzle using three characteristics to demonstrate the method.

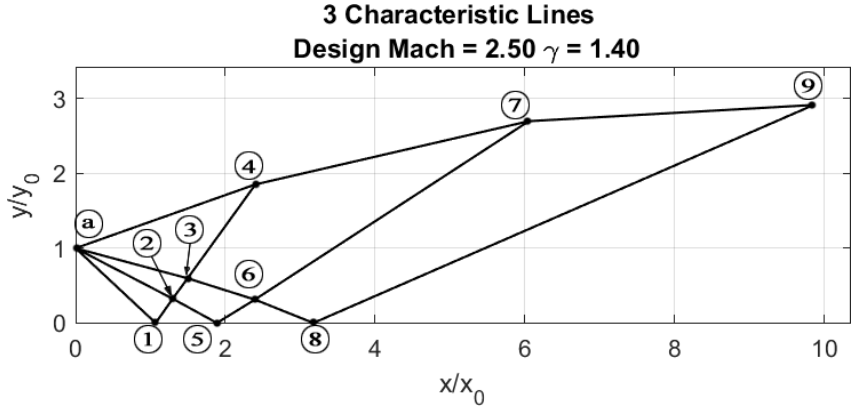


Figure 2.8: Three characteristics and corresponding nodes.

The calculation is performed dimensionlessly with the throat radius set to one. Leaving the throat (point a in Fig.2.8), the flow passes a sharp corner and expands, forming expansion waves that are directed toward the centerline of the nozzle ($y = 0$). As the flow passes through the nozzle, the gas elements collide with only two wave systems: right-running waves emanating

Table 2.1: Example of MOC calculation for three characteristic lines.

Point no.	K_- (deg)	K_+ (deg)	θ (deg)	$\nu(M)$ (deg)	M	μ_M (deg)
1	13.04	0	6.52	6.52	1.31	49.62
2	26.08	0	13.04	13.04	1.54	40.54
3	39.12	0	19.56	19.56	1.76	34.63
4	39.12	0	19.56	19.56	1.76	34.63
5	26.08	-26.08	0	26.08	1.99	30.18
6	39.12	-26.08	6.52	32.60	2.23	26.59
7	39.12	-26.08	6.52	32.60	2.23	26.59
8	39.12	-39.12	0	39.12	2.5	23.58
9	39.12	-39.12	0	39.12	2.5	23.58

from point a, and left-running waves emanating symmetrically from the point a' (not shown in the Figure). Thus, the calculation is performed for internal points 1, 2, 3, 5, 6, and 8 at the intersection of characteristics, and for points near the wall (4, 7, and 9). Axial points 1, 5, and 8 are calculated based on the symmetry of the nozzle, so the known first point upstream is used as the second known point. For example, to calculate point 5, the parameters of point 2 are used twice.

By increasing the number of characteristic lines, the nozzle slightly decreases in the exit diameter, which improves the accuracy of the geometric parameters calculations. Figure 2.9 illustrates 20 characteristics for the same initial parameters of Mach number and γ.

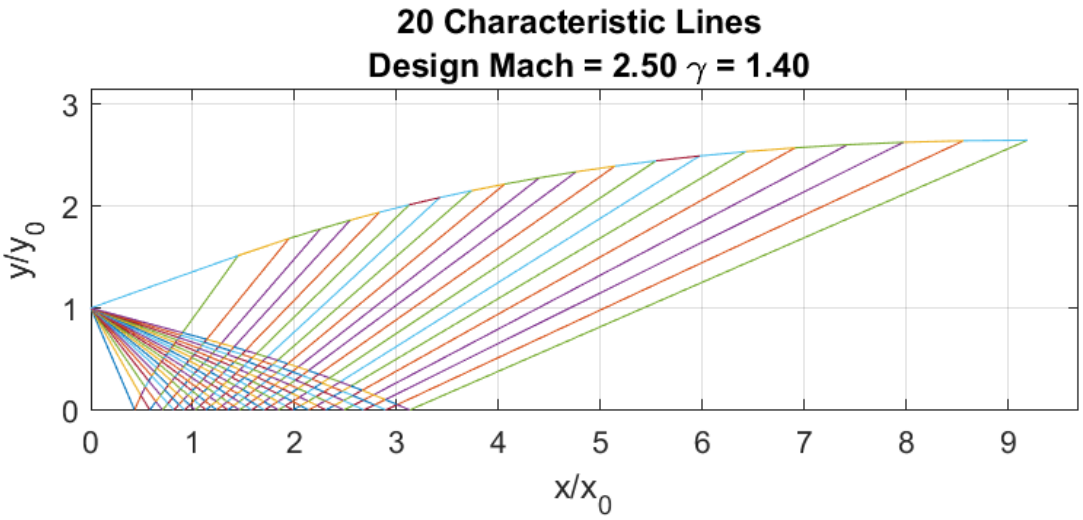


Figure 2.9: Minimum-length nozzle design for Mach number 2.5 and $\gamma = 1.4$.

The resulting nozzle contour for 50 characteristics is shown in Fig.2.10, where the internal lines of the characteristics are removed.

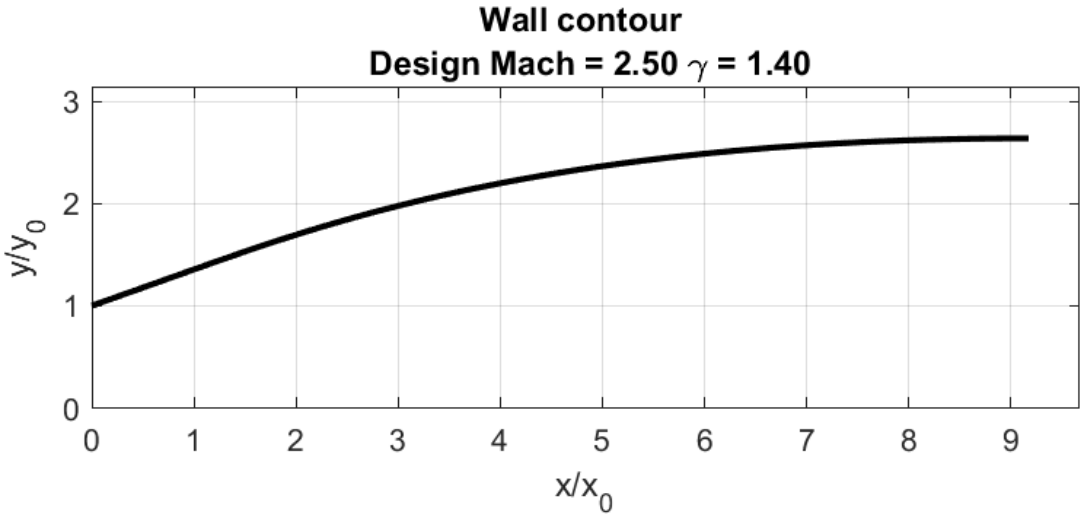


Figure 2.10: Minimum-length nozzle wall contour for Mach number 2.5 and $\gamma = 1.4$.

Chapter 3 - Preliminary CFD Modeling

The objective of this chapter is to perform a preliminary computational fluid dynamics (CFD) analysis on a simplified nozzle geometry. This will help to gain insight into how the flow separation phenomenon occurs in supersonic nozzles. Choosing an appropriate numerical model is important in subsequent work on more complicated contours.

3.1 Initial 2D Nozzle CAD Design

The preliminary model employs a conical nozzle geometry to reduce computational complexity while still capturing essential flow features. The use of a conical nozzle simplifies mesh generation, as the divergent section is a straight line instead of a parabolic curve. Despite this simplification, the important flow physics, including shock structures and recirculation zones, can be captured with the appropriate boundary conditions.

The nozzle operates in the overexpanded regime, where the nozzle exit pressure is lower than the ambient pressure. This condition triggers the occurrence of flow separation. According to the Summerfield criteria [35], the separation occurs when the exit pressure is approximately 40% of the ambient pressure.

3.1.1 Geometry

The dimensions of the conical nozzle were obtained following the method described by Huzel and Huang [8], which is based on empirical data and the fundamental relations governing ideal gas flow. The procedure for obtaining the dimensional values is described below and presented in Table 3.1 and Fig.3.1.

Given standard sea-level ambient pressure (p_a), the required pressure at the nozzle exit p_e for the formation of flow separation can be determined using the Summerfield criterion:

$$p_e = 0.4\, p_a \tag{3.1}$$

With the specific heat ratio γ of the working gas known, and the stagnation pressure in

the combustion chamber p_c set, the theoretical nozzle expansion ratio (ε) can be calculated as follows:

Given the throat radius and using the formula for the area of a circle, the nozzle expansion ratio, Eq.1.4, can be used to determine the radius of the nozzle exit area R_e:

$$R_e = \sqrt{\frac{\varepsilon A_t}{\pi}} \tag{3.2}$$

A primary section of this project is the divergent part of the nozzle. In addition to the throat and exit radii, the section is defined by the divergent cone half-angle α_c, which usually has a standardized value of 15 degrees. Using the cone angle, the length (L_n) of the divergent section from the throat to the exit can be determined:

$$L_n = \frac{R_t(\sqrt{\varepsilon} - 1) + R_{con}\,(\sec\alpha_c - 1)}{\tan\alpha_c} \tag{3.3}$$

Where R_{con} is the contour radius of arc near the throat and typically ranges from 0.5 to 1.5 times the throat radius R_t [8].

The determination of the remaining nozzle dimensions, such as the combustion chamber radius R_c, length L_c, and the converging angle θ_c, are described in detail in Chapter 4 of the Huzel and Huang textbook. These parameters are derived using the method of the characteristic length L^*, which involves a determination of the contraction area ratio ε_c. The dimensions are applied to the CAD model illustrated in Fig.3.1, created using SolidWorks software.

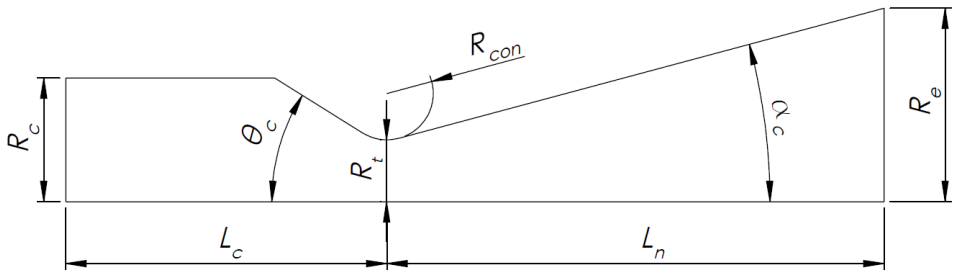


Figure 3.1: Conical nozzle contour.

Computational fluid dynamics modeling requires creating a computational domain in addition to the nozzle geometry, as shown in Fig.3.2. The computational domain consists of 60 throat radii in length ($60R_t$) and 20 throat radii in width ($20R_t$). Additionally, it includes boundary sections where boundary conditions will be assigned later. The boundaries include the centerline, inlet, walls, and outlet. The nozzle exit, also shown in Fig.3.2, is defined as an internal line within the computational domain.

Table 3.1: Dimension parameters of conical nozzle design.

Parameter	Notation	Value	Units
Ambient pressure	p_a	101325	Pa
Specific heat ratio	γ	1.22	-
Chamber pressure	p_c	506625	Pa
Exit pressure	p_e	40530	Pa
Area ratio (A_e/A_t)	ε	2.57	-
Throat radius	R_t	0.05	m
Throat area	A_t	0.008	m^2
Exit area	A_e	0.021	m^2
Exit radius	R_e	0.081	m
Divergent cone half-angle	α_c	15	deg
Divergent length	L_n	0.402	m
Characteristic length	L^*	1.143	m
Chamber volume	V_c	0.009	m^3
Convergent cone half-angle	θ_c	32.0	deg
Contraction ratio (A_c/A_t)	ε_c	4	-
Combustion area	A_c	0.008	m^2
Chamber radius	R_c	0.1	m
Chamber length	L_c	0.26	m
Contour radius	R_{con}	0.075	m

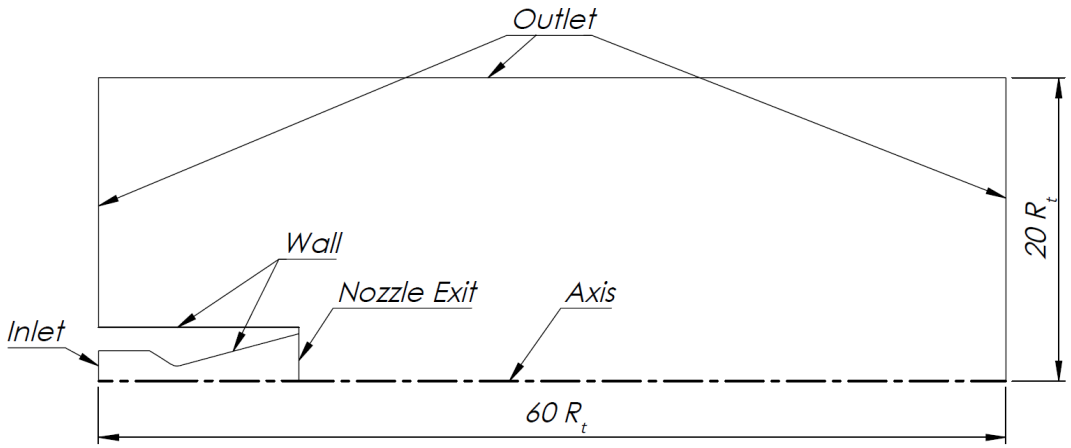


Figure 3.2: Conical nozzle with computational domain.

3.2 CFD Modeling

3.2.1 Mesh

The next step after the CAD design is to discretize the computational domain into a computational mesh. Figures 3.3 and 3.4 show the generated structured mesh that consists of quadrilateral elements obtained using a combination of meshing tools integrated into ANSYS software.

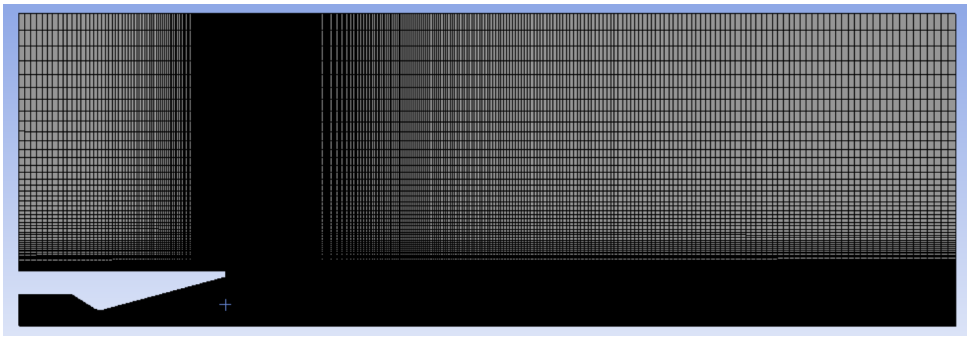


Figure 3.3: Computational mesh.

The main mesh detailing is focused on the nozzle geometry, where the element size is set to 0.1 mm. The mesh density is increased near the nozzle walls using the optional Bias tool, with the bias factor values ranging from 30 to 50, to better capture boundary layer development and potential flow separation. Figure 3.4 illustrates an example of the mesh distribution in the nozzle section.

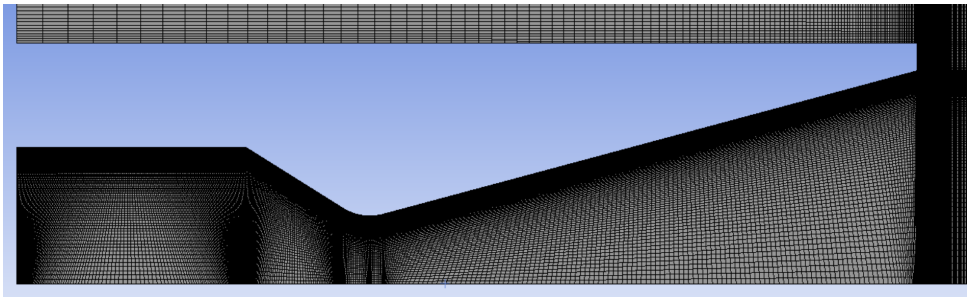


Figure 3.4: Meshed nozzle section.

3.2.2 Problem Setup

General and Models

The initial model configuration is defined as a pressure-based solver with an absolute velocity formulation. Additionally, the modeling is steady, 2D, and axisymmetric.

The Models tab in ANSYS Fluent defines physical models that represent the primary effects that influence flow behavior. The Energy model is used to simulate heat transfer within the computational domain. When enabled, Fluent solves the energy equation, taking into

account the conduction and convection properties of the physical flow. The energy model allows for analyzing temperature changes in the flow.

The Viscous model section is used to define the turbulence model. The k-omega model is a two-equation turbulence model that calculates the turbulent kinetic energy k and the specific dissipation rate ω.

The k-ω SST model is widely used due to its robustness and accuracy in predicting flow separation and adverse pressure gradients. The model uses a hybrid calculation approach for different regions. It applies the standard k-ω model near the walls to resolve the boundary layer with a viscosity limiter to prevent overestimation of wall shear stress, improving separation predictions.

Material

The Materials tab defines and configures the properties of the working gas or liquid. In the preliminary simulation, air is used as the working gas with the following key properties:

- Density ρ: defined as an ideal gas.
- Specific heat C_p: defined using NASA 9 Piecewise Polynomial function that employs a 9-coefficient polynomial to establish the dependence of the coefficient on temperature.
- Viscosity μ: defined by Sutherland's law that introduces a temperature-dependent model.
- Thermal conductivity k_{th}: a constant value of 0.0242 W/(m·K)
- Molecular weight M_w: a constant value of 28.96 kg/kmol.

Boundary Conditions

Referring to Fig.3.2, several lines represent boundary conditions. Preliminarily, the only variable parameter is the inlet pressure, which is used to analyze flow separation behavior. The inlet pressure corresponds to the combustion chamber pressure, and the simulations differ from each other by the nozzle pressure ratio (PR). The pressure ratio is defined as the chamber total pressure (p_0) divided by the ambient pressure (p_a).

$$\mathrm{PR} = \frac{p_c}{p_a} \tag{3.4}$$

Additionally, the inlet boundary has a thermal condition with a temperature of 3000 K and a supersonic/initial gauge pressure that can be predicted using Eq.1.5 at the throat, Eq.3.5:

$$p_t = p_c \left(\frac{2}{\gamma + 1} \right)^{\frac{\gamma}{\gamma - 1}} \tag{3.5}$$

The remaining boundary conditions are:

- Outlet:
  - Pressure: standard ambient pressure at sea level, 101325 Pa.
  - Temperature: standard ambient temperature at sea level, 300 K.
  - Backflow turbulent intensity: 0.5 %.
  - Backflow turbulent viscosity ratio: 2.
- Wall:
  - Adiabatic solid wall with no-slip condition.

The axis line in Fig.3.2 is assigned as the axis line in the axisymmetric solver. In addition, the operating pressure is set to zero to ensure correct calculation of the gas density. The influence of gravitational forces is also neglected.

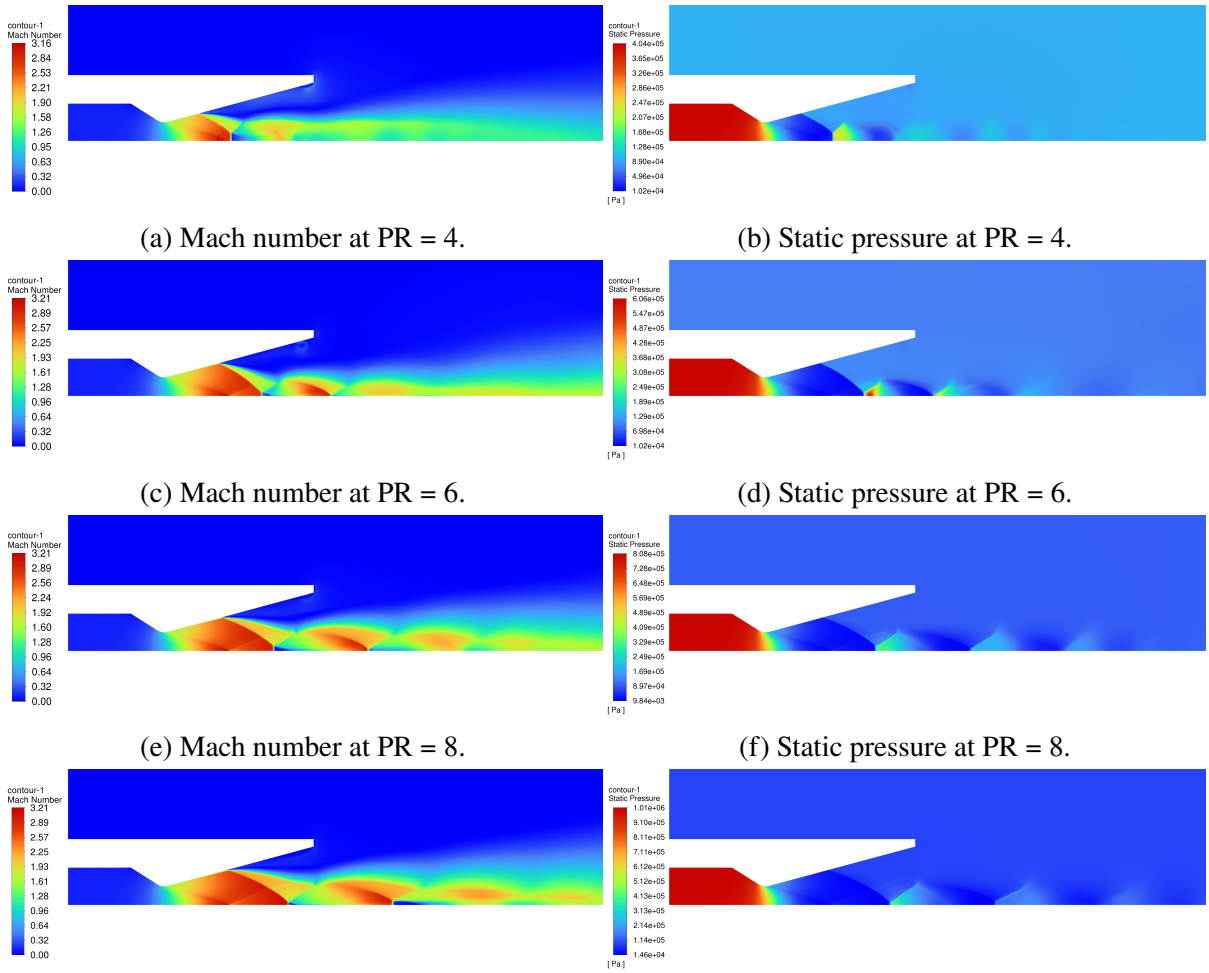
Solution Methods

The Solution Methods tab controls the major settings of the numerical schemes and algorithms used to solve the governing equations. These selected settings are:

- Scheme: Coupled.
- Gradient: Least squares cell based.
- Pressure: Second order.
- Density: Second order upwind.
- Momentum: Second order upwind.
- Turbulent kinetic energy: Second order upwind.
- Specific dissipation rate: Second order upwind.
- Energy: Second order upwind.
- Time scale factor: 0.1.
- Number of iterations: 2000.

3.2.3 Results

The driving force of the flow is the pressure difference between the nozzle inlet and the ambient pressure, defined by Eq.3.4. Simulations were conducted for PR values of 4, 6, 8, and 10. Figure 3.5 presents the Mach number and static pressure contours for each PR case.



(a) Mach number at PR = 4.

(b) Static pressure at PR = 4.

(c) Mach number at PR = 6.

(d) Static pressure at PR = 6.

(e) Mach number at PR = 8.

(f) Static pressure at PR = 8.

(g) Mach number at PR = 10.

(h) Static pressure at PR = 10.

Figure 3.5: Mach number and static pressure contours for different PR values.

The Mach number contours, Fig.3.5 (left), display an abrupt color transition from red–yellow to dark blue, indicating the location of the shock wave. This color shift reflects a substantial decrease in flow velocity after the shock, where the flow loses its accumulated momentum and becomes nearly stagnant downstream of the separation region. Similarly, the static pressure contours clearly depict the shock waves through sharp color gradients.

As the pressure ratio PR increases, the chamber pressure rises accordingly. With this increase, the flow separation point shifts downstream. This occurs because a higher-pressure gas requires a greater nozzle expansion ratio, and therefore a larger cross-sectional area. In other words, the gas travels a longer distance before reaching the critical pressure at which flow separation occurs.

The downstream shift of the flow separation point can also be observed by examining the wall pressure plot, which is shown in Fig.3.6 (right). The working gas expands after passing the

throat section (located at the coordinate $x = 0$). Reaching the separation pressure p_{sep}, a sudden pressure jump to the ambient pressure occurs. The values of the separation pressure and its ratio to the ambient pressure are presented in Table 3.2. In each PR case, the separation pressure is approximately 40% of the ambient pressure, which aligns well with the Summerfield criterion. However, a slight variation is observed at PR = 6, indicating minor sensitivity of separation behavior to boundary conditions or possibly to local mesh quality.

Table 3.2: Separation pressure and its ratio to the ambient pressure.

	PR = 4	**PR = 6**	**PR = 8**	**PR = 10**
p_{sep}, Pa	42663.1	35671.6	43660.8	44402.1
p_{sep}/p_a, %	42.1	35.2	43.1	43.8

Additionally, Fig.3.6 (left) shows the variation of the Mach number along the nozzle axis for each PR scenario. In every case, the gas accelerates from subsonic conditions within the combustion chamber, reaches sonic speed ($M = 1$) at the throat section ($x = 0$), and continues to accelerate until it encounters the shock wave. After passing through the shock, the velocity drops nearly to zero and only then begins to recover. Despite this recovery, the velocity never returns to the levels observed upstream of the shock.

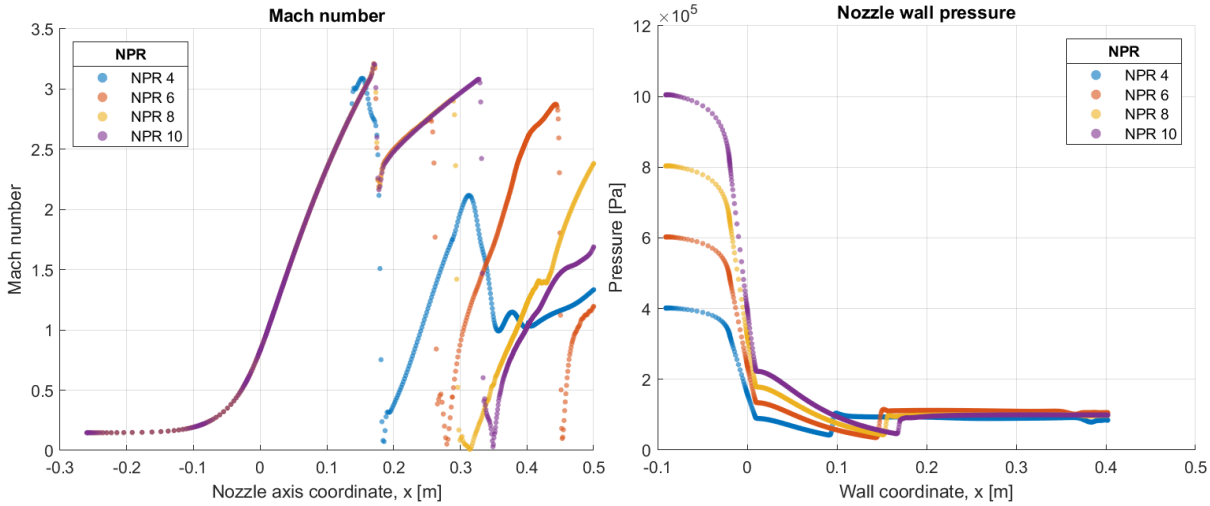


Figure 3.6: Axis Mach number (left) and nozzle wall pressure for different PR values.

These interactions with shock waves occur multiple times. The maximum flow velocity in each case is reached before the first shock, confirming that shock waves reduce the exit velocity. In turn, the exit velocity directly influences the engine thrust, as shown in Eq.1.6. Therefore, any decrease in exit velocity affects the overall performance of the rocket engine.

Chapter 4 - Mesh Generation and Validation Model Development

4.1 Sub-scale Nozzle Testing

Full-scale hot-fire tests of rocket engines under operational conditions are expensive and risky. Therefore, there is a pressing need for preliminary analysis of the product under development, which is relevant to CFD. However, CFD is not always the only way to analyze a future product. An alternative approach in experimental engineering involves creating sub-scale models identical in their characteristics to the actual setup. Such experimental models include sub-scale nozzle models, which are particularly helpful in reproducing and analyzing critical gas-dynamic phenomena under controlled conditions.

An example of this type of facility is the Cold Gas Sub-scale Test Facility P6.2, located at the German Aerospace Center in Lampoldshausen, Germany. This facility is designed for testing scaled models of rocket engine components such as nozzles and diffusers. Using the P6.2 rig, researchers have conducted numerous experiments, including investigations of flow separation in overexpanded nozzles. For example, studies of unsteady shock dynamics in a TOP nozzle by Verma [36], as well as studies of restricted shock separation in out-of-round TOP nozzles by Stark [21].

In the 1990s, the European Space Agency began actively studying flow separation due to the resulting negative side loads after analyzing several performance issues with the Vulcain engines. As part of the General Support Technology Program, experimental studies were developed and conducted by Östlund, presented in his thesis on "Side Load Phenomena in Highly Over-Expanded Rocket Nozzles", [37]. In his extensive work, Östlund, developed and tested several scaled-down models of the Vulcain TOP nozzle to replicate and evaluate side loads on the nozzle walls during engine startup and shutdown at low altitude.

4.2 Computational Model Development

Östlund's work is a comprehensive and detailed study of flow separation and the effects of operating rocket engine nozzles at low altitudes. The research is supported by numerous publications, including theoretical, CFD, and experimental developments, making it especially valuable for building a CFD validation model for this project. Through thorough descriptions of nozzle geometry, boundary and initial conditions, and published results, Östlund's research

allows for both the reconstruction of a complex physical model and the verification of its accuracy. Consequently, the VOLVO S1 nozzle model was chosen for validation and verification of the CFD simulations in this project.

4.2.1 Nozzle Geometry: VOLVO S1

The VOLVO S1 nozzle is a sub-scaled model of the real Vulcain engine nozzle, created to study and assess flow separation phenomena. The nozzle features a distinctive parabolic TOP-type profile in its divergent section. Additionally, the nozzle has a shorter length. These two design choices are intended to maximize engine thrust while reducing the nozzle's length and weight.

In the 1950s, Rao and Shmyglevsky introduced a new method for constructing a parabolic TOP contour based on an advanced MOC analysis. Their implemented approach is to adjust the control curve for the nozzle wall that was defined by a characteristic line. The control surface is determined by the assumption of achieving the maximum thrust, while the mass flow rate has a constant value [38]. The result of their work was the derivation of Rao-Shmyglevsky Eq.4.1, which significantly simplified the computational effort involved in designing bell-shaped nozzles.

$$\left(\frac{r}{R_t} + b\frac{x}{R_t}\right)^2 + c\frac{x}{R_t} + d\frac{r}{R_t} + e = 0 \tag{4.1}$$

In Equation 4.1, the coefficients b, c, d, and e are determined by five independent variables: R_d, R_e, θ_N, θ_e, and L_n. Once the independent parameters are fixed, the parabola is defined. The values of these five independent parameters were taken from Östlund's Table 7 [37] and applied to the CAD geometric model to recreate the VOLVO S1 TOP nozzle shown in Fig.4.1.

Figure 4.1 illustrates the geometry of the diverging section of a parabolic nozzle with the specified dimensions, the values of which are presented in Table 4.1.

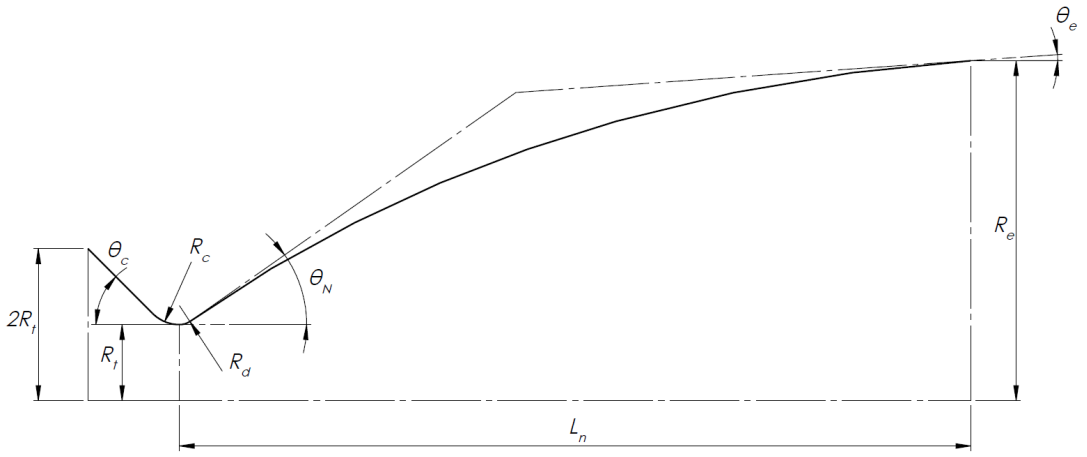


Figure 4.1: Geometry of the VOLVO S1 TOP nozzle section.

Table 4.1: VOLVO S1 divergent section dimensions.

Parameter	**Notation**	**Value**	**Units**
Area ratio (A_e/A_t)	ε	20	-
Nozzle divergent length	L_n	350	mm
Throat radius	R_t	33.54	mm
Exit radius	R_e	150	mm
Radius at converging section	R_c	16.77	mm
Radius at diverging section	R_d	8.39	mm
Throat wall angle	θ_N	35.025	deg
Nozzle exit angle	θ_e	4	deg
Convergent angle	θ_c	45	deg

The converging section does not significantly influence the flow development, therefore it is unnecessary to model this area.

Computational Domain

The computational domain was modeled to simulate a two-dimensional axisymmetric flow within the considered nozzle design. As shown in Fig.4.2, the domain extends $100R_t$ in the axial direction and $50R_t$ in the radial direction from the exit section of the nozzle. Additionally, the left boundary is moved by $30R_t$ to the left of the exit section. Such an extension is necessary to minimize any influence of the exhaust jet on the external boundaries of the ambient environment, which must remain stationary. The thickening in the region of $0.33R_t$ is introduced based on the assumption that the nozzle wall has a finite physical thickness.

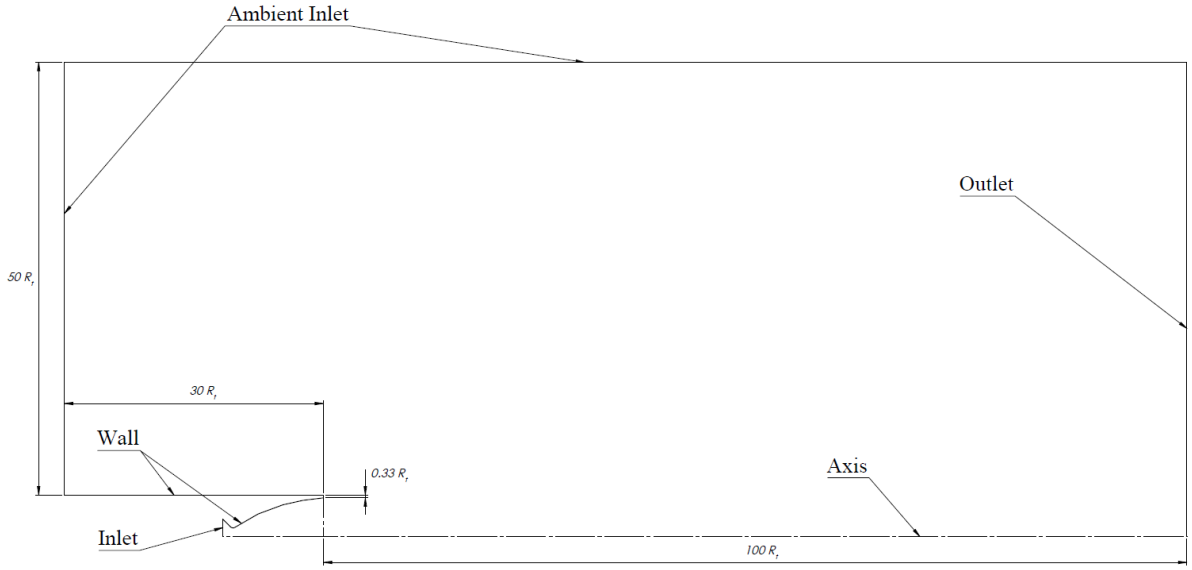


Figure 4.2: Computational domain with boundaries.

The lower dashed line represents the axis of the nozzle and the computational domain. Thus, when simulating the model with the axisymmetric assumption, the cross-section is considered circular. The leftmost line at the nozzle entrance is the inlet cross-section. The nozzle contour, along with the straight line above it, represents an adiabatic wall. The boundary lines of the computational domain are the inlet and outlet surfaces of the external atmosphere. The left and top lines represent the ambient inlet boundaries, while the rightmost line corresponds to the outlet to the environment.

4.2.2 Mesh Generation and Quality Criteria

A correct CFD computational model heavily depends on a designed mesh. As mentioned earlier, the computational volume is discretized into many elements and nodes. In turn, physical processes such as the boundary layer, expansion fans, shock-induced separation, and the separated shear layer impose additional mesh quality requirements in certain areas.

One of the main requirements for mesh construction is its structure, meaning that the grid elements must be in hex (3D) or quad (2D) shape. Transformed PDEs take a simpler form on orthogonal grids due to the orthogonal lines perpendicular to each other. This orthogonality results in better convergence and higher accuracy. Therefore, representing a physical model

with a structured grid offers several advantages, and it is preferable for problems involving strong local gradients of physical phenomena.

The advantages of a structured mesh can be clearly illustrated using a boundary layer as an example. A fluid flow forms a boundary layer due to the no-slip condition assumption. This assumption means that the flow is stationary on a rigid wall surface, which creates the boundary condition V= 0. At the same time, the average velocity in the flow core will be non-zero. From a physical point of view, the boundary layer has a very small thickness, δ, relative to other dimensions. The thickness usually does not exceed a few millimeters. Therefore, within this relatively thin layer near the wall, the flow velocity changes in a perpendicular direction sharply from zero to hundreds of meters per second. Moreover, other physical processes, such as heat flux and wall shear, can vary across the boundary layer in an even greater range. Thus, the boundary layer imposes strict requirements on the computational grid that include increased cell density, which increases the number of computational grid points, high orthogonality to the boundary, which ensures the correct direction of change in physical gradients, low skewness, and overall smoothness. Important metrics for tracking a proper mesh creation usually include:

- Skewness - measures how much a mesh element deviates from its ideal symmetrical shape. The skewness value should approach 0.
- Orthogonality - defined by the angle between the line connecting the centers of two adjacent elements and the normal to the common edge between them. The orthogonality quality value should approach 1.
- Aspect ratio - measures the deviation of an element from an ideal shape with equal sides. Aspect ratio is defined as the ratio of the largest element size to the smallest. The ratio values should ideally be close to 1, although higher values are acceptable in boundary layer regions.
- Smoothness - measures the uniformity of the mesh and is determined by the percentage change in element size. The smoothness value should not exceed 20% between adjacent elements.
- y^+ - determines the height of the first mesh layer near the wall. It is determined by the flow characteristics according to Eq.1.9. To properly capture the physics of the boundary layer, the y^+ value should be less than 1.

Block-Structured Topology of the Computational Grid

Generating a mesh of complex geometry that meets the quality requirements can be challenging. Complex geometry may include sections featuring fillet radii, sharp corners, quadratic curves, and other nonlinear segments. In this project, the nozzle contour is considered a complex geometry due to its radii at the nozzle throat and the parabolic curve of the diverging cross-section.

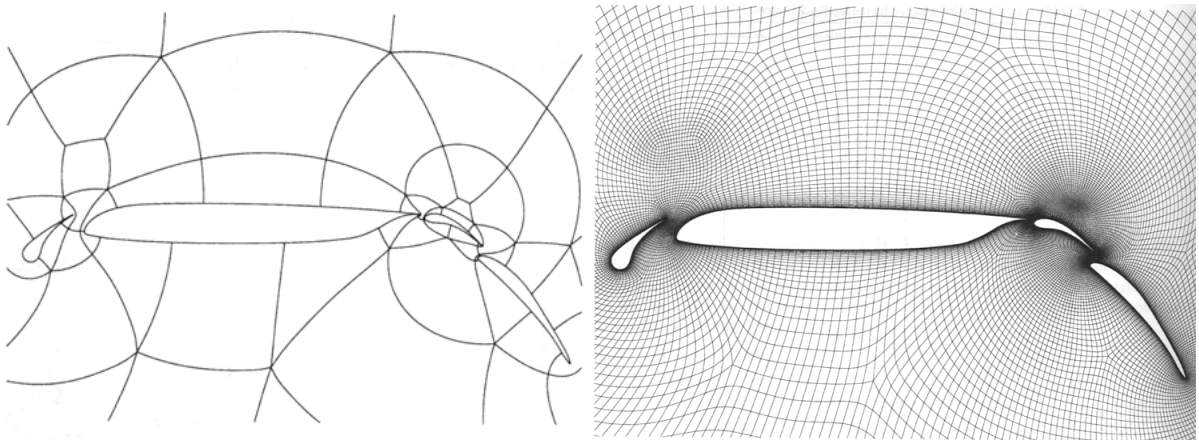
When generating the mesh, the computational algorithm must determine the slopes, curvature, and boundary guides to uniformly distribute the mesh cells and nodes. When attempting to mesh the solid model shown in Fig.4.2, a distribution conflict occurs due to the nozzle contour's different curve slopes and alternating line directions. As a result, the solver

generates a mesh that does not meet the minimum requirements of the CFD computational framework. Therefore, the original CAD model is unsuitable for mesh generation and requires modification.

To address this problem, a method exists for structuring the geometry and subsequently structuring the elements of the computational mesh. The study of geometric properties and spatial relations that remain unaffected by the continuous change in shape or size is called topology. Topology is also applicable to describing the logical structure of connected cells of a computational mesh – that is, how grid points and cells are arranged and connected to each other. This topic has been the subject of numerous studies, leading to the development of standard mesh construction methods such as algebraic, elliptic, hyperbolic, and adaptive techniques. These numerical methods are embedded in the computational code that propagates and populates the mesh with nodes. Therefore, mesh generation using the hyperbolic method is accomplished by solving hyperbolic PDEs. However, each method depends on boundary conditions, so a physical model must be initially prepared properly.

One of the most common methods for preparing a mesh for structuring is the block-structured grid technique. This method involves dividing a complex geometric configuration into simpler sections, ideally square (in 2D) or hexagonal (in 3D). Each section or subregion of the composite mesh must have outer block boundaries whose lines intersect as close as possible to a 90° angle. In this way, complex geometry is described by simpler geometry, which makes it easier to maintain high orthogonality. Subsequently, a structured mesh is generated within each block, and the submeshes can then be connected using common interfaces [39].

The initial and fundamental step in processing the physical model is defining the outer mold line (OML). The OML defines the external appearance of the geometric structure. Designing such lines is commonly used in the aerodynamic design of aircraft, wings, and fuselages. Furthermore, the OML defines characteristics and serves as an important source of information for creating a detailed design of the interior of parts. Figure 4.3a shows a detailed decomposition of the plane around four airfoils into a block structure.



(a) Block structure of a four-element airfoil. (b) Structured grid for a four-element airfoil.

Figure 4.3: Example of a block structure for a complex geometry with the corresponding structured mesh [39].

Each block surrounding an airfoil is defined primarily by the OML outline. The area around the airfoil is then divided into sections that approximate rectangular shapes as closely as possible. This division takes into account the complexity of the airfoil surface geometry. The final block shape is subsequently influenced by the curvatures, directional changes, bends, and edge rounding of each airfoil. The result is a set of blocks, within which rectangular cells are subsequently generated, as shown in Fig.4.3b.

Block Structure Implementation

The nozzle geometry was created in two-dimensional space, followed by the creation of a plane for axisymmetric simulation. The CAD was developed using SolidWorks Academic Edition 2025. The geometry was constructed based on the dimensions presented in Table 4.1 and utilizing basic built-in SolidWorks tools such as lines, arcs, circles, splines, and other modification features for adjusting and refining the drawing.

The divergent parabolic curve was created using the spline tool and constrained by geometric references to the throat wall angle θ_N and nozzle exit angle θ_e. Next, an OML was defined as an offset line of the nozzle's outer contour and the outer wall line above the nozzle contour. This was done to preserve an identical control volume of the boundary layer near the walls.

After, the blocks were created for the entire fluid domain, including the nozzle region. The overall view of the block-structured fluid domain is shown in Fig.4.4.

The nozzle block structure was developed and implemented in the CAD model and is shown in Fig.4.5. The nozzle consists of 14 internal blocks. Additionally, there are 11 blocks created outside the nozzle section to control the mesh in the outer fluid domain. The primary criterion for creating a new block was that each transition curve of the nozzle contour must have a guiding boundary. Since the nozzle has a straight, converging section at the inlet with an angle greater than 90°, it was decided to bisect the α angle. The throat region was then divided into two sections based on the number of fillet radii at the throat. The diverging section of the



Figure 4.4: Block-structured computational domain.

nozzle was divided into four block sections because the parabolic curve has a large curvature slope and requires more control volumes.

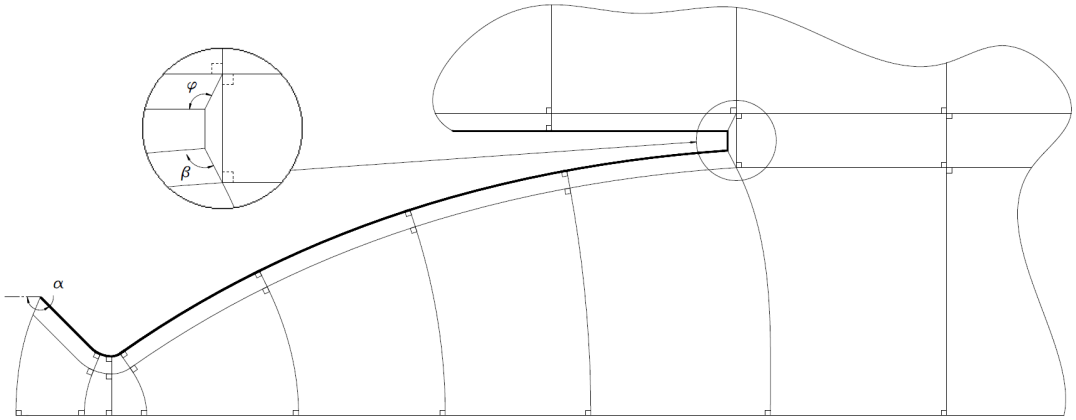


Figure 4.5: Block-structured nozzle section and surrounding regions.

The most challenging area is the edge region at the nozzle outlet, highlighted in a detailed view in Fig.4.5. When constructing a structured square mesh, points of uncertainty in the wall boundary condition can arise at sharp edge corners. In CFD practice, it is recommended to avoid such points and move them deeper into the computational mesh, away from the boundary. Accordingly, the sharp edges were separated by angles β and φ, both greater than 90°. Another reason for defining this region and the angles is to preserve a control boundary layer region along the model walls. Therefore, only two structural blocks were not implemented as rectangular. The remaining line intersections are at 90° and are indicated by the right-angle symbol in Fig.4.5.

Mesh Generation Strategy

The mesh was generated using ANSYS Academic Edition 2021, with its built-in basic mesh element control tools:

- Face Meshing - applicable to two-dimensional faces, allowing the generation of a structured "mapped" mesh filled with quadrilaterals.
- Sizing - a tool for determining the mesh size. Applicable to edges, faces, and bodies, it allows specifying an element size or the number of divisions of an object.
  - Bias factor - a sub-tool of Sizing that controls the distance between elements. Applicable to edges, it defines the ratio of the largest element size to the smallest.

Using these tools makes it possible to control both the cell location, size, and density. First, all face surfaces are assigned as Face Meshing so that the solver fills the block volume with only quadrilateral cells. Next, each face surface must be divided into a specified number of divisions using the Edge Sizing tool. Additionally, within Sizing, mesh refinement in a certain direction and the refinement ratio are configured using the Bias Type and Bias Factor parameters, respectively. Detailed assignments of block division parameters for the mesh are presented in Fig.4.6 and Table 4.2.

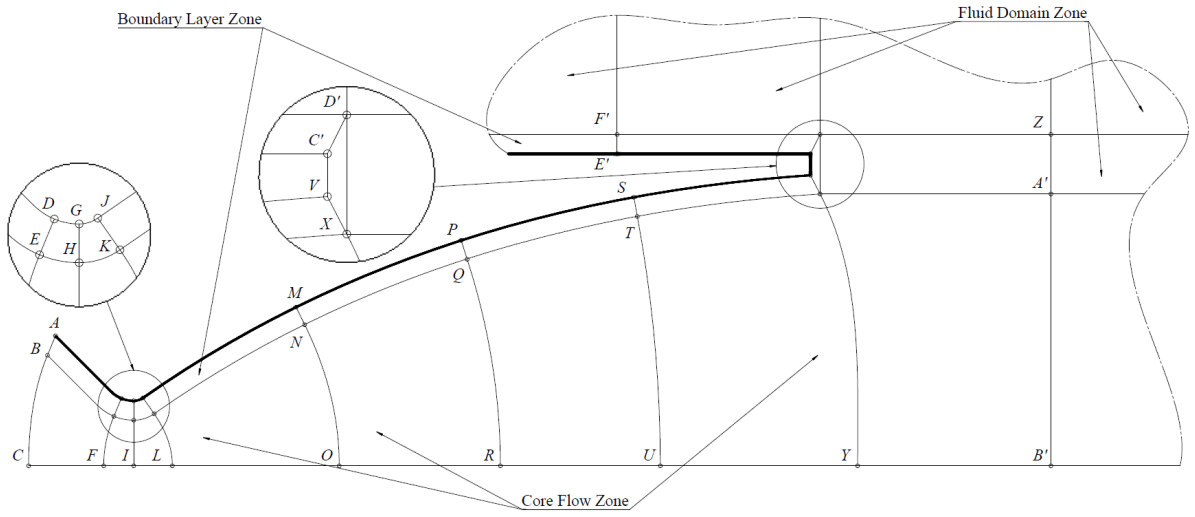


Figure 4.6: Mesh control strategy for the nozzle section.

It is important to note that the number of divisions must remain consistent across the mesh in each zone to avoid solver conflicts during generation. However, some generation errors may still occur even when an adequate division distribution is assigned. In such cases, it is recommended to set the Sizing assignment behavior to Hard type.

Table 4.2: Mesh division and bias parameters for each segment.

Zone name	Segments	Bias factor	Number of divisions
Boundary Layer	DE, GH, JK, MN, PQ, ST, VX, E'F'	632	100
	AB, C'D'	692	
Core flow zone	BC	1	100
	EF, HI	–	
	KL	–	
	NO	3	
	QR	3	
	TU	3	
	XY, A'B'	3	
Horizontal edges	AD, BE, CF	1.5	40
	DG, EH, FI, GJ, HK, IL	–	16
	JM, KN, LO	–	150
	MP, NQ, OR, PS, QT, RU, SV, TX, UY	–	150
Fluid domain zone	VC', XD', A'Z	–	40

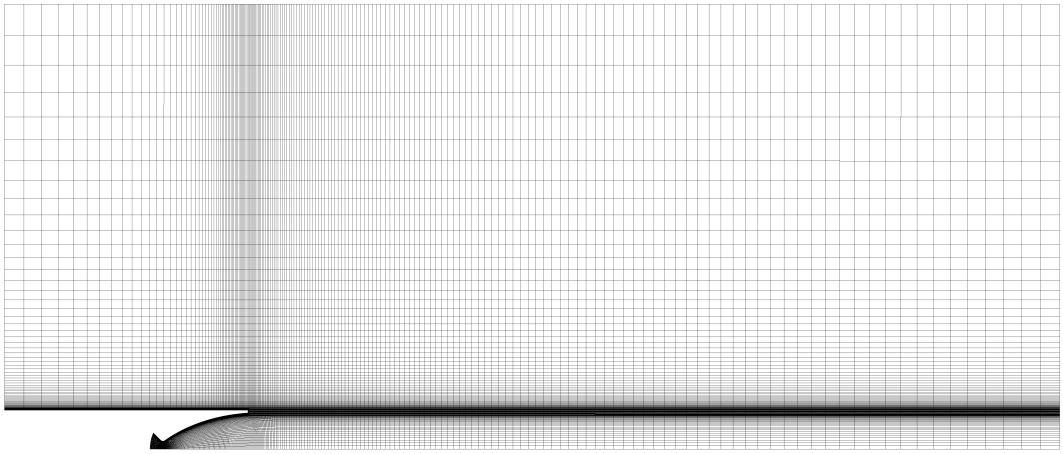
The bias direction should be oriented toward the nozzle walls to refine the mesh near the no-slip boundary condition. The bias direction for segments JM, KN, and LO is set toward the nozzle throat to improve mesh orthogonality in this region. Fluid domain segments not shown in Table 4.2 and Fig.4.6 were divided as follows:

- 60 divisions with a bias factor of 120 for vertical lines,
- 30 divisions with a bias factor of 12 for horizontal lines on the left side of the fluid domain, and
- 100 divisions with a bias factor of 9 for horizontal lines on the right side.

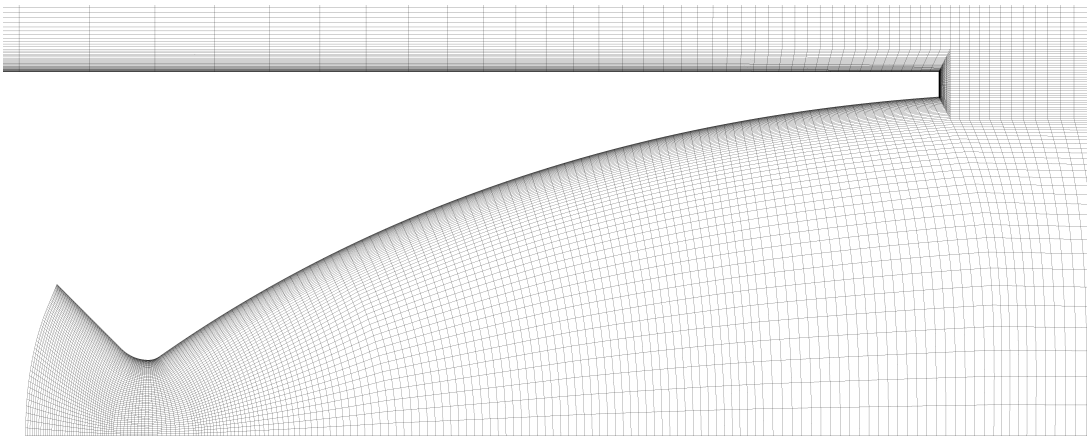
The bias direction for all unspecified lines is assigned toward the nozzle outlet, as this region is dominated by strong flow gradients.

Quality Metrics and Resulting Mesh

The resulting mesh, shown in Fig.4.7, contains 181,999 elements (including the fluid domain). The least successful characteristics are as follows: a minimum orthogonal quality equal to 0.475 in the edge region of the nozzle outlet, a maximum skewness of 0.67 also in the sharp-edge region, a maximum aspect ratio of 782 on the left side of the fluid domain, and the first layer height of 10^{-6} m along the wall, which corresponds to $y^+ \approx 1$.



(a) Fluid domain mesh.



(b) VOLVO S1 nozzle mesh.

Figure 4.7: Computational mesh for the VOLVO S1 nozzle design (every fourth line is shown).

The computational mesh shown in Fig. 4.7 represents the coarse mesh from the set of generated meshes used for subsequent CFD model verification. This mesh has lower resolution and fewer elements. However, it more clearly demonstrates the distribution pattern of the elements and the structure of the mesh – features that are consistently maintained in the higher-quality meshes discussed in greater detail later in the project.

Chapter 5 - CFD Setup, Verification, and Validation

In modern engineering, CFD represents the merger of theoretical and experimental science with the use of advanced computing tools. Therefore, when considering any CFD model in isolation, it is essential to keep in mind two fundamental factors: how closely the CFD model reflects the physical model, and how numerically reliable the solution is. Taking these two factors into account reduces the risk of errors, limits the risk associated with the development and approval of projects, and enables the development of reliable models.

From a scientific perspective, these two factors are reflected in the concepts of Verification and Validation (V&V) [40]:

- Verification - The process of determining that a model implementation accurately represents the developer's conceptual description of the model and the solution to the model.
- Validation - The process of determining the degree to which a model is an accurate representation of the real world from the perspective of the intended uses of the model.

5.1 Overview of CFD Verification and Validation

There is an entire separate field dedicated to V&V, with a branch devoted to CFD. Nevertheless, the simplified concept can be reduced to a few steps: to create a reliable CFD model, it is necessary to verify the correctness and repeatability of the equation solutions, and it is also necessary to validate that the equations being solved are suitable for the specific problem.

5.1.1 CFD Verification

Verification confirms the reliability of the computational results. In CFD, results are achieved by solving PDEs equations in the model grid or mesh. This means that the equations are solved at each node and element of the discretized computational volume, taking into account the boundary and operational conditions.

The primary objective of verification is to quantify errors in the computational model, such as insufficient spatial discretization convergence, insufficient temporal discretization convergence, lack of iterative convergence, and computer error. This process primarily relies on

comparing the computational solution to the correct answer, which is provided by what we call "highly accurate solutions" [40]. Applicable to finite difference, finite volume, and finite element methods, the most common and important verification process is the systematic refinement of the grid size. This method is known as a grid independence study or grid convergence. The goal of this process is to estimate the discretization error of the numerical solution.

A physical volume can theoretically be divided into an infinite number of infinitely small elements. Since it is impossible to achieve physically and numerically, model discretization is limited by the size and number of elements. Accordingly, the greater the number, the more accurately the model is described, the fewer intermediate and final quantitative errors, and consequently, the more accurate the result.

The standard method for determining mesh convergence is performed on two or more successively refined meshes [41]. Systematically refined meshes must have a constant refinement factor. Richardson extrapolation is used to estimate the order of accuracy.

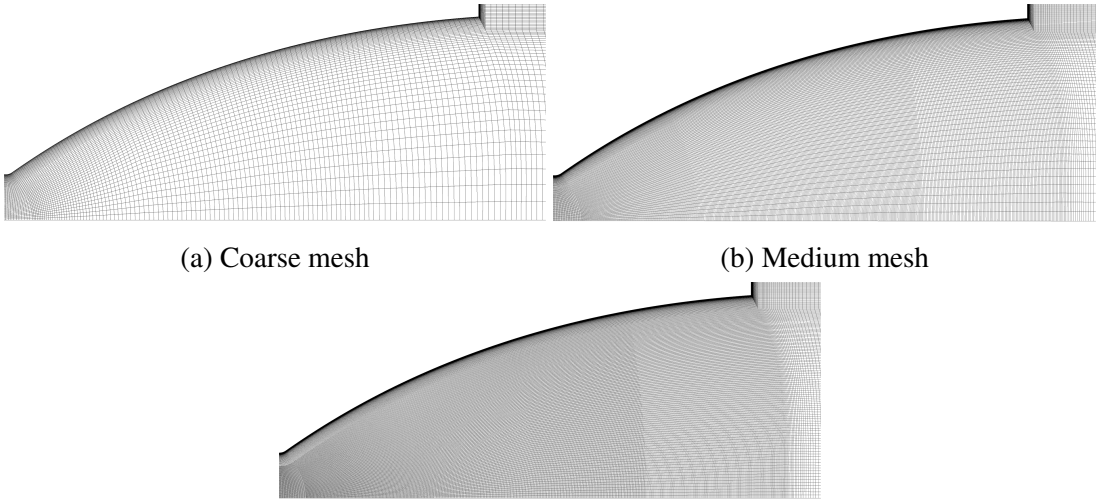
The standard method to perform a grid convergence study is to generate three grid levels: coarse, medium, and fine. This approach is widely used, simple, and does not require significant additional computational costs. For a more detailed analysis of grid convergence, it is preferable to increase the number of grid levels. The methodology involves systematically creating smaller or larger grids by removing every second grid line in each coordinate direction, and the number of grid nodes in a given direction is described by the equation:

$$N = 2^n m + 1 \tag{5.1}$$

Where N is the number of points along a specific direction, m is an arbitrary integer defining the refinement of the mesh, and n is the number of levels. For a two-level grid, Eq.5.1 becomes:

$$N = 4m + 1 \tag{5.2}$$

Three meshes were generated for the grid independence study, as shown in Fig.5.1.



(a) Coarse mesh

(b) Medium mesh

(c) Fine mesh

Figure 5.1: Three grid levels.

The parameters for each grid level are presented in Table 5.1. The height of the first grid layer for the medium and fine grid types was maintained at 10^{-6}m to keep the y^+ parameter close to 1.

Table 5.1: Grid level parameters.

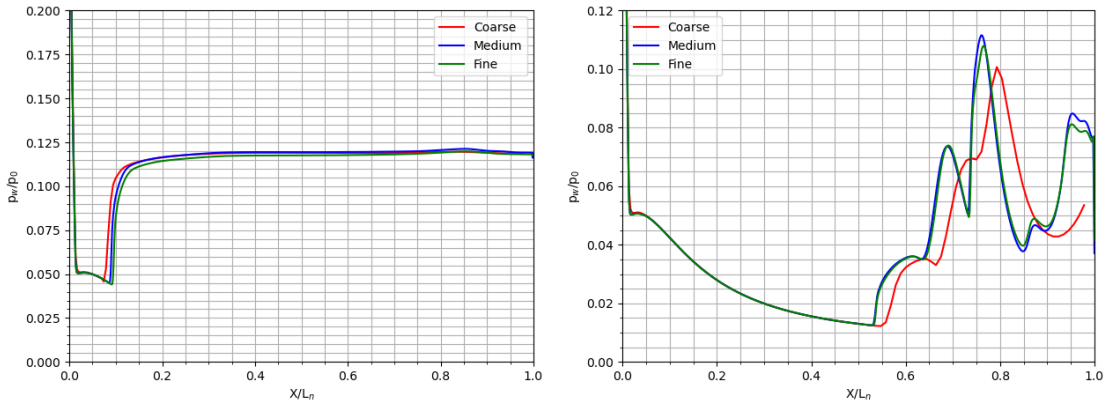
Grid type	First spacing [m]	N_{radial}	N_{axial}	Total number of element	Total number of cells
Coarse	10^{-4}	51	38	30613	30120
Medium	10^{-6}	101	75	112161	111200
Fine	10^{-6}	201	149	181999	180800

Grid Independence Study

Since the flow separation phenomenon has two main patterns, FSS and RSS, the grid independence study was conducted in two versions to test convergence under both flow behavior scenarios. According to Östlund's research, the VOLVO S1 nozzle operates in FSS mode over a nozzle inlet pressure range of up to 1.5 MPa. Accordingly, the PR was chosen as 8 and 16.2.

The results of calculating three grids in FSS and RSS modes are shown in Fig.5.2. The pressure values are normalized with respect to the total chamber pressure p_w/p_0, and the coordinate position is normalized by the length of the divergent nozzle section, x/L_n.

Figure 5.2 demonstrates the convergence of the solution for different pressure ratios. As the number of mesh elements gradually increases, the wall pressure curve approaches a single result. From the FSS results (Fig.5.2a), the pressure curves are almost identical, which makes it difficult to determine convergence. However, the results in Fig.5.2b clearly show the difference between the coarse mesh and finer meshes. The results for the medium and fine meshes are close, which indicates that the solution is converging to a single form. The results for the fine mesh are satisfactory, and this mesh will be used for further calculations. No additional mesh



(a) FSS, $p_0/p_a = 8$ (b) RSS, $p_0/p_a = 16.2$

Figure 5.2: Wall pressure distribution for different mesh resolutions.

refinement is necessary.

5.1.2 CFD Validation

Validation is intended to determine the accuracy of simulated physical phenomena with respect to reality. The concept of validation is based on the quantitative evaluation of a computational model against high-precision experimental instruments. Furthermore, validation incorporates the concept of uncertainty, as experimental data also contain both systematic and random errors.

A common validation strategy consists of several subsections: unit problems, benchmark cases, subsystem cases, and complete cases. The strategy aims to consistently integrate validation cases step by step, from a simpler case to a full system.

The concept of unit problems involves validation using simple geometry, simplified flow, and clearly defined boundary conditions. The preliminary CFD model described in Chapter 3 serves as a partial implementation of this strategy. The model features a simplified conical nozzle geometry with a more accurate definition of turbulent flow and operational gas. Although the preliminary model is not supported by a specific experiment, a correlation was found with analytical calculations, which in turn were derived from theory based on high-precision experiments.

Validating a complete system requires a combination of real equipment or a system that requires validated computational fluid dynamics tools [40].

5.2 Experimental Benchmark for Validation

The verification of the CFD model has been accomplished through a grid convergence study, while validation requires reference to experimental data. This data must be accompanied by detailed and specific conditions under which the prototype was tested. In this project,

Östlund's experimental data will be employed for the CFD validation model, due to his extensive research [37] on flow separation and lateral loads.

Östlund's work presents several nozzles, named as VOLVO S nozzles. These nozzles are scaled-down models of the actual Vulcain rocket engine nozzle. The VOLVO nozzles were tested under laboratory conditions at the Aeronautical Research Institute of Sweden. The tests were conducted at varying nozzle pressure ratios. The VOLVO S1 nozzle geometry was chosen for the validation model, with PRs of 14 and 16, since these pressure ratios correspond to the primary flow separation patterns: FSS and RSS, respectively.

Allamaprabhu [42] provided CFD simulations and analyzed different turbulence models for several nozzles with similar parameters to the VOLVO S1. Wang [43] recreated the identical geometry of VOLVO S1 and simulated it with various CFD turbulence models at different PRs. Schomberg [44] performed a comparative study of the S3 nozzle performance against a proposed nozzle design using a new arc-based design method. All of the aforementioned studies demonstrated PRs of 14 and 16 achieved under steady-state flow, using various turbulence models with good agreement to experimental data. Based on this analysis, the minimum dataset required to create a CFD validation model for this project was identified and is described in detail below.

5.2.1 VOLVO S1 CFD Simulation

After analyzing references [37]-[44], the simulation flow conditions were established. The computational mesh was transferred to ANSYS Fluent Academic Version 2021, where the following parameters were configured:

Physical Models

A steady-state, two-dimensional flow problem with the absolute velocity formulation and a density-based solver. The energy equation and the SST k-omega viscosity models were enabled.

The energy equation should be included because the physical model assumes the simulation of hot exhaust gas exiting the nozzle into a lower-temperature environment. Additionally, as the flow passes through the shock wave, it experiences significant physical changes, including temperature. Accordingly, it is necessary to account for the temperature effects on the material properties of the flow. These changes are described by the energy equation 2.13. In ANSYS Fluent, the energy per unit mass equation is calculated using Eq.5.3, which includes the internal energy, the work done on the gas, and the kinetic energy associated with the flow velocity.

$$E = h - \frac{p}{\rho} + \frac{v^2}{2} \tag{5.3}$$

In addition to the energy equation, a turbulence model must be specified. The literature review revealed that the k-ω SST model is the most stable and suitable for the considered design

problem. The SST model is based on the standard k-ω model, which is an empirical formulation derived from the transport equations for turbulence kinetic energy (k) and specific dissipation rate (ω).

These two variables describe the turbulent flow motion, where k represents the energy of the turbulent eddies, describing the swirling, chaotic motions of turbulent flow. The parameter ω represents the rate at which these eddies decay. The SST model extends the standard k-ω model with two main modifications [45]:

1. The standard model is applied near the walls; a high-Reynolds-number k-ϵ model is used to calculate the flow outside the boundary layer.
2. A modified turbulent viscosity formulation accounts for the transport effects of the principal turbulent shear stress.

The SST k-ω turbulence model is a hybrid formulation that combines the k-ω and k-ϵ models. The k-ω model is well suited for resolving the flow in the viscous layer, which is characteristic of near-wall regions where viscous forces dominate. The k-ϵ model, on the other hand, is better suited for predicting the behavior of the free stream, which is typical of regions farther away from walls.

Material Model

The working gas was designated as air with standard values for specific heat, thermal conductivity, and molecular weight treated as constants. The ideal gas model used to simulate the density properties to account for the compressibility effects of the material, as described by Eq.2.19. In Fluent, the density equation is implemented as:

$$\rho = \frac{p_{op} + p}{\frac{R}{M_w}T} \tag{5.4}$$

Where p_{op} represents the operating pressure and p is the local calculated pressure.

The material viscosity was determined using Sutherland's law:

$$\mu = \mu_0 \frac{T_0 + C}{T + C} \left(\frac{T}{T_0}\right)^{3/2} \tag{5.5}$$

Where μ is dynamic viscosity at temperature T, μ_0 is the reference viscosity at the temperature T_0, and C is Sutherland's constant for the gaseous material.

Boundary Conditions

The computational domain, shown in Fig.4.2, contains three boundaries: the ambient inlet, the nozzle inlet, and the ambient outlet. The ambient boundaries were defined under

standard atmospheric conditions and are assigned as pressure-inlet and pressure-outlet. The nozzle inlet was defined as a pressure-inlet boundary, where the total pressure depends on the PR for a specific case. The assigned boundary values are presented in Table 5.2.

Table 5.2: Boundary conditions for the VOLVO S1 CFD simulation.

Boundary	**Type**	**Value**	**Units**
Ambient inlet	pressure-inlet	101,325	Pa
Ambient outlet	pressure-outlet	101,325	Pa
Nozzle inlet	pressure-inlet	$p_0 = \text{PR} \cdot p_a$	Pa

Four PR values were simulated: 8, 14.2, 16.2, and 22, which correspond to total pressure values of approximately 8, 1.4, 1.6, and 2.2 MPa, respectively. The nozzle contour was defined as a solid, adiabatic, stationary wall. The operating pressure was defined as 0 Pa, since atmospheric pressure is described at the ambient boundaries.

Numerical Methods and Solver Controls

The most stable and accurate simulation was obtained using the combination of methods and solution types for the physical problem presented in Table 5.3. The table summarizes the key parameters defined in the simulation. The results that most closely matched the experimental data were achieved using the Flux Type Roe-FDS solver formulation and second-order computation for both flow and turbulence characteristics.

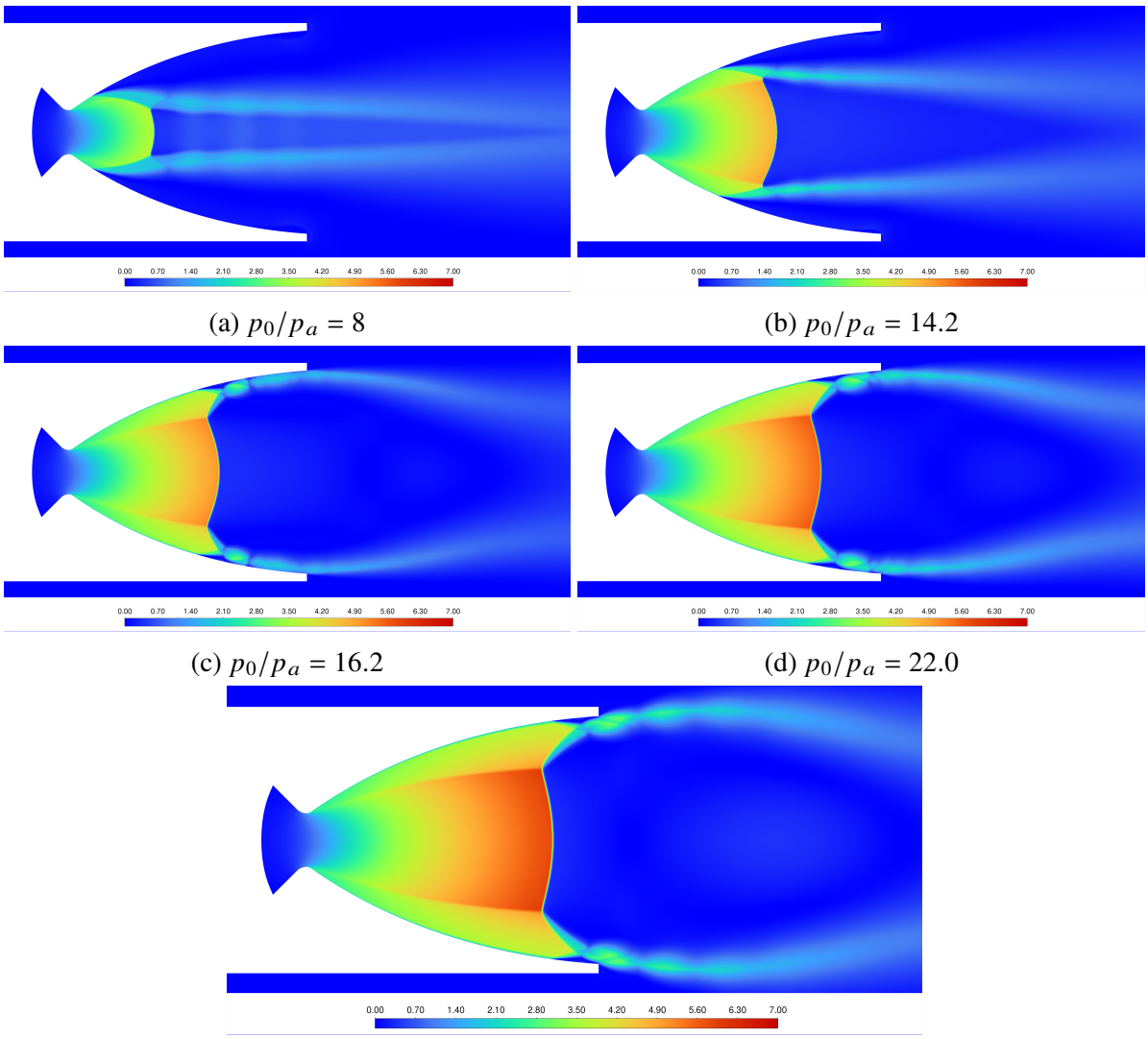
Table 5.3: Summary of Fluent setup: methods and controls.

Methods		**Controls**	
Solution methods	*Type/Value*	*Solution controls*	*Type/Value*
Formulation	Implicit	Courant number (CFL)	1
Flux Type	Roe-FDS	Turbulent kinetic energy	0.8
Gradient	Least Squares Cell Based	Specific dissipation rate	0.8
Flow	Second Order Upwind	Turbulent viscosity	1
Turbulent Kinetic Energy	Second Order Upwind	Solid	1
Specific Dissipation Rate	Second Order Upwind		

Results and Discussion

The ANSYS Fluent simulation results were compared with the experimental data reported by Östlund [37]. A good agreement was achieved at lower pressures, while the findings at higher pressures showed slight discrepancies. This indicates that the simulated physical process is close to the real one, although further optimization of the CFD model is still necessary. The contours

in Fig.5.3 illustrate the Mach number distribution inside the VOLVO S1 nozzle with dependency on the feeding pressure applied at the nozzle inlet.



(a) $p_0/p_a = 8$ (b) $p_0/p_a = 14.2$

(c) $p_0/p_a = 16.2$ (d) $p_0/p_a = 22.0$

(e) $p_0/p_a = 26.5$

Figure 5.3: Mach number contours for different PRs.

In Figs.5.3a and 5.3b, flow separates and continues along the nozzle axis, corresponding to the FSS type. In contrast, Figs.5.3c - 5.3e illustrate the second pattern. The separated flow reflects from the core flow toward the nozzle wall, then reflects again, and continues along the wall, forming multiple reflections and closed recirculation pockets. This flow pattern corresponds to RSS behavior.

For each case, the resulting pressure on the nozzle wall was collected, normalized, and presented in Figs.5.4-5.7.

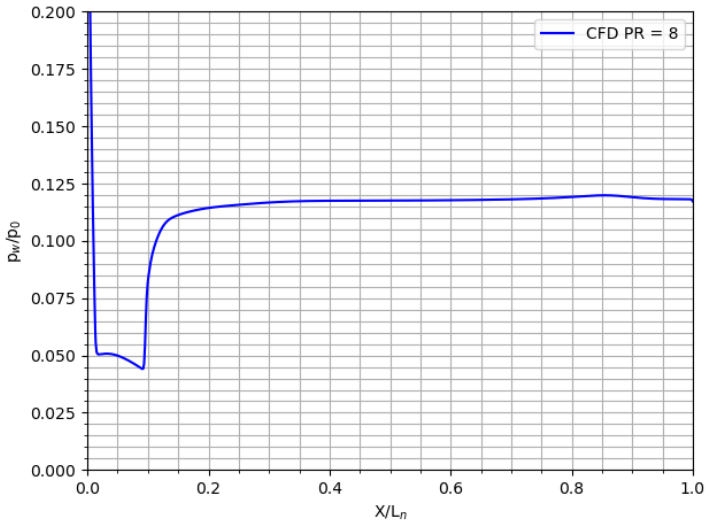


Figure 5.4: Wall pressure distribution at PR = 8.

Figure5.4 presents the wall pressure along the nozzle wall under the FSS regime. Experimental data are not provided for this case.

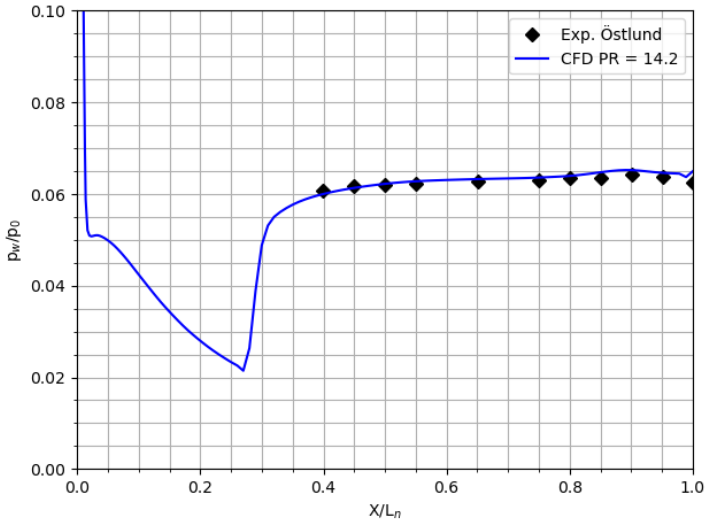


Figure 5.5: Wall pressure distribution at PR = 14.2 compared with experiment.

Figure 5.5 shows the wall pressure along the nozzle wall under the FSS regime at PR = 14.2. The results demonstrate good agreement, with a maximum discrepancy of 3.7% observed at the nozzle exit.

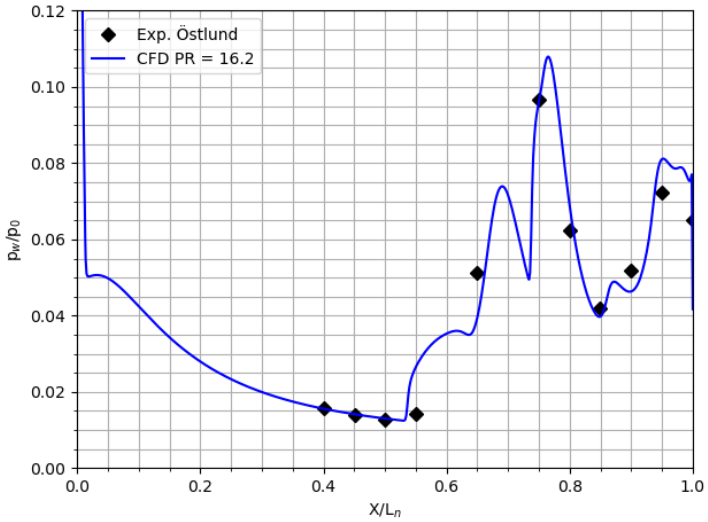


Figure 5.6: Wall pressure distribution at PR = 16.2 compared with experiment.

As shown in Fig.5.6, the wall pressure along the nozzle wall under the RSS regime at PR = 16.2 closely matches the experimental measurements. The CFD model effectively captures the pressure dynamics and accurately reproduces the complex physical process of shock wave interaction. However, the model overestimates the flow separation point ($X/L \approx 0.54$) by approximately 3.6%. This overprediction leads to a downstream shift of the pressure curve, causing noticeable discrepancies with experimental data at several points. Considering the earlier publication by Östlund [46] that includes more detailed data for the VOLVO S1 nozzle, such deviations are not unusual due to the limitations of the experimental equipment.

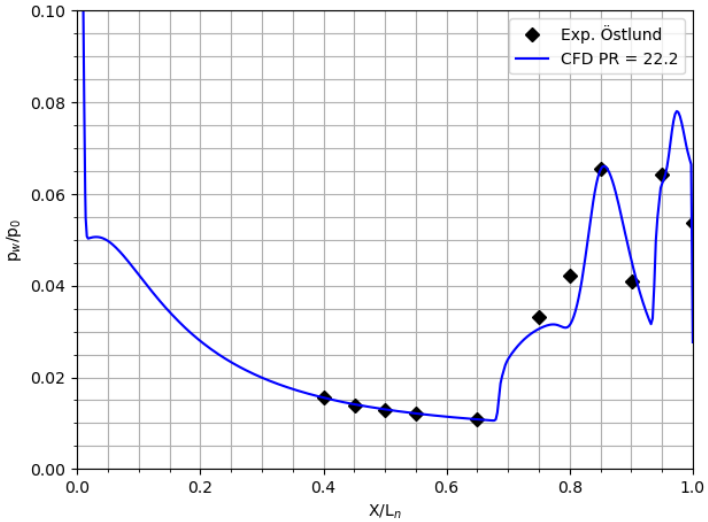


Figure 5.7: Wall pressure distribution at PR = 22.0 compared with experiment.

Figure 5.7 illustrates the wall pressure along the nozzle wall under the RSS regime at PR = 22.0. Likewise, the graph indicates a discrepancy in the determination of the flow separation location. This time, the flow separates later compared to the experimental data. The observed difference is about 4.5%, though it could be smaller due to the absence of intermediate data. Consequently, the pressure curve is shifted to the right. However, the dynamics of pressure along the nozzle wall remain captured.

In conclusion, the results of CFD model demonstrate meaningful and good alignment with the experimental data, despite minor discrepancies observed when simulating more complex flow structures. The model is validated and can be utilized for further analysis.

Chapter 6 - Nozzle Performance Evaluation and Design Modification

In this chapter, methodologies are proposed for evaluating the performance and modifying the nozzle, followed by a comparative study of improvements based on the developed and validated CFD model. The performance assessment focuses on specific impulse and thrust coefficient as the main characteristics of nozzle efficiency, which makes it possible to determine the effectiveness of the working gas at the nozzle exit under various operating conditions. The nozzle modification is based on studies by Frey [12] and Stark [47], who introduced a new contouring concept called TICTOP. This design combines two common nozzle contours, TIC and TOP, aimed to mitigate the internal shock and eliminate RSS, which causes excessive side loads. The TICTOP configuration enables the retention of the advantages inherent in both nozzle types without significant losses in performance and efficiency.

After developing the improved nozzle model, a CFD simulation was conducted utilizing the same ambient parameters and boundary conditions. Thus, the only variable affecting the flow behavior is the parabolic shape of the modified contour. The new results are also subjected to an evaluation process to determine the thrust and thrust coefficient for subsequent comparative analysis of the two nozzle designs.

6.1 Performance Evaluation Methodology

The primary parameters used for the comparative assessment of efficiency are the specific impulse, Eq.1.7, and the thrust coefficient, Eq.1.8. These parameters are directly influenced by the exhaust velocity, mass flow rate, exit and chamber pressures, the thermal and molecular properties of the gas, and the geometric characteristics of the nozzle. When the geometry is fixed, the primary factors become the flow parameters at the nozzle exit. Specifically, exit velocity, exit pressure, and mass flow rate. These variables are essential components of the rocket thrust equation (Eq.1.8). However, the thrust equation is applicable only to an idealized one-dimensional case in which the flow at the nozzle exit is steady, uniform, and lossless. In practice, achieving such a flow condition is nearly impossible.

The VOLVO S1 simulation results clearly demonstrate the nonlinear distribution of the main flow parameters at the nozzle exit section. Figure 6.1 shows the distribution of the exit flow Mach number M_e along the nozzle axis versus the exit section radius r_e. The figure indicates that the highest flow velocity shifts from the nozzle center (the red and orange lines

corresponding to the FSS regime) toward the nozzle walls (the green and blue lines during the RSS mode) as pressure increases. Additionally, the flow periodically acquires a negative axial velocity, crossing the black dashed line $M_e = 0$, which indicates that the flow locally moves into the nozzle rather than exiting it.

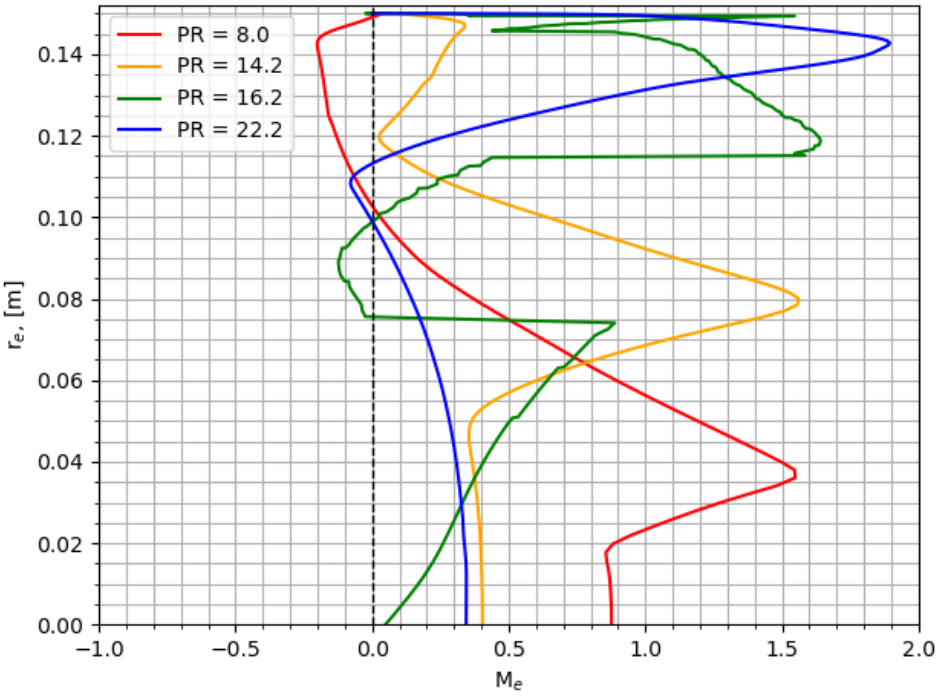
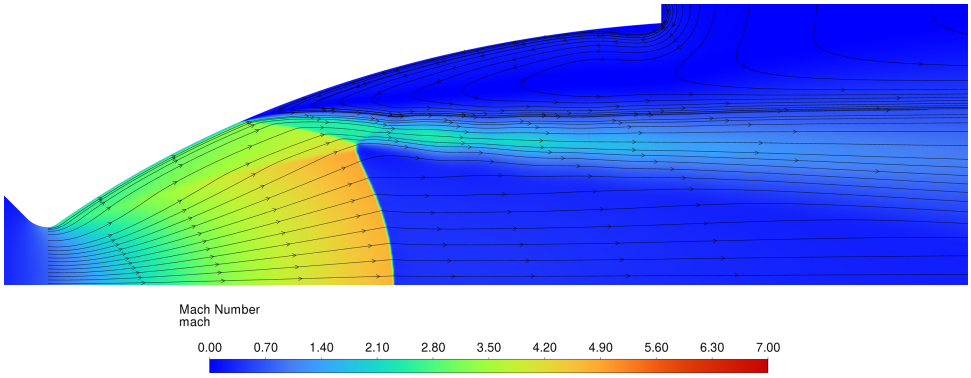
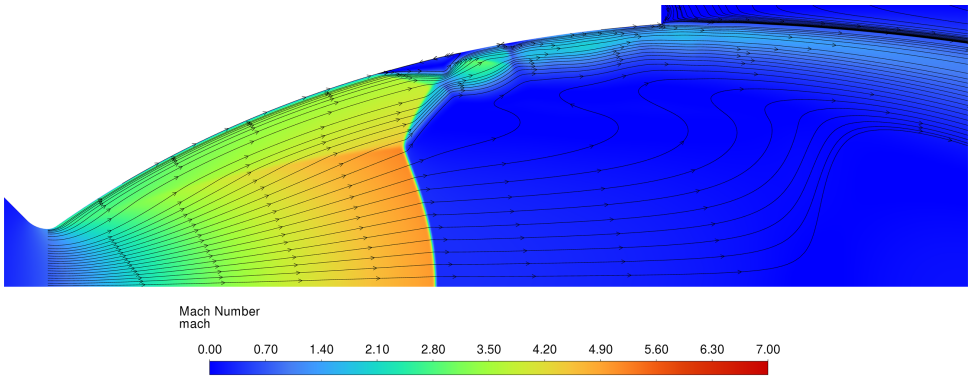


Figure 6.1: Axial Mach number distribution at various PR along the exit cross-section.

This behavior is caused by the formation of recirculation zones under different operating conditions, which is clearly illustrated in the streamline contours in Fig.6.2. The arrows and lines indicate flow motion within the nozzle, showing the formation of a large recirculation zone at a pressure ratio of 14.2, where the flow goes along the upper nozzle wall, collides with the exhaust jet, and exits parallel to the axis line.



(a) Mach number streamlines $p_0/p_a = 14.2$



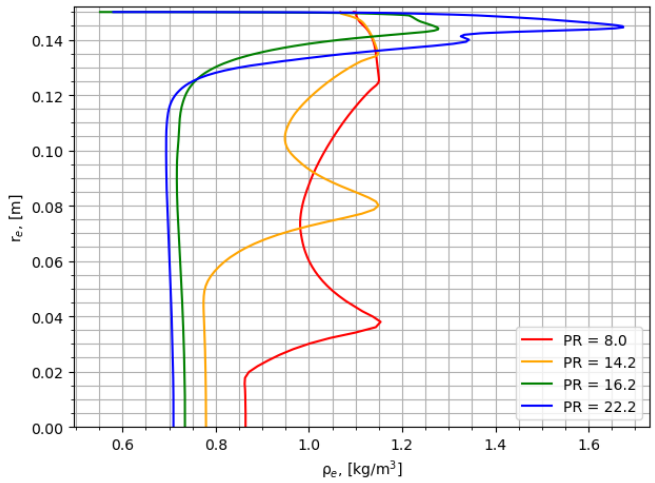
(b) Mach number streamlines $p_0/p_a = 16.2$

Figure 6.2: Mach number streamlines for different PRs.

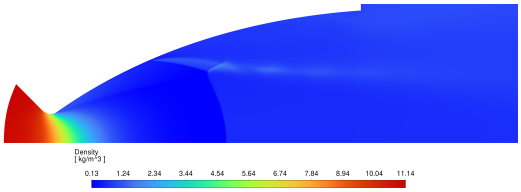
In contrast, under the RSS regime (Fig.6.2b), the recirculation zone is formed within the core of the nozzle, causing the gas to swirl in the middle of the exit cross section.

In addition to changes in velocity, the simulation results provide insights into other key parameters at the exit section necessary for evaluating nozzle performance.

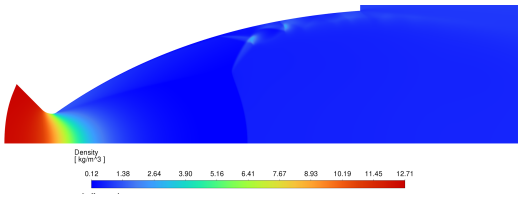
Figure 6.3 presents the density distribution ρ_e, shown both as a function of the nozzle exit radius and in contour forms. Similarly to velocity, density directly characterizes the mass flow rate (Eq.2.4), which impacts the engine's thrust coefficient and specific impulse.



(a) Density distribution at the exit cross-section



(b) Density contour at $p_0/p_a = 14.2$

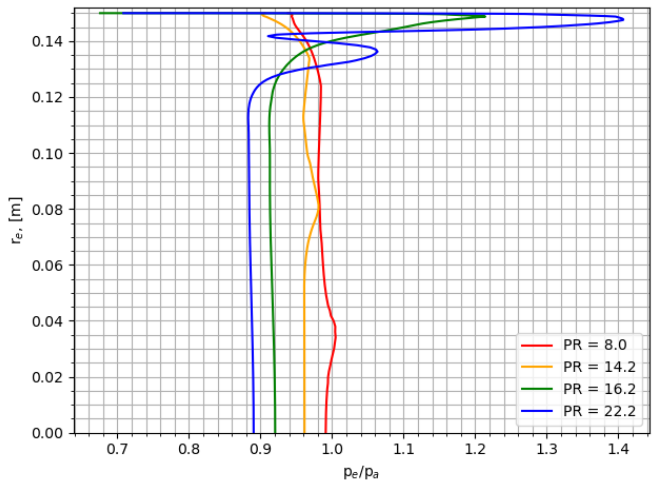


(c) Density contour at $p_0/p_a = 16.2$

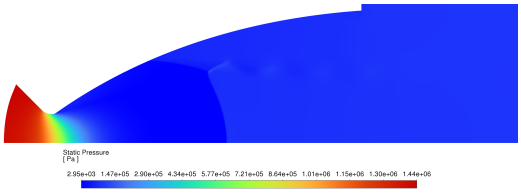
Figure 6.3: Density distribution at nozzle exit (left) and density contours (right) for different PRs.

According to Fig.6.3, the denser flow shifts from the center toward the nozzle walls as the pressure ratio increases. This dynamic is caused by the displacement of the exhaust jet and the formation of compression shock waves, where the gas is more compressed due to higher velocity and higher pressure.

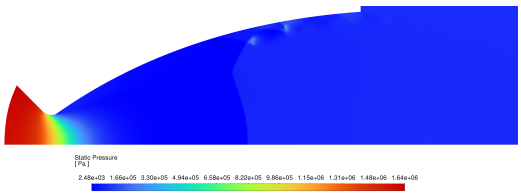
The final key parameter for evaluating nozzle efficiency is the exit pressure p_e, shown in Fig.6.4. The exit pressure also plays a crucial role in determining the engine's thrust.



(a) Pressure distribution at the exit cross-section



(b) Pressure contour at $p_0/p_a = 14.2$



(c) Pressure contour at $p_0/p_a = 16.2$

Figure 6.4: Pressure distribution at nozzle exit (left) and Pressure contours (right) for different PRs.

Figure 6.4a illustrates the exit pressure normalized by the ambient pressure along the radius of the exit plane. Similar to the previous parameters, increased pressure is observed at the locations of the exhaust jets, where the flow is subjected to higher pressure due to the presence of shock waves.

In summary, the distribution of key flow parameters across the nozzle exit section clearly demonstrates the limitation of using idealized equations for computing thrust coefficient and specific impulse. Therefore, the performance parameters will be evaluated using integral equations of impulse flux and pressure force at the exit of the nozzle.

Considering that the simulation is two-dimensional and axisymmetric, Fluent treats the axis of symmetry as the line of revolution, rotating the 2D cross-section by 360° to represent a three-dimensional domain. Consequently, when assessing the mass flow through the exit line, the software computes the flow through an annular surface. The mass flow through this surface is obtained by summing the contributions from each facet area, as defined by Eq.6.1.

$$\dot{m} = \sum_{i=1}^{n} \rho_i \vec{v}_i \cdot \vec{A}_i \tag{6.1}$$

Due to the non-uniform flow velocity, which may also be misaligned with the nozzle axis, the concept of effective exhaust velocity, $V_{e,\text{eff}}$, is introduced to estimate thrust. Calculating this velocity takes into account various factors, such as friction, non-axial flow direction, and the pressure differential. In other words, it represents the average velocity of the exhaust mass in the axial direction. The effective axial velocity is obtained using a mass-weighted average of the axial velocity, as expressed in Eq.6.2.

$$V_{e,\text{eff}} = \frac{\sum_{i=1}^{n} u_{i,ax} \rho_i \left(\vec{v}_i \cdot \vec{A}_i\right)}{\sum_{i=1}^{n} \rho_i \left(\vec{v}_i \cdot \vec{A}_i\right)} \tag{6.2}$$

The final unknown component of the thrust equation is the static pressure at the nozzle exit. This parameter will be determined using an area-weighted average, which calculates the average pressure across the surface of the exit section and is defined by Eq.6.3.

$$\bar{p}_e = \frac{1}{A_e} \sum_{i=1}^{n} p_{i,e} \left|A_{i,e}\right| \tag{6.3}$$

With the relevant data collected from the simulation and computing the parameters using Eqs.1.6-1.8, Table 6.1 of the performance characteristics of the VOLVO S1 nozzle can be constructed.

Table 6.1: VOLVO S1 performance parameters.

PR, flow regime	$\dot{m}$ [kg/s]	$V_{e,\text{eff}}$ [m/s]	Thrust [N]	C_F	I_{sp} [s]
8.0, FSS	5.39	260.75	1259.15	0.44	23.83
14.2, FSS	9.45	310.12	2653.22	0.52	28.62
16.2, RSS	10.78	384.08	3750.49	0.65	35.48
22.0, RSS	14.64	466.67	6450.72	0.82	44.94

A table of changes in the parameters of the modified nozzle, varying with operating pressure, is compiled and presented similarly.

6.2 Design Modification and TICTOP Concept

The main idea behind the development of the TICTOP nozzle type is a modification of the TOP nozzle contour, specifically the first half of its diverging section. The motivation for this modification is to prevent the occurrence of RSS, since this phenomenon – especially during the transition from FSS to RSS – results in the highest side loads. The RSS is most common in TOP-type nozzles. In contrast, TIC type nozzles do not exhibit this behavior, maintaining flow separation in the FSS mode.

This observation was validated by Hagemann [15], who conducted at the P6.2 facility of the German Aerospace Center a comparative experimental study, where nozzles of both types were tested for flow separation behavior during engine start-up and shutdown. The investigation demonstrated the absence of RSS in the TIC nozzle and confirmed that the transitions between FSS and RSS modes are the primary source of extreme side loads in overexpanded nozzles.

Accordingly, Frey and Stark ([12] and [47]) proposed a novel method for contouring a rocket nozzle, which combines the advantages of both traditional contour types. The TICTOP concept integrates two design approaches: the upper part of the nozzle near the throat follows the ideal truncated contour, while the remaining part is a thrust-optimized contour. The geometric transition between the profiles must preserve continuity, slope, and smoothness. The resulting contour retains the advantages of the higher pressure of TOP-type nozzles while also maintaining the favorable flow separation behavior typical of TIC-type contours.

6.2.1 Geometry of TIC and TICTOP Nozzles

Following the published methodology, a new nozzle geometry was developed and implemented. The geometric parameters R_t, R_e, and θ_e from the original VOLVO S1 nozzle were preserved. A family of similar nozzles was subsequently created using the Method of Characteristics. Only two parameters are varied: the Mach design number (M_{des}) and the axial position of the transition between the two profiles (I_{TIC}). This approach allows the generation of multiple TIC contours, the upper sections of which can be integrated into the original TOP nozzle.

To construct an ideal contour, it is necessary to specify the design Mach number and

determine the range of values for this parameter. The Mach design number is associated with the minimum of the range, $M_{des,\,min}$, for such a contour that intersects the upper point of the exit cross-section of the original TOP contour. Larger values of M_{des} then produce additional alternative contours.

Figure 6.5 illustrates several ideal MOC-generated contours overlaid on the original TOP contour. The contour that intersects the TOP exit point corresponds to a Mach design number of 3.25. The maximum value of M_{des} is considered to be at 4.0, since an ideal contour with a higher design Mach number does not intersect the TOP contour and therefore cannot be integrated into the original geometry without altering the fixed geometric parameters.

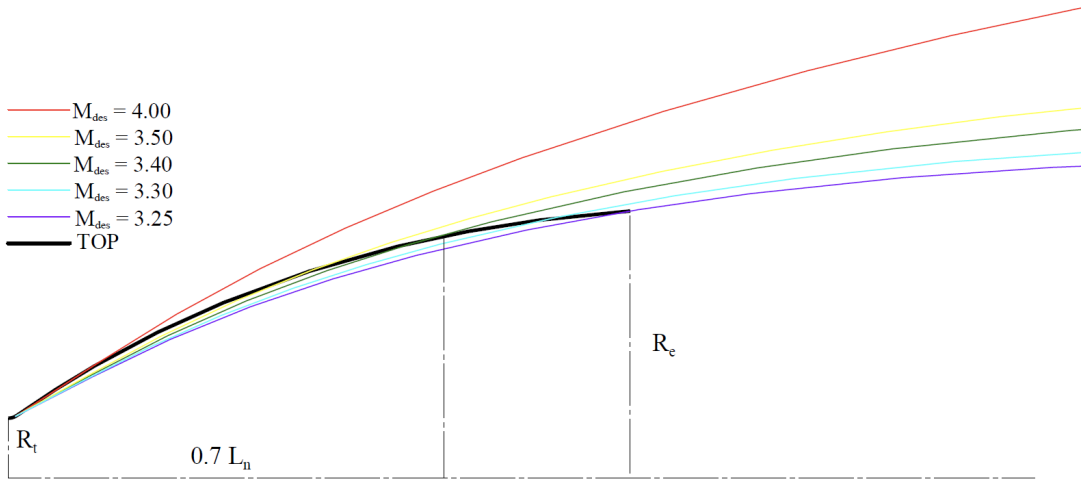


Figure 6.5: Comparison of TIC contours with the baseline TOP nozzle geometry.

The second variable is the axial position of the transition between the profiles. This position is determined by the location of the first right-hand characteristic that is not in contact with the internal shock. However, such an assessment requires a CFD simulation of the nozzle, which is a substantial and time-consuming task.

The experimental study [47] evaluated the TICTOP nozzle concept in comparison with a traditional TOP nozzle. The paper discusses two constructed versions: TICTOP-B1 and TICTOP-C2. One of the differences between these nozzles is the length of the integrated ideal contour: a larger portion of TICTOP-B1 features the TIC contour, whereas TICTOP-C2 includes only a small segment of the ideal contour. After numerous start-up and shutdown cycles, it was found that TICTOP-B1 consistently suppressed RSS, while the TICTOP-C2 occasionally exhibited RSS, demonstrating a high sensitivity to internal shock waves.

Based on these findings, the axial position of I_{TIC} was established at 70% of the nozzle length to avoid accidental formation of RSS. The ideal contour was selected for integration with a Mach design number of 3.4 to provide the new contour with a greater convexity. The TIC contour was truncated at the point $I_{TIC} = 0.7\ L_n$ and connected to the original TOP contour. The transition point between the two lines was smoothed using a fillet tool to eliminate the sharp corner. In parallel, a TIC-type nozzle was created for additional assessment of flow separation and validation of the absence of the RSS mode in case the TICTOP nozzle undergoes a mode change.

The ideal contour with a corresponding Mach design number of 3.4 was selected for

integration. The TIC profile was truncated and joined to the original TOP contour at at the 0.7 L_n location. The transition point between the two profiles was smoothed using a fillet tool to eliminate the sharp corner. In parallel, a TIC-type nozzle with M_{des} = 3.25 was constructed as an additional assessment of flow separation and to validate the absence of the RSS regime. The three contours, TOP, TIC, and TICTOP, are shown in Fig.6.6.

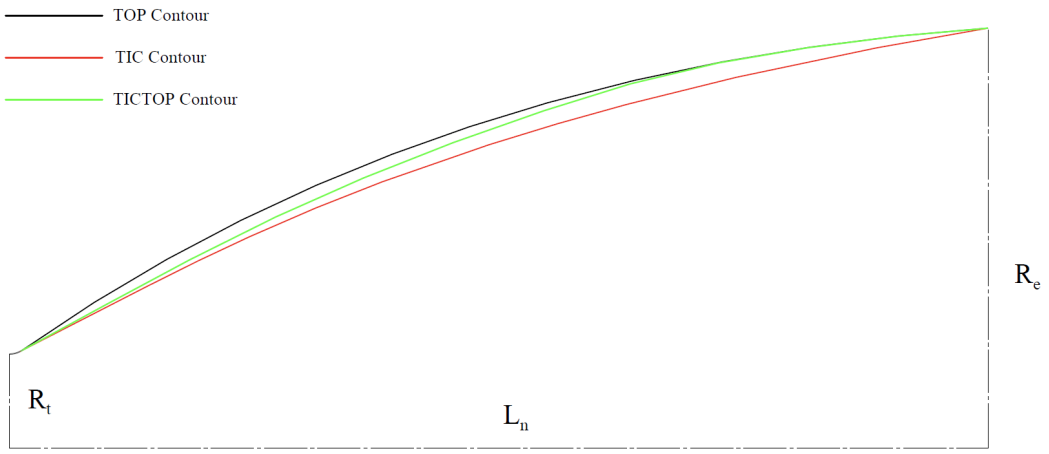
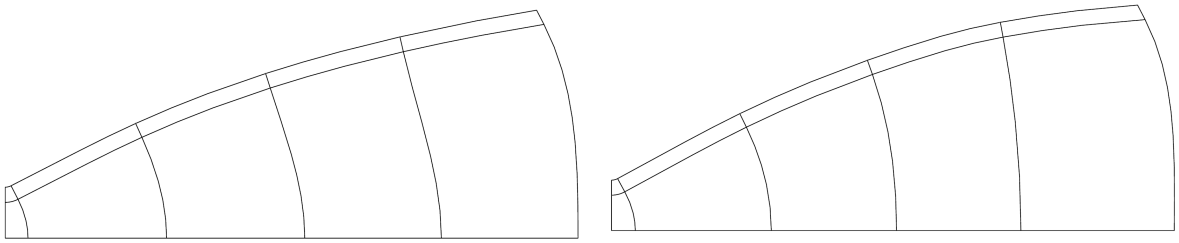


Figure 6.6: Comparison of TIC, TOP, and TICTOP contours.

6.2.2 Mesh Generation for TIC and TICTOP Nozzles

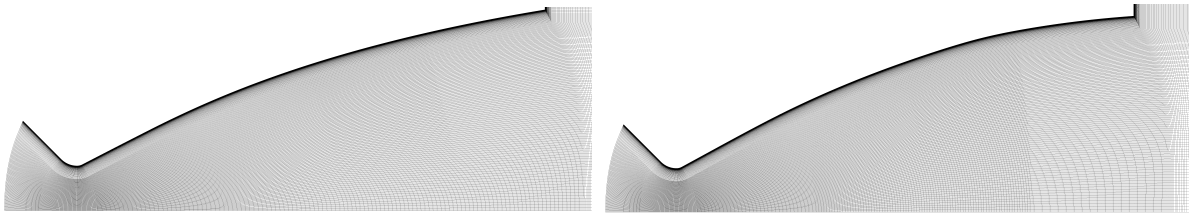
Following the creation of the alternative nozzle contours, the geometry of the fluid domain was divided into blocks, similar to the method outlined in Chapter 4, presented in Fig.6.7. Subsequently, the structured blocks for both nozzles were utilized for the mesh generation.



(a) Block structure of TIC S1 nozzle (b) Block structure of TICTOP S1 nozzle

Figure 6.7: Block-structured sections of TIC and TICTOP nozzles.

The meshes were generated in a manner similar to the VOLVO S1 nozzle fine mesh. Figure 6.8 illustrates the meshes for the TIC and TICTOP nozzle sections. For each mesh, the y^+ parameter is kept close to 1, which corresponds to a first layer mesh height of 10^{-6}m.



(a) Mesh of TIC S1 nozzle (b) Mesh of TICTOP S1 nozzle

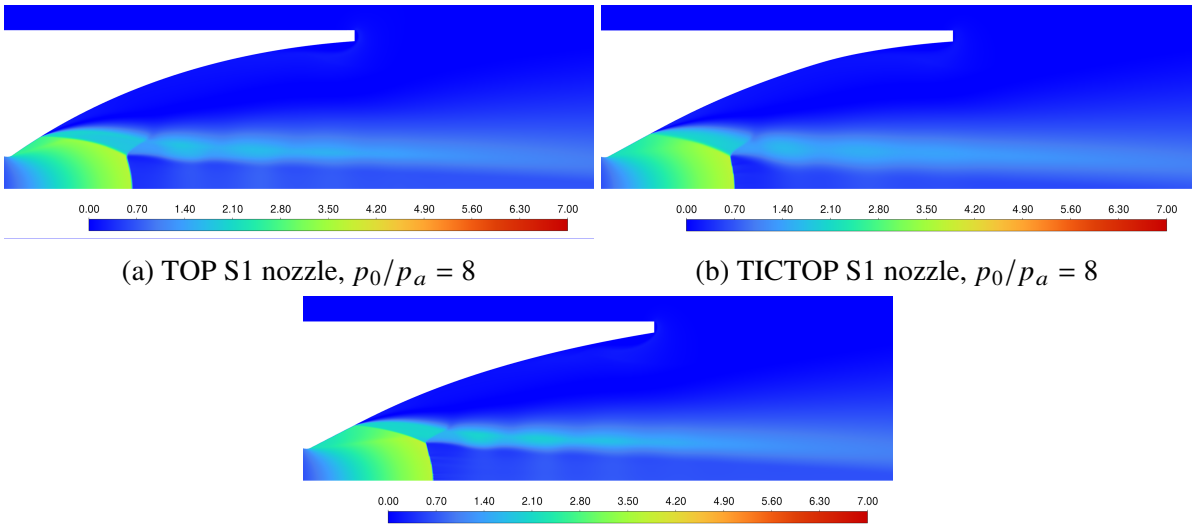
Figure 6.8: Nozzle section meshes of the TIC and TICTOP types.

6.3 Results and Discussion

Two alternative nozzle designs were built and simulated in Ansys Fluent using the same boundary conditions, fluid material properties, and numerical methods as those applied to the original S1 nozzle. The main goal of the modification is to delay the flow separation within the nozzle and to prevent a transition to the less favorable RSS regime. At the same time, the nozzle's performance should not be significantly affected. Four representative PR values were selected to evaluate the effectiveness of the modification.

6.3.1 Pressure Ratio 8.0 Results

Figure 6.9 displays the Mach number contours for the three nozzles at a pressure ratio of 8. Flow separation occurs in the FSS regime in all cases.



(a) TOP S1 nozzle, $p_0/p_a = 8$ (b) TICTOP S1 nozzle, $p_0/p_a = 8$

(c) TIC S1 nozzle, $p_0/p_a = 8$

Figure 6.9: Mach number contours for TOP, TICTOP, and TIC nozzles at PR = 8.

Figure 6.10 illustrates the wall-pressure variation for the three nozzle types at PR = 8. The TIC and TICTOP nozzles show a noticeable downstream shift in the onset of flow separation, with the TICTOP nozzle displaying a smoother pressure jump.

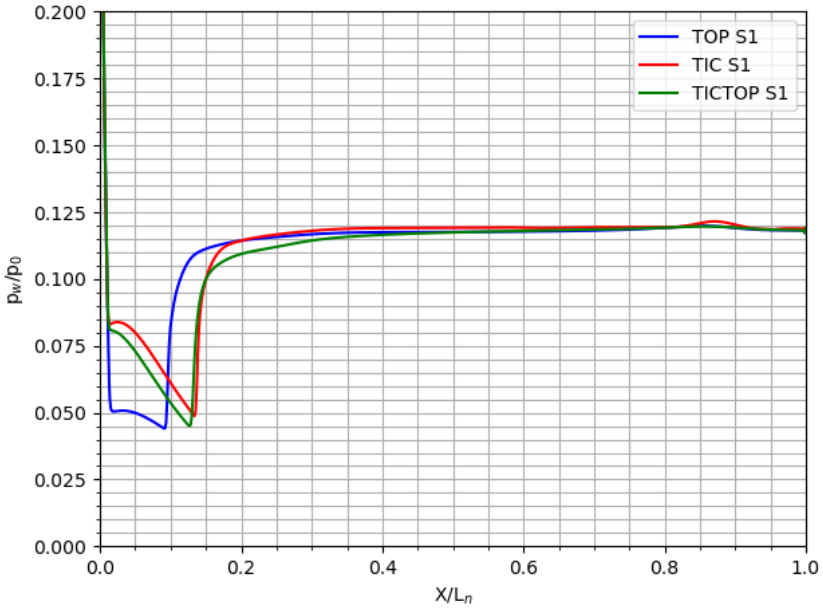
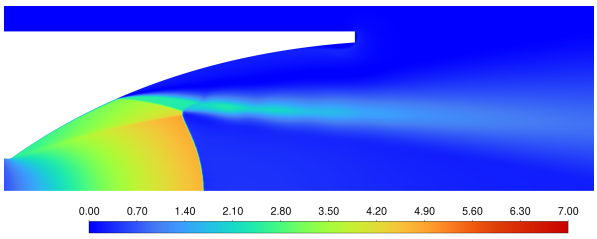


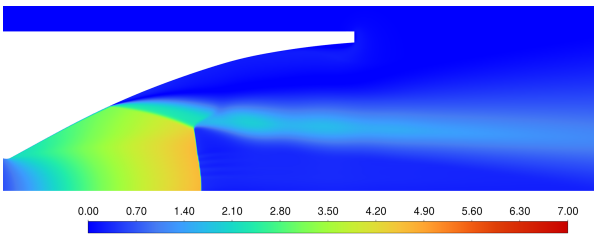
Figure 6.10: Wall-pressure distributions for TOP, TICTOP, and TIC nozzles at PR = 8.

6.3.2 Pressure Ratio 14.2 Results

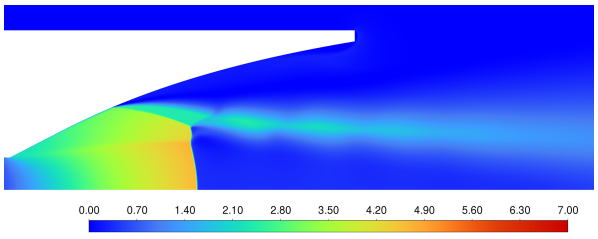
Figure 6.11 shows the Mach number contours for the three nozzles at a pressure ratio of 14.2. In all cases, flow separation occurs in the FSS regime.



(a) TOP S1 nozzle, $p_0/p_a = 14.2$



(b) TICTOP S1 nozzle, $p_0/p_a = 14.2$



(c) TIC S1 nozzle, $p_0/p_a = 14.2$

Figure 6.11: Mach number contours for TOP, TICTOP, and TIC nozzles at PR = 14.2.

Additionally, the contours in Fig.6.11 reveal the formation of an internal shock (indicated by a darker shade of orange within the jet core), which is partly responsible for the displacement

of the shock waves toward the wall. In the TOP nozzle, the internal shock is curved and directed toward the wall; in the TIC nozzle, the internal shock is straight and aligned with the nozzle axis. The only nozzle that behaves differently is the TICTOP design, in which the internal shock is not visible – an indication of the modification's effectiveness at this pressure ratio.

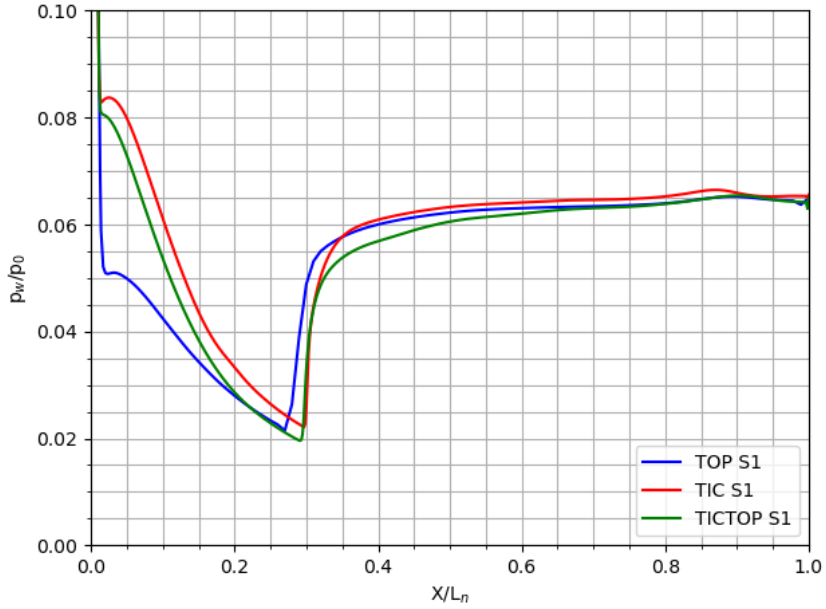
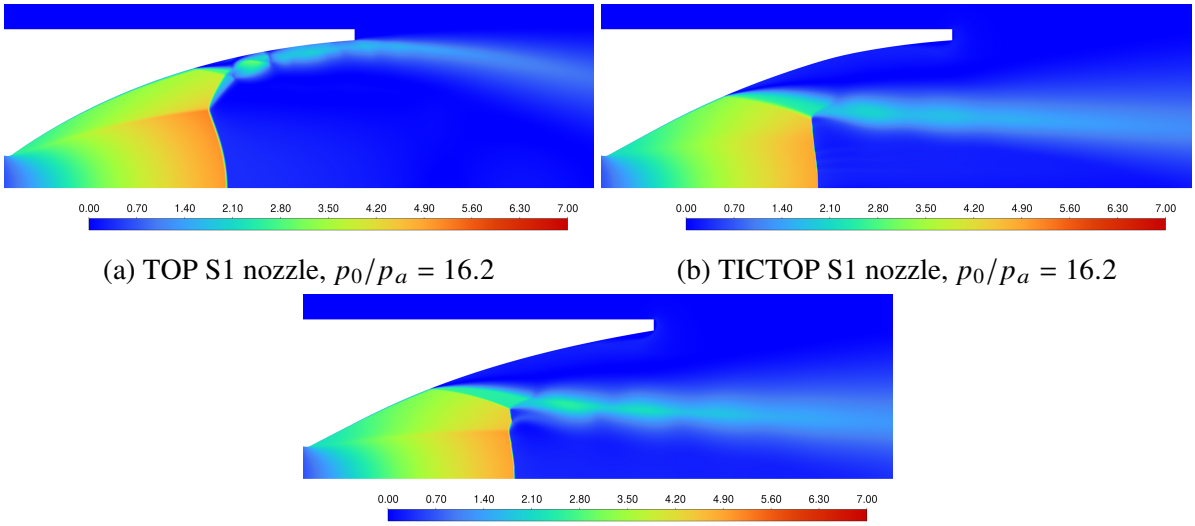


Figure 6.12: Wall-pressure distributions for TOP, TICTOP, and TIC nozzles at PR = 14.2.

Figure 6.12 shows the wall-pressure variation for the three nozzle types at PR = 14.2. Similarly, the TIC and TICTOP nozzles shift the flow separation point downstream. The TICTOP nozzle also exhibits a smoother pressure jump, distributing the load over a larger surface.

6.3.3 Pressure Ratio 16.2 Results

Figure 6.13 presents the Mach number contours for the three nozzles at PR = 16.2. The TOP nozzle is the only one where the RSS regime develops. In the other two nozzles, the flow remains in the FSS regime, exhibiting a normal shock wave in the jet core. It is also notable that the internal Mach number distribution in the TICTOP nozzle is smooth and uniform, with no clearly identifiable internal shock.



(a) TOP S1 nozzle, p_0/p_a = 16.2

(b) TICTOP S1 nozzle, p_0/p_a = 16.2

(c) TIC S1 nozzle, p_0/p_a = 16.2

Figure 6.13: Mach number contours for TOP, TICTOP, and TIC nozzles at PR = 16.2.

The wall-pressure distribution for the three nozzles at a pressure ratio of 16.2 is shown in Fig.6.14. In the TOP nozzle, flow separation occurs farther downstream due to the transition to the RSS separation mode. This delay in separation is undesirable because the main goal is to prevent the flow from entering the more adverse RSS regime. The TIC and TICTOP nozzles successfully maintain FSS behavior, fulfilling this requirement.

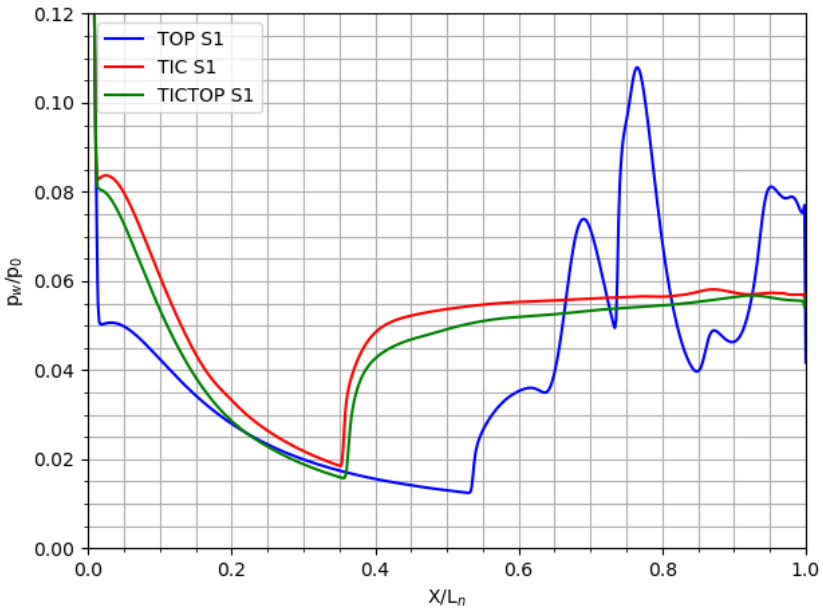
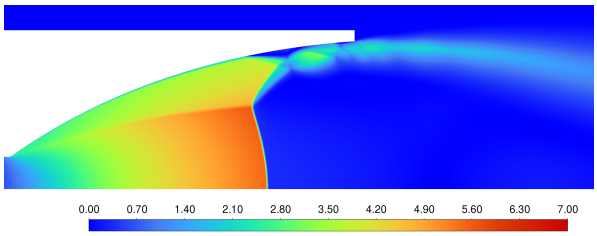


Figure 6.14: Wall-pressure distributions for TOP, TICTOP, and TIC nozzles at PR = 16.2.

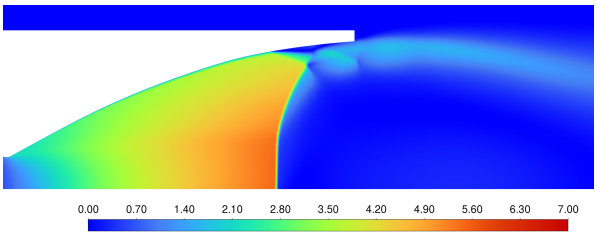
6.3.4 Pressure Ratio 22.0 Results

Figure 6.15 illustrates the Mach number contours for three nozzles at a pressure ratio of PR = 22.0. At this pressure level, the RSS regime also appears in the TICTOP nozzle. This

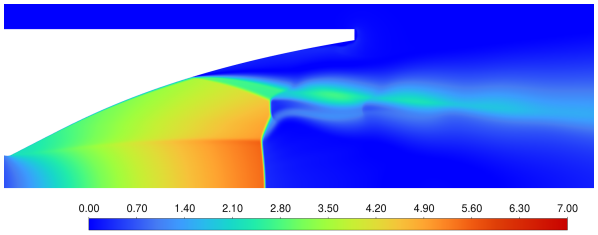
indicates that the modified design can no longer maintain the more favorable separation mode. Several factors may contribute to this, such as an abrupt geometric change between the TIC and TOP profiles or insufficient integration length of the TIC contour into the original design. Conversely, the TIC nozzle continues to maintain FSS-type separation, consistent with findings reported in the literature.



(a) TOP S1 nozzle, $p_0/p_a = 22.0$



(b) TICTOP S1 nozzle, $p_0/p_a = 22.0$



(c) TIC S1 nozzle, $p_0/p_a = 22.0$

Figure 6.15: Mach number contours for TOP, TICTOP, and TIC nozzles at PR = 22.0.

Despite the occurrence of the RSS separation, the TICTOP nozzle still partially meets the requirement of delaying flow separation downstream, as shown in Fig.6.16. The separation point in the TICTOP nozzle shifts to the right by nearly 10% compared to the separation point in the TOP nozzle. Furthermore, due to this downstream shift, the peak load seen in the TOP nozzle does not occur in the modified design.

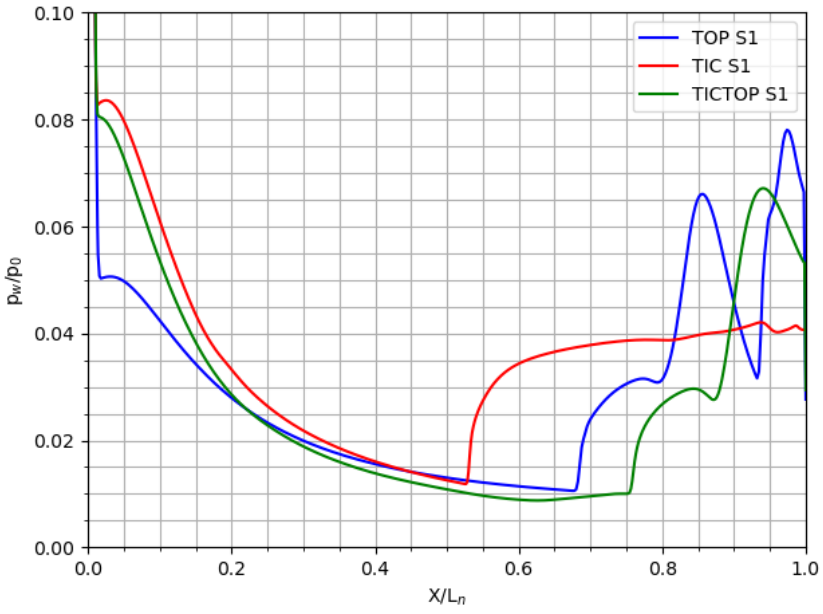


Figure 6.16: Wall-pressure distributions for TOP, TICTOP, and TIC nozzles at PR = 22.0.

6.3.5 Final Performance Comparison

To conclude the assessment of the implemented modifications, a performance comparison of the simulated nozzles needs to be conducted. For each design, the performance parameters were evaluated using the same methodology described earlier. The resulting Table 6.2 summarizes the key nozzle characteristics for each PR scenario.

Table 6.2: Comparison of key performance metrics of TOP, TICTOP, and TIC nozzles.

PR	**Nozzle type**	$\dot{m}$ [kg/s]	$V_{e,\text{eff}}$ [m/s]	$\bar{p}_e$ [kPa]	Thrust [N]	C_F	I_{sp} [s]
8.0	TOP S1	5.39	260.75	99.26	1259.15	0.44	23.83
	TICTOP S1	5.29	264.61	98.73	1290.06	0.45	24.83
	TIC S1	5.33	266.71	99.58	1300.05	0.45	24.84
14.2	TOP S1	9.45	310.12	97.39	2653.22	0.52	28.62
	TICTOP S1	9.39	329.52	98.08	2867.68	0.56	31.11
	TIC S1	9.46	339.17	100.07	3121.06	0.61	33.63
16.2	TOP S1	10.78	384.08	95.81	3750.49	0.65	35.48
	TICTOP S1	10.71	359.23	95.88	3465.58	0.59	32.97
	TIC S1	10.76	385.25	95.75	3754.98	0.64	35.55
22.0	TOP S1	14.64	466.67	95.95	6450.72	0.82	44.94
	TICTOP S1	14.51	439.18	87.79	5418.55	0.68	38.06
	TIC S1	14.62	456.38	91.83	6002.36	0.76	41.86

Analysis of Table 6.2 highlights the main advantages and disadvantages of each nozzle design concerning performance during the gradual increase in chamber pressure under sea-level conditions. Focusing only on the traditional TIC and TOP contours, it is clear that at low pressures during the engine start-up, the TIC nozzle provides a higher thrust than the TOP nozzle. However, this phase is very short, as the combustion chamber pressure rapidly rises within fractions of a second to much higher levels, at which point the thrust-optimized design surpasses TIC in performance. At sufficiently high chamber pressures, the TOP nozzle becomes more advantageous at low altitudes because of its greater expansion capability and proves significantly more beneficial at high altitudes where ambient pressure drops.

The modified TICTOP nozzle offers only limited performance improvements, which are insufficient to justify replacing traditional TIC and TOP nozzle designs. During the start-up phase, the TICTOP nozzle displays improved characteristics similar to those of an ideal-contour nozzle. However, once higher pressures are reached, it loses this advantage.

Nevertheless, the TICTOP nozzle demonstrated the ability to maintain flow separation in the more favorable regime, a significant advantage that suggests its design methodology deserves further consideration. Since TIC-type nozzles are widely used in modern aerospace applications, the TICTOP concept has the potential to offer an optimized balance of safety and performance for future rocket engine nozzles.

6.4 Conclusion

The objectives of this project were to create and validate a computational model capable of predicting flow separation in overexpanded nozzles, as well as to design a new bell-shaped nozzle that delays and reduces separation. The results demonstrated that simulating flow separation in supersonic flows requires careful attention to each stage of CFD model development. Despite the complexity of the task, the project presents an accessible engineering approach that allows for the numerical reconstruction of a highly complex physical phenomenon with realistic accuracy.

The preliminary investigation of a conical nozzle was a crucial first step in understanding the problem. Its simple shape makes it easier to analyze both theoretically and practically. The equations that define its geometric parameters are intuitive, and constructing the initial CFD model takes relatively little time and effort. This makes the conical nozzle an ideal candidate for preparing for more advanced CFD challenges. The results from this preliminary model offer a strong foundation for understanding flow behavior and the conditions that lead to separation – such as the Summerfield criterion that separation begins when wall pressure reaches about 40% of the ambient pressure.

Building on this foundation, a detailed CFD model of the VOLVO S1 nozzle – with its thrust-optimized parabolic TOP contour – was developed. One of the key achievements of the project is the creation of a structured-mesh generation strategy using block decomposition of the geometry. This method is easy to apply and significantly reduces the computational effort needed to build high-quality meshes in CFD environments. The technique is broadly applicable and capable of producing meshes of professional quality, which is crucial for verifying and validating CFD models.

A key part of the project involves validating the experimental data of Östlund's research. The CFD model successfully reproduced the transition from FSS to RSS, the separation location was accurately captured, and both the magnitude and overall shape of the wall-pressure distribution were matched. The findings demonstrate that the RANS simulation and the *k-omega* SST turbulence model are reliable and appropriate for predicting flow separation in overexpanded nozzles.

The final stage of the project focused on developing an optimized hybrid contour, TICTOP, which combines features of the two traditional nozzle designs. This effort was made possible by the initial MOC study that helped to create ideal contours. The methodology also allowed for the rapid construction of an additional TIC nozzle model, which supported a more thorough comparative analysis. While completely eliminating RSS was not achieved, the TICTOP nozzle demonstrated the ability to delay the onset of RSS and create a smoother internal supersonic flow structure. These results suggest that this design concept has promising potential.

The project also has limitations that point toward future research directions. A steady, two-dimensional model cannot fully capture the nature of flow separation, which is highly sensitive to asymmetries and small disturbances. A more complete understanding would require expanding the model to three dimensions and incorporating unsteady simulations. This approach would enable the characterization of asymmetric separation patterns and more complex internal shock structures. Additionally, the current model should be scaled to match real rocket-nozzle dimensions and include reacting flows, since combustion and scale effects play significant roles in determining separation behavior.

In conclusion, this project resulted in robust CFD models that enhance the understanding of separation phenomena in high-expansion-ratio nozzles. The developed practical methodologies provide a foundation for future nozzle design efforts aimed at achieving both high performance and structural reliability.

References

[1] Mishra, D. P., *Fundamentals of Rocket Propulsion*, CRC Press, Boca Raton, FL, 1st ed., 2017.

[2] Leishman, J. G., *Introduction to Aerospace Flight Vehicles*, Embry-Riddle Aeronautical University, Daytona Beach, FL, 2023.

[3] Hadjadj, A. and Onofri, M., "Nozzle Flow Separation," *Shock Waves*, Vol. 19, June 2009, pp. 163–169.

[4] Smalley, K., Brown, A., Ruf, J., and Gilbert, J., "Flow Separation Side Loads Excitation of Rocket Nozzle FEM," *48th AIAA/ASME/ASCE/AHS/ASC Structures, Structural Dynamics, and Materials Conference*, Honolulu, HI, Apr. 23–26 2007.

[5] Khobragade, N., Wylie, J., Gustavsson, J., and Kumar, R., "Control of Flow Separation in a Rocket Nozzle Using Microjets," *New Space*, Vol. 7, No. 1, April 2019, pp. 31–42.

[6] Marrion, M., Costigan, G., and Bellhouse, B., "Flow Separation Control in Over-Expanded Supersonic Nozzles," *35th AIAA Fluid Dynamics Conference and Exhibit*, Toronto, ON, Canada, June 6–9 2005.

[7] Hagemann, G., Immich, H., Van Nguyen, T., and Dumnov, G. E., "Advanced Rocket Nozzles," *Journal of Propulsion and Power*, Vol. 14, No. 5, 1998, pp. 620–634.

[8] Huzel, D. K. and Huang, D. H., *Modern Engineering for Design of Liquid-Propellant Rocket Engines*, American Institute of Aeronautics and Astronautics, Washington, DC, 1992.

[9] Morrisette, E. L. and Goldberg, T. J., "Turbulent-Flow Separation Criteria for Overexpanded Supersonic Nozzles," NASA Technical Report NASA-TP-1207, NASA Langley Research Center, Hampton, VA, Aug. 1978.

[10] Khare, S. and Saha, U. K., "Rocket Nozzles: 75 Years of Research and Development," *Sādhanā*, Vol. 46, No. 76, 2021.

[11] Sutton, G. P. and Biblarz, O., *Rocket Propulsion Elements*, Wiley, Hoboken, NJ, 9th ed., 2017.

[12] Frey, M., Makowka, K., and Aichner, T., "The TICTOP Nozzle: A New Nozzle Contouring Concept," *CEAS Space Journal*, Vol. 9, 2016, pp. 175–181.

[13] Nave, L. H. and Coffey, G. A., "Sea Level Side Loads in High-Area-Ratio Rocket Engines," *9th AIAA Propulsion Conference*, American Institute of Aeronautics and Astronautics, Las Vegas, NV, Nov. 5–7 1973.

[14] Nasuti, F. and Onofri, M., "Shock Structure in Separated Nozzle Flows," *Shock Waves*, Vol. 19, July 2009, pp. 229–237.

[15] Hagemann, G., Frey, M., and Koschel, W., "Appearance of Restricted Shock Separation in Rocket Nozzles," *Journal of Propulsion and Power*, Vol. 18, No. 3, 2002, pp. 577–584.

[16] Zaheer, S. Q., Disimile, P. J., and Toy, N., "Controlling the Jet of Overexpanded Nozzle Using Coanda Effect," *AIAA Scitech 2023 Forum*, National Harbor, MD, Jan. 23–27 2023.

[17] Verma, S. B. and Haidn, O., "Unsteady Side-Load Evolution in a Liquid Rocket Engine Nozzle," *Journal of Spacecraft and Rockets*, Vol. 57, No. 2, 2020, pp. 391–397.

[18] Stark, R. H., "Flow Separation in Rocket Nozzles: An Overview," *49th AIAA/ASME/SAE/ASEE Joint Propulsion Conference*, San Jose, CA, July 14–17 2013.

[19] Ansys, "What is Computational Fluid Dynamics (CFD)?" https://www.ansys.com/simulation-topics/what-is-computational-fluid-dynamics, Retrieved February 14, 2025.

[20] Zmijanovic, V., Lago, V., Sellam, M., et al., "Thrust Shock Vector Control of an Axisymmetric Conical Supersonic Nozzle via Secondary Transverse Gas Injection," *Shock Waves*, Vol. 24, 2014, pp. 97–111.

[21] Stark, R. and Jack, S., "Restricted Shock Separation in Out-of-Round TOP Nozzles," *Proceedings of the 34th International Symposium on Shock Waves (ISSW34)*, Daegu, Korea, July 16–21 2023.

[22] Muhammed, I., N., S. B., Suryan, A., Lijo, V., Simurda, D., and Kim, H. D., "Computational study of flow separation in truncated ideal contour nozzles under high-altitude conditions," *International Journal of Fluid Engineering*, Vol. 1, No. 1, March 2024.

[23] Alfonsi, G., "Reynolds-Averaged Navier–Stokes Equations for Turbulence Modeling," *Applied Mechanics Reviews*, Vol. 62, July 2009.

[24] Scarlatella, G., Tajmar, M., and Bach, C., "Advanced Nozzle Concepts in Retro-Propulsion Applications for Reusable Launch Vehicle Recovery: A Case Study," *Proceedings of the 72nd International Astronautical Congress (IAC-21)*, Dubai, United Arab Emirates, Oct. 25–29 2021.

[25] Alvi, F., "Active Control of Supersonic Impinging Jets Using Supersonic Microjets," *Journal of Propulsion and Power*, Vol. 21, No. 1, Jan. 2005, pp. 71–79.

[26] Schneider, D., Stark, R., Génin, C., Oschwald, M., and Kostyrkin, K., "Active Control of Dual-Bell Nozzle Operation Mode Transition by Film Cooling and Mixture Ratio Variation," *Journal of Propulsion and Power*, Vol. 36, No. 5, Oct. 2019, pp. 1–12.

[27] Salim, S. M. and Cheah, S. C., "Wall y+ Strategy for Dealing with Wall-Bounded Turbulent Flows," *Lecture Notes in Engineering and Computer Science*, Vol. 2175, Jan. 2009.

[28] Zucrow, M. J. and Hoffman, J. D., *Gas Dynamics, Volume 1*, John Wiley & Sons, 1976.

[29] Zucrow, M. J. and Hoffman, J. D., *Gas Dynamics, Volume 2*, John Wiley & Sons, 1977.

[30] Anderson, J. D., *Modern Compressible Flow: With Historical Perspective*, Aeronautical and Aerospace Engineering Series, McGraw-Hill Education, 2003.

[31] Anderson, J. D., *Fundamentals of Aerodynamics*, McGraw-Hill Education, 6th ed., 2017.

[32] Ansys, "Method of Characteristics – Lesson 6," https://innovationspace.ansys.com/courses/wp-content/uploads/2020/12/Lesson6-Handout-NT-v1.pdf, Retrieved March 18, 2025.

[33] Niemeyer, K., "Gas Dynamics Notes," https://kyleniemeyer.github.io/gas-dynamics-notes/intro.html, Retrieved March 20, 2025.

[34] Maurya, S., "Minimum Length Nozzle Design Using Method of Characteristics," https://www.mathworks.com/matlabcentral/fileexchange/57098-minimum-length-nozzle-design-using-method-of-characteristics, Retrieved March 20, 2025.

[35] Summerfield, M., Forster, C., and Swan, W., "Flow Separation in Overexpanded Supersonic Exhaust Nozzles," *Jet Propulsion*, Vol. 24, Sept. 1954, pp. 319–320.

[36] Verma, S. B., "Experimental investigations on confined coaxial supersonic jets," *Shock Waves*, Vol. 18, No. 5, 2008, pp. 345–355.

[37] Östlund, J., "Flow Processes in Rocket Engine Nozzles with Focus on Flow Separation and Side-Loads," TRITA-MEK 2002:09, KTH Royal Institute of Technology, 2002.

[38] Rao, G. V. R., "Exhaust Nozzle Contour for Optimum Thrust," *Journal of Jet Propulsion*, Vol. 28, No. 6, 1958, pp. 377–382.

[39] Thompson, J. F., Soni, B. K., and Weatherill, N. P., *Handbook of Grid Generation*, CRC Press, Boca Raton, FL, 1999.

[40] AIAA, *Guide for the Verification and Validation of Computational Fluid Dynamics Simulations*, Jan. 1998, AIAA G-077-1998 (R2002).

[41] NASA Glenn Research Center, "Spatial Convergence Tutorial," https://www.grc.nasa.gov/www/wind/valid/tutorial/spatconv.html, n.d., Retrieved September 15, 2025.

[42] Allamaprabhu, Y., Raghunandan, B. N., and Moríñigo, J. A., "Numerical prediction of nozzle flow separation: Issue of turbulence modeling," *Aerospace Science and Technology*, Vol. 50, 2016, pp. 31–43.

[43] Wang, L., Tian, Z., Yu, H., Zhang, Y., and Li, H., "Comparative study on the performance of turbulence models in flow separation of large expansion ratio nozzle," *Journal of Physics: Conference Series*, Vol. 2364, No. 1, 2022, pp. 012035.

[44] Schomberg, K., Olsen, J., and Doig, G., "Design of High-Area-Ratio Nozzle Contours Using Circular Arcs," *Journal of Propulsion and Power*, Vol. 32, No. 1, 2016, pp. 188–195.

[45] ANSYS Inc., "ANSYS Fluent Theory Guide," https://www.afs.enea.it/project/neptunius/docs/fluent/html/th/node67.htm, 2013, Retrieved October 30, 2025.

[46] Mattsson, J., Högmann, U., and Torngren, L., "A Sub Scale Test Programme on Investigation of Flow Separation & Side Loads in Rocket Nozzles," *Aerothermodynamics for space vehicles*, edited by R. A. Harris, Vol. 426 of *ESA Special Publication*, Jan. 1999, p. 373.

[47] Stark, R. and Génin, C., "Experimental Study of TICTOP Nozzles," *31st International Symposium on Shock Waves (ISSW31)*, Nagoya, Japan, 2017, pp. 515–522.

Appendix A - MOC Calculation

```
%% Appendix A
% Method of characteristics for steady, 2D, irrotational, supersonic flow
clear all; clc;

% Initial parameters:
% Specific heat ratio
gamma = 1.4;
% Design Mach number
M_des = 2.5;
% Desired number of characteristic lines
n = 20;

% Input validation
validateInputs(gamma, M_des, n);

% Half of maximum flow deflection angle
theta_max = 0.5 * PrandtlMeyer(M_des, gamma) * 180 / pi;
% Compute angular increment between characteristics
dtheta = theta_max / n;
% Total number of nodes in the characteristic network (series formula for
% a triangular mesh)
nodes = 0.5 * n * (n + 3)

% Initialize zero arrays for storing
M = zeros(1, nodes);        % Mach number
mu = zeros(1, nodes);       % Mach angle
theta = zeros(1, nodes);    % Flow deflection angle
v = zeros(1, nodes);        % Prandtl-Meyer angle
K_Left = zeros(1, nodes);   % Left-running characteristic constant
K_Right = zeros(1, nodes);  % Right-running characteristic constant

%% MOC parameter calculation

% Initial characteristic values:
% Initial increment of deflection angle for n lines
theta(1:n) = dtheta + (0:n-1) * dtheta;
% Initial Prandtl-Meyer angle
v(1:n) = theta(1:n);
% Initial characteristic line constants from compatibility equations
K_Left(1:n) = theta(1:n) - v(1:n);      % Should be zero
K_Right(1:n) = theta(1:n) + v(1:n);     % Should be 2*theta

% Initial conditions for the centerline symmetry
theta(n+1) = theta(n);
v(n+1) = v(n);
K_Left(n+1) = K_Left(n);
```

```
K_Right(n+1) = K_Right(n);

% Initialize track coefficients
LineN = 2;  % To track the current characteristic line number
nID = n+2;  % To track the index of a node

% Compute characteristic line intersection and boundary nodes
for k = 1:n-1   % Number of remaining lines
    j = LineN;
    h = nID;
    % Compute the current node angles and constants
    theta(h) = 0;
    K_Right(h) = K_Right(j);
    v(h) = K_Right(j) - theta(h);
    K_Left(h) = theta(h) - v(h);
    % Next characteristic line
    j = j + 1;
    % Compute the internal nodes
    for i = h+1:n-LineN+nID % Next point on the current line
        K_Right(i) = K_Right(j);
        K_Left(i) = K_Left(i-1);
        % Calculate angles for the internal node
        theta(i) = 0.5 * (K_Left(i) + K_Right(i));
        v(i) = 0.5 * (K_Right(i) - K_Left(i));
        j = j + 1;
    end
    % Check the boundary condition
    if i == n-LineN+nID
        h = i + 1;
    else
        h = h + 1;
    end
    % Set the last values for the boundary
    theta(h) = theta(h-1);
    v(h) = v(h-1);
    K_Left(h) = K_Left(h-1);
    K_Right(h) = K_Right(h-1);
    %Next line and node index update
    LineN = LineN+1;
    nID = h+1;
end

% Compute Mach number and Mach angle for each node
for i=1:nodes
    % Return Mach number from Prandtl-Meyer function
    M(i)=flowprandtlmeyer(gamma,v(i),'nu');
    mu(i)=Mu(M(i));
end

% Plot characteristic mesh
figure(1)
D = 1;    % D=1 for non-dimensional calculation
i = 1;
% Initialize node coordinates
x = zeros(1, nodes);
y = zeros(1, nodes);
% Maximum flow turning angle
wall = theta_max;
```

```
105 while (i <= n+1)
106     % First characteristic
107     if i == 1
108         x(i) = -D / (tand(theta(i) - mu(i)));
109         y(i) = 0;
110         plot([0 x(i)],[D 0]);
111         hold on
112     % Last characteristic
113     else if i == n+1
114             x(i) = (y(i-1) - D - x(i-1) * tand((theta(i-1) + theta(i) + mu(
                    i-1) + mu(i)) * 0.5)) / (tand(0.5 * (wall + theta(i))) -
                    tand((theta(i-1) + theta(i) + mu(i-1) + mu(i)) * 0.5));
115             y(i) = D + x(i) * tand(0.5 * (wall + theta(i)));
116             plot([x(i-1) x(i)],[y(i-1) y(i)]);
117             hold on
118             plot([0 x(i)],[D y(i)]);
119             hold on
120         %Internal characteristic
121         else
122             x(i) = (D - y(i-1) + x(i-1) * tand(0.5 * (mu(i-1) + theta(i-1)
                    + mu(i) + theta(i)))) / (tand(0.5 * (mu(i-1) + theta(i-1) +
                    mu(i) + theta(i))) - tand(theta(i) - mu(i)));
123             y(i) = tand(theta(i) - mu(i)) * x(i) + D;
124             plot([x(i-1) x(i)],[y(i-1) y(i)]);
125             hold on
126             plot([0 x(i)],[D y(i)]);
127             hold  on
128         end
129     end
130     i = i+1;
131     hold on
132 end
133 % The remaining lines
134 h = i;
135 k = 0;
136 i = h;
137 for j = 1:n-1
138     while (i <= h+n-k-1)
139         % First node
140         if (i == h)
141             x(i) = x(i-n+k) - y(i-n+k) / (tand(0.5 * (theta(i-n+k) + theta(
                    i) - mu(i-n+k) - mu(i))));
142             y(i) = 0;
143             plot([x(i-n+k) x(i)],[y(i-n+k) y(i)]);
144             hold on
145         % Last node
146         else if (i == h+n-k-1)
147                 x(i) = (x(i-n+k) * tand(0.5 * (theta(i-n+k) + theta(i))) -
                        y(i-n+k) + y(i-1) - x(i-1) * tand((theta(i-1) + theta(i)
                         + mu(i-1) + mu(i)) * 0.5)) / (tand(0.5 * (theta(i-n+k)
                        + theta(i))) - tand((theta(i-1) + theta(i) + mu(i-1) +
                        mu(i)) * 0.5));
148                 y(i) = y(i-n+k) + (x(i) - x(i-n+k)) * tand(0.5 * (theta(i-n
                        +k) + theta(i)));
149                 plot([x(i-1) x(i)],[y(i-1) y(i)]);
150                 hold on
151                 plot([x(i-n+k) x(i)],[y(i-n+k) y(i)]);
152                 hold on
```

```
153             %Internal nodes
154             else
155                 s1 = tand(0.5 * (theta(i) + theta(i-1) + mu(i) + mu(i-1)));
156                 s2 = tand(0.5 *(theta(i)+theta(i-n+k)-mu(i)-mu(i-n+k)));
157                 x(i) = (y(i-n+k) - y(i-1) + s1 * x(i-1) - s2 * x(i-n+k)) /
                        (s1-s2);
158                 y(i) = y(i-1) + (x(i) - x(i-1)) * s1;
159                 plot([x(i-1) x(i)],[y(i-1) y(i)]);
160                 hold on
161                 plot([x(i-n+k) x(i)],[y(i-n+k) y(i)]);
162                 hold on
163             end
164         end
165         i = i+1;
166     end
167     k = k+1;
168     h = i;
169     i = h;
170     hold on
171 end
172 % Plot settings:
173 title(sprintf('%d Characteristic Lines \n Design Mach = %.2f \\gamma = %.2f
        ', n, M_des, gamma))
174 xlabel('x/x0');
175 ylabel('y/y0');
176 axis equal
177 xlim([0 x(nodes) + 0.5])
178 ylim([0 y(nodes) + 0.5])
179 grid on
180
181 % Necessary functions:
182 % Mach angle function
183 function mu = Mu(M)
184 mu = asind(1/M);
185 end
186
187 % Prandtl-Meyer function
188 function v = PrandtlMeyer(M,gamma)
189 v = sqrt((gamma+1)/(gamma-1)) * atan(sqrt((gamma-1)*(M^2-1)/(gamma+1))) -
        atan(sqrt(M^2-1));
190 end
191
192 % Validation function
193 function validateInputs(gamma, Me, n)
194     if gamma <= 1, error('Gamma must be greater than 1');
195     end
196     if Me < 1, error('Exit Mach number must be supersonic (Me >= 1)');
197     end
198     if n < 2, error('Number of characteristics must be greater than 2');
199     end
200 end
```